

PROBING STAR FORMATION AT LOW AND
HIGH REDSHIFT WITH ZEUS, A NEW
SUBMILLIMETER GRATING SPECTROMETER

A Dissertation

Presented to the Faculty of the Graduate School

of Cornell University

in Partial Fulfillment of the Requirements for the Degree of

Doctor of Philosophy

by

Steven Hailey-Dunsheath

May 2009

© 2009 Steven Hailey-Dunsheath

ALL RIGHTS RESERVED

PROBING STAR FORMATION AT LOW AND HIGH REDSHIFT WITH ZEUS,
A NEW SUBMILLIMETER GRATING SPECTROMETER

Steven Hailey-Dunsheath, Ph.D.

Cornell University 2009

We have detected emission in the $J = 6 \rightarrow 5$ transition ($\lambda = 453 \mu\text{m}$) of the carbon monoxide isotopologue ^{13}CO from the starburst nucleus of the nearby galaxy NGC 253. This is the first extragalactic detection of this transition, which traces the warm, dense molecular gas found in regions of massive star formation. An excitation analysis of the CO line strengths measured here and obtained from the literature finds that $\approx 35\% - 60\%$ of the molecular gas mass ($M_{\text{H}_2} \approx 2.9 \times 10^7 M_{\odot}$) in the nuclear region is both warm ($T \sim 110 \text{ K}$) and dense ($n_{\text{H}_2} \sim 10^4 \text{ cm}^{-3}$). We find that the gas is most likely heated either by an elevated density of cosmic rays, or by the dissipation of supersonic turbulence. As both of these heat sources are the result of stellar feedback within the starburst, our analysis suggests that the starburst may be self-limiting.

We also present the detection of emission in the $^2\text{P}_{3/2} \rightarrow ^2\text{P}_{1/2}$ transition ($\lambda = 158 \mu\text{m}$) of ionized carbon from MIPS J142824.0+352619, an extremely luminous star-forming galaxy at $z = 1.325$. We combine this measurement with existing observations of the far-infrared continuum and CO emission to estimate that the bulk of the molecular gas in this galaxy is dense ($n_{\text{H}_2} \sim 10^4 \text{ cm}^{-3}$), and is illuminated by an ambient far-ultraviolet radiation field ~ 1000 times more intense than the mean field measured in our Galaxy. These are similar conditions as experienced by the molecular gas in the starburst nuclei of nearby galaxies, and suggests that this source may be modeled as a scaled-up version

of a starburst nucleus. The large star formation rate and molecular gas reservoir indicate that MIPS J142824.0+352619 is likely the progenitor of one of the population of massive elliptical galaxies seen in the local Universe.

These observations were made with ZEUS, a new direct-detection grating spectrometer operating at the Caltech Submillimeter Observatory. ZEUS is a broad-band spectrometer providing a resolving power of $\lambda/\Delta\lambda \sim 1000$ across the $350 \mu\text{m}$ and $450 \mu\text{m}$ telluric windows. It uses a 1×32 semiconductor bolometer array oriented along the dispersion direction, and is configured to simultaneously provide a 16 pixel spectrum covering $\Delta\nu \sim 10$ GHz in each of the two windows. The current sensitivity is within a factor of ≈ 1.2 and ≈ 1.3 of the background photon limit at the centers of the $350 \mu\text{m}$ and $450 \mu\text{m}$ bands, respectively, and this superb sensitivity coupled with the large instantaneous bandwidth make ZEUS an excellent tool for the observation of extragalactic spectral lines. Here we describe the design, construction, characterization, and implementation of this new instrument.

BIOGRAPHICAL SKETCH

Steven James Hailey-Dunsheath was born to John Dunsheath and Ann Hailey in Davenport, IA on May 7, 1979. Careful analysis of photographic evidence shows that he was an adorably rotund child, whose appearance suggested to some a likeness to a large chunk of cheese. He has one sibling, an older sister named Megan, who thanklessly looked after the well-being of her younger brother throughout his childhood.

After matriculating from Davenport West High School, Steven moved 120 miles west to attend Grinnell College in Grinnell, IA. There, he pursued a liberal arts education by taking classes in numerous subjects, but developed a keen interest in physics. A summer working as a researcher for Professor Robert Cadmus at the school's Grant O. Gale observatory sparked an interest in astronomy. Hours spent writing code and digging through low signal to noise data, and long nights waiting for the clouds to clear, helped prepare him for the realities of scientific research. While at Grinnell, Steven also worked diligently on his billiards game, played the occasional midfield on the school soccer team, and celebrated the minor victories in life with inexpensive beer. It was during his time at Grinnell that Steven was lucky enough to meet and successfully woo his current and future partner in all things, Lara Ratzlaff. Steven graduated with honors in May of 2001 with a Bachelor of Arts in Physics.

In September of 2001, Steven accepted a position as a technician in the Astronomy Department at Cornell University in Ithaca, NY. Working in the lab of Gordon Stacey, Steven began designing and building ZEUS, a project he decided to see to fruition by joining the department as a graduate student in the fall of 2002. The next six years are mostly remembered by Steven as a blurry melange of coffee, coursework, cursing, and cryogenics. But after 7 observing

runs, 5 conferences, 4 apartments, 2 automobiles, and a quick trip to the South Pole, Steven was ready to set off from Ithaca and move on to his next adventure. January 2009 will find him in Munich, Germany, where he will join the Infrared and Submillimeter group at the Max Planck Institute for Extraterrestrial Physics. In his free time he hopes to travel, develop his Maß-curling abilities, and track down the perfect Brötchen.

This dissertation is dedicated to Lara, whose support and encouragement made it possible.

ACKNOWLEDGEMENTS

This work was made possible by the efforts of many individuals, and it is my pleasure to acknowledge their contributions. Firstly I thank my advisor, Gordon Stacey, for entrusting the construction of his newly-funded spectrometer to a youngster with little experience. I have learned a great deal about submillimeter instrumentation and astrophysics from working with Gordon, but perhaps the most important lessons have concerned the fine art of knowing when a project is finished. I will always remember that “the enemy of good is better”, and that if “you can’t see it from a trotting horse, don’t worry about it.” Thomas Nikola has been heavily involved in all aspects of this project, from the early design work to the scientific publication, and without his superhuman efforts the submillimeter group would cease to function. Steve Parshley built the instrument mount and the control unit for the ^3He refrigerator, and has saved the day on many occasions with last-minute machining jobs. Tom Oberst constructed the data acquisition hardware, and despite having little programming experience, wrote the acquisition and reduction software as well. Carl Ferkinhoff built the stepper motor controller as an undergraduate summer student, and as a graduate student was on hand to help guide the instrument through a particularly chaotic, but eventually fruitful, observing run.

I also received a great deal of help from the many knowledgeable people on the 2nd floor of Space Sciences. Terry Herter educated me on the fundamentals of optical design, and Luke Keller undertook the unenviable task of teaching me Zemax. In addition to providing the instrument with a dewar, George Gull helped me with many aspects of the mechanical design and answered my many AutoCAD questions. I learned everything I know about pumping down a dewar from Chuck Henderson, who also taught me how to work with cryogenic

wiring, and how to find the humor present in any situation.

I also owe thanks to Harvey Moseley, Christine Allen, Dominic Benford, and Johannes Staguhn at NASA Goddard Space Flight Center for providing us with an excellent detector array, and to Johannes for helping us troubleshoot some electrical issues at the telescope. The essential filters were fabricated by Peter Ade and Carole Tucker at Cardiff University. I also thank the CSO staff, and in particular the day crew: Ed, Steve, Pat and Allen, for make the ZEUS implementation a top priority. Lastly I thank my committee members Riccardo Giovanelli, Robert Brown, and Eanna Flanagan, for their many helpful comments on an earlier draft of this manuscript.

On the personal side, I also thank Harvey and Karen for the home cooking and good cheer that kept me going while I finished up, and Mom, Dad, and Megan, for their love and support throughout.

I would not have succeeded in this work without the unwavering support of Lara, who stood with me through the many highs and lows of this long journey, displaying a compassionate understanding that still amazes me. I dedicate this dissertation to her.

TABLE OF CONTENTS

Biographical Sketch	iii
Dedication	v
Acknowledgements	vi
Table of Contents	viii
List of Tables	xi
List of Figures	xii
1 Introduction and Overview	1
2 Background and Scientific Motivation	3
2.1 Photodissociation Regions	3
2.1.1 [CI] Observations	7
2.1.2 Mid-J CO Observations	8
2.2 Observing Program	10
2.2.1 Starburst Galaxies	11
2.2.2 Ultraluminous Infrared Galaxies	12
2.2.3 Luminous, Dusty Galaxies at High Redshift	14
2.2.4 First Sources: NGC 253 and MIPS J142824.0+352619	18
3 Instrument Overview: Optical and Cryogenic Design	20
3.1 Introduction	20
3.1.1 Coherent vs. Direct-Detection	20
3.1.2 Spatial vs. Spectrally Multiplexing	22
3.2 Grating Design	22
3.3 Optics	26
3.4 Dewar	27
3.5 ³ He Refrigerator	29
3.6 Filtration	34
4 Detectors and Electronics	36
4.1 Introduction	36
4.2 Implementation	37
4.3 Electronics and Software	38
4.4 Bolometer Characterization	39
4.4.1 Dark Load Curves	41
4.4.2 Unblanked Load Curves	42
4.5 System Transmission	48
4.6 Noise Contributions	51
4.6.1 Photon Noise	51
4.6.2 Detector Noise	53
4.6.3 Amplifier Noise	54
4.6.4 Measured Noise	55

4.7	Sensitivity Estimate	56
4.7.1	Comparison with the Background Limit	58
4.7.2	Comparison with Heterodyne Receivers	59
5	Beam Coupling and Calibration	61
5.1	Beam Coupling	61
5.1.1	Coupling Terms and Definitions	61
5.1.2	Estimate of η_{tel}	62
5.1.3	Estimate of η_{fss}	63
5.1.4	Contributions to η_{fss}	65
5.1.5	Beam Mapping	67
5.2	Calibration	70
5.2.1	Flux Calibration	70
5.2.2	Spectral Calibration	72
5.2.3	Sky Subtraction	73
6	The Warm, Dense Molecular Gas in the Starburst Nucleus of NGC 253	75
6.1	Introduction	75
6.2	Observations	76
6.3	Results: CO Excitation Analysis	77
6.3.1	LVG Model	77
6.3.2	High Excitation Component	80
6.3.3	Low Excitation Component	83
6.3.4	Comparison with Atomic Gas	83
6.4	Discussion: What Heats the Gas?	85
6.4.1	X-Rays	85
6.4.2	Cosmic Rays	86
6.4.3	Shocks	86
7	Photodissociated Molecular Gas in MIPS J142824.0+352619	89
7.1	Introduction	90
7.2	Results	94
7.2.1	[CII], CO, and the FIR Continuum: A Comparison to Starburst Galaxies	94
7.2.2	PDR Analysis	97
7.2.3	Comparison to M82: MIPS J1428 as a Scaled-Up Starburst Galaxy	103
7.3	Discussion	105
7.3.1	[CII], CO, and the FIR Continuum: A Comparison with ULIRGs	105
7.3.2	[CII] Emission from High-Redshift Quasars	108
7.3.3	An Extended Starburst?	109
7.3.4	Evolution of High-Redshift Galaxies: Connection to Massive Ellipticals	113

7.4	Conclusions	113
A	Large Velocity Gradient	115
	Bibliography	118

LIST OF TABLES

2.1	Selected Extragalactic Probes Available to ZEUS	10
2.2	Redshift Coverage for Far-Infrared Fine-Structure Line Observations with ZEUS	16
3.1	ZEUS Resolving Power	26
3.2	Elements in the ZEUS Optical Train	35
4.1	ZEUS Bolometer Parameters	44
4.2	ZEUS/CSO Sensitivity	57
5.1	ZEUS/CSO Beam Parameters	70
6.1	NGC 253 CO Line Intensities	81
7.1	MIPS J142824.0+352619 Observations	91

LIST OF FIGURES

2.1	PDR Schematic	5
2.2	Star Formation History of the Universe	17
3.1	Submillimeter Atmospheric Transmission	23
3.2	ZEUS Grating Efficiency	25
3.3	ZEUS Optical Layout	28
3.4	ZEUS Cryostat	30
3.5	³ He Refrigerator	32
4.1	ZEUS Electronics Schematic	40
4.2	Dark Load Curves	43
4.3	Unblanked Load Curves	46
4.4	Full System Optical Transmission	49
5.1	ZEUS/CSO Skydips	64
5.2	ZEUS/CSO Beam Map	69
6.1	HCN $J = 1 \rightarrow 0$ and 6 cm Maps of NGC 253	78
6.2	NGC 253 CO Spectra	79
6.3	CO Rotational Level Diagram	80
6.4	Results of LVG Analysis	84
7.1	MIPS J142824.0+352619 [CII] Spectrum	90
7.2	$L_{\text{FIR}}/L'_{\text{CO}}$ vs. L_{FIR} in Local and High-Redshift Galaxies	93
7.3	$Y_{[\text{CII}]}$ vs. Y_{CO} in Nearby Galaxies	96
7.4	PDR Ratio Plot: CO(3 \rightarrow 2)/CO(2 \rightarrow 1)	98
7.5	PDR Ratio Plot: [CII]/FIR continuum	100
7.6	PDR Plot: Absolute [CII] Intensity	101
7.7	$Y_{[\text{CII}]}$ vs. Y_{CO} from ISO	107
7.8	$L_{[\text{CII}]} / L_{\text{FIR}}$ vs. L_{FIR} in Local and High-Redshift Galaxies	110

CHAPTER 1

INTRODUCTION AND OVERVIEW

In a normal spiral galaxy like our own about 90% of the baryonic mass is contained in stars, and the rest is distributed in the gas and dust that comprise the interstellar medium (ISM). About 1% of the ISM mass is in dust, and the rest in gas distributed in one of a few distinct components. Most of the gas is atomic, divided between the warm neutral medium (WNM) with $n \sim 0.5 \text{ cm}^{-3}$ and $T \sim 8000 \text{ K}$, and the cold neutral medium (CNM) with $n \sim 30 \text{ cm}^{-3}$ and $T \sim 80 \text{ K}$. These two phases represent the two dynamically stable solutions for gas in pressure equilibrium at $P/k_B \approx 3 \times 10^3 \text{ cm}^{-3} \text{ K}$. A small fraction of the gas is ionized, found in the warm ionized medium (WIM) with n and T similar to the WNM, and in the low density, hot ionized medium (HIM) that fills most of the galactic volume. Ionized gas is also found in the transient HII regions that form near massive stars.

The second most massive reservoir of gas is the molecular component, most of which resides in massive ($M \sim 10^5 M_\odot$) Giant Molecular Clouds (GMCs). Unlike the atomic clouds, these GMCs are self-gravitating, resulting in internal pressures as high as $P/k_B \sim 10^7 \text{ cm}^{-3} \text{ K}$. The large columns of dust mixed with the gas shield the clouds from UV radiation, allowing the interiors to cool, and it is the cold ($T \sim 10 \text{ K}$), dense ($n \sim 10^6 \text{ cm}^{-3}$) cores at the centers of GMCs that condense to form stars. The stellar radiation emerges as infrared dust continuum and gas cooling line emission, and we use observations of this line emission to probe the physical conditions of the gas, and to infer the intensity of the stellar radiation fields.

This dissertation is concerned with a study of the warm, dense molecular gas

in the starburst nucleus of the nearby galaxy NGC 253, and in the distant luminous infrared galaxy MIPS J142824.0+352619. This work is made possible by observations conducted with the redshift (z) and Early Universe Spectrometer (ZEUS), a new submillimeter wavelength spectrometer. The design, construction, and implementation of this instrument required a considerable amount of time and effort on the part of myself and the ZEUS team, and occupies a large portion of this dissertation, which is organized as follows. In chapter 2 we provide the scientific background and motivation for this project. In chapter 3 we describe the spectrometer and cryostat, in chapter 4 the detectors and electronics, and in chapter 5 the optical coupling to the telescope and sky. In chapter 6 we present our $^{13}\text{CO } J = 6 \rightarrow 5$ detection from NGC 253, model the excitation of the molecular gas, and discuss potential heat sources. In chapter 7 we present our detection of the [CII] $^2\text{P}_{3/2} \rightarrow ^2\text{P}_{1/2}$ fine-structure line from the $z = 1.325$ luminous infrared galaxy MIPS J142824.0+352619, obtain estimates of the gas density and the strength of the ambient stellar radiation field, and discuss the implications.

CHAPTER 2

BACKGROUND AND SCIENTIFIC MOTIVATION

We have constructed a submillimeter wavelength spectrometer, ZEUS, to study the gas-phase ISM in star-forming galaxies at low and high redshift. Nearby systems will be observed in the $370 \mu\text{m}$ [CI] fine-structure transition, and in the mid- J ¹ CO rotational transitions. High-redshift galaxies will be studied through observations of far-infrared fine-structure line emission, particularly in the [CII] $158 \mu\text{m}$ transition. We begin this introductory chapter with a description of photodissociation regions (PDRs), which produce most of the [CII] emission in galaxies, and also emit strongly in the [CI] and CO transitions. We then outline our observing program to study local starburst galaxies, Ultraluminous Infrared Galaxies, and dusty galaxies at high redshift, and describe how ZEUS observations will be used to address some of the key questions concerning these systems.

2.1 Photodissociation Regions

When massive stars are formed near a molecular cloud, their ultraviolet (UV) radiation strongly affects the thermal and chemical properties of the cloud surface. The incident far-UV (FUV; $6 \text{ eV} < h\nu < 13.6 \text{ eV}$) flux photodissociates the gas in the outer layer, and photoionizes the species such as carbon which have ionization potentials less than 13.6 eV . The gas in this region is heated to high temperatures by photoelectric heating, in which $\sim 1\%$ of the FUV radiation absorbed by dust produces energetic electrons which collisionally heat the gas. Somewhat deeper into the cloud the gas becomes molecular, but still has

¹In this chapter we use the term ‘mid- J ’ to describe transitions with $J_{\text{upper}} = 6 - 8$.

a higher temperature than in the FUV-shielded core. The result is that the surface of the molecular cloud is transformed into a region of warm atomic and molecular gas that produces bright cooling line emission.

Detailed photo-chemical PDR modeling was first done by [120], who consider FUV radiation incident on a uniform density slab. This basic model has been subsequently refined by many groups to account for such effects as clumpy density structure and time-dependent chemistry (for a comparison of the many PDR codes see [97]), but it is sufficient to capture the important physics, and we describe it here. A PDR schematic is presented in Figure 2.1, which shows the gas temperature and the states of hydrogen, carbon, and oxygen as a function of depth into the cloud. The penetration of FUV photons is limited by dust extinction, and the natural unit for describing the position in the PDR is the corresponding visual extinction, A_V , measured from the ionic/atomic transition. At small A_V the carbon is ionized, and photoelectric heating raises the gas temperature to $T \sim 100 - 1000$ K, depending on the incident FUV flux (parameterized as $F_{\text{FUV}} = G_0 \times [1.6 \times 10^{-3}] \text{ ergs cm}^{-2} \text{ s}^{-1}$) and the gas density (n). At $A_V \approx 4$ the FUV energy density is sufficiently reduced that carbon becomes neutral, and there is a sharp $\text{C}^+/\text{C}^0/\text{CO}$ transition. Since oxygen is more abundant than carbon in the ISM, the oxygen not bonded into CO remains atomic until $A_V \approx 10$, where it forms O_2 and the PDR formally ends.

At $A_V \lesssim 6$ the gas is heated by photoelectric heating, in which a fraction of the FUV photons absorbed by dust grains and PAH molecules cause the ejection of an energetic electron, which collisionally heats the gas. The efficiency of this heating process is negatively correlated with the grain charge; at higher grain charges the work function (and the ionization potential of the PAH molecules)

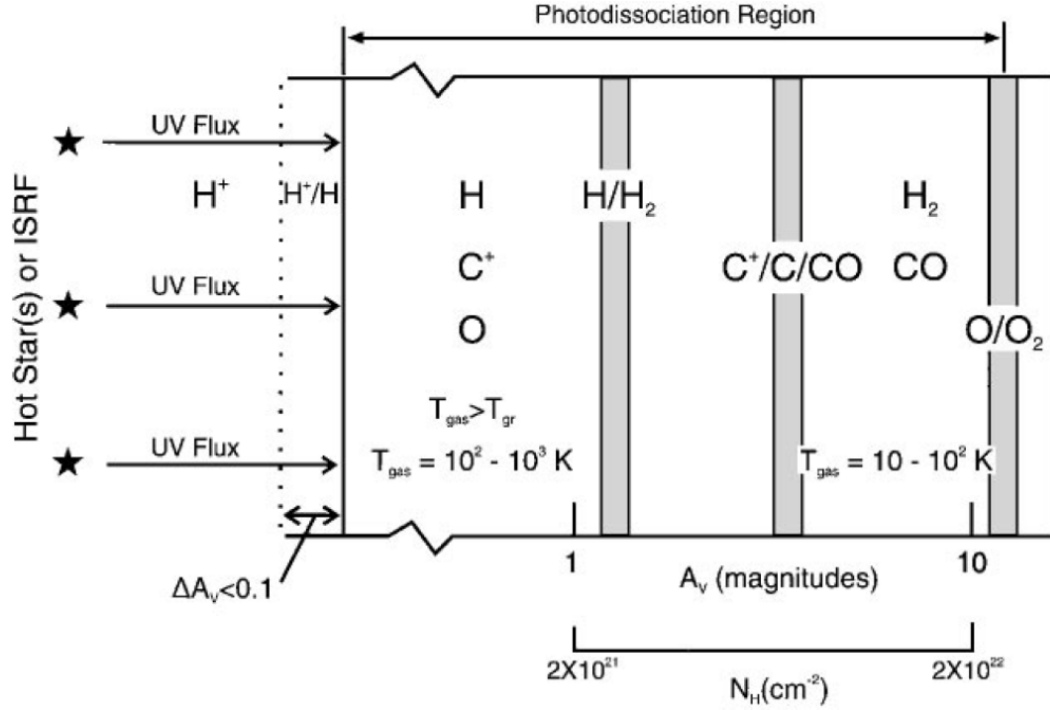


Figure 2.1: Schematic diagram of a photodissociation region from [51].

increases, and a smaller fraction of the FUV energy is transferred to the gas. Higher gas densities increase the electron recombination rate and decrease the net charge of the grain, such that the grain charge is determined by the ratio G_0/n , with higher ratios resulting in lower gas heating efficiencies. At small A_V the cooling is dominated by emission in the [CII] $158 \mu\text{m}$ and the [OI] $63 \mu\text{m}$ fine-structure lines, so the fraction of the bolometric emission contained in these two lines is equal to the gas heating efficiency, and traces the ratio G_0/n . The [OI] $63 \mu\text{m}$ transition has a higher excitation potential and a higher critical density² than the [CII] transition, such that the $F_{\text{[OI]}}/F_{\text{[CII]}}$ ratio increases for hotter (higher G_0) or denser PDRs. Beyond the $\text{C}^+/\text{C}^0/\text{CO}$ transition the rotational lines of CO dominate the gas cooling. At the transition the gas temperature is $T \sim 100 \text{ K}$

²Density at which the spontaneous emission rate matches the collisional de-excitation rate. At densities lower than n_{crit} each collisional excitation is followed by a radiative decay, such that the intensity is proportional to the collisional excitation rate, which scales as n^2 . At densities higher than n_{crit} the energy levels are populated according to thermal equilibrium, and the intensity is proportional to n .

and the mid- J states are populated, resulting in strong $J = 6 \rightarrow 5$ and $J = 7 \rightarrow 6$ emission.

One of the best studied Galactic PDRs is found in the Orion star-forming region, at the interface between the M42 nebula and the background GMC. This region provided the first detections of the [CII] and [OI] fine-structure lines, and was subject to the first detailed PDR modeling [119, and references therein]. FUV emission from the Trapezium stars at a distance of $\approx 0.1 - 0.2$ pc in front of the molecular cloud illuminates the neutral gas with a flux characterized by $G_0 \sim 10^5$, heating the gas to a peak temperature of ~ 500 K. The fine-structure line radiation from the primary coolants is well modeled by a PDR with a gas density of $n \sim 10^5 \text{ cm}^{-3}$. Mapping of the [CII] emission over the interface region shows that it correlates well with the CO $J = 1 \rightarrow 0$ distribution, further supporting the conclusion that the [CII] emission arises from the photodissociated surface of the molecular cloud [110].

PDR models are generally successful at modeling the observed emission from star-forming regions, particularly the intensities of the dominant [CII] and [OI] coolants, and their ratio with the far-infrared (FIR) continuum. Averaged over a galaxy, an important fraction of the total ISM is estimated to be traced by the [CII]-emitting regions of PDRs. For nearby spiral galaxies, [109] estimate that these regions account for 3% – 15% of the total molecular gas mass, while for starburst nuclei this increases to as large as $\approx 40\%$. In addition to PDRs, [CII] emission may arise from diffuse atomic gas, atomic clouds, compact HII regions, and extended low-density HII regions, but on a galactic scale the PDR component is expected to dominate [15, 109].

2.1.1 [CI] Observations

Neutral carbon in the electronic ground state produces emission in two fine-structure transitions: the ${}^3P_2 \rightarrow {}^3P_1$ ($\lambda = 370 \mu\text{m}$) transition connects the $J = 2$ and $J = 1$ excited states, and the ${}^3P_1 \rightarrow {}^3P_0$ ($\lambda = 609 \mu\text{m}$) transition connects the $J = 1$ state to the $J = 0$ ground level. Plane-parallel PDR models predict that emission in both lines will arise from a narrow region at the $C^+/C^0/\text{CO}$ transition, located at a depth of $A_V \approx 4$ into the neutral gas. The first observations of [CI]($1 \rightarrow 0$) in Galactic molecular clouds found emission which was much more widespread than expected, however, suggesting that C^0 is well mixed in molecular cloud interiors [93, 61, 62]. One explanation for this extended [CI] emission is that molecular gas is clumpy, such that UV photons penetrate the cloud to larger mean optical depths than would be predicted for a homogeneous medium [113]. In some of these systems, such as M17 SW and Orion A, the [CII] emission is similarly extended, supporting this picture of enhanced UV penetration through a clumpy medium [113, 110].

Observations of the Galaxy and nearby galaxies have shown that the total emission in the [CI] lines is comparable to that in the CO transitions, thereby demonstrating the importance of C^0 as a global coolant [25, 32]. The first detections of the [CI]($1 \rightarrow 0$) transition in the nearby starburst galaxies M82 and NGC 253 were used to derive abundance ratios of $[C^0]/[CO] \sim 0.5$ [101, 125, 45, 58, 44], much larger than the value of ~ 0.1 measured in Galactic molecular clouds [128]. More recent observations of a larger sample of galaxies have shown that $[C^0]/[CO] \sim 1$ may be a common feature of galactic nuclei [57]. One possible explanation of this enhanced abundance ratio is that the [CI] and CO emission in galactic nuclei arise in regions which are not as well

shielded from UV radiation as are the dense cores in Galactic molecular clouds, such that a larger fraction of the CO is photodissociated [57]. A second explanation is that the emission arises in gas with a high ionization fraction, which may drive the chemistry to equilibrium with a large $[C^0]/[CO]$ value [45, and references therein].

Most observations of neutral carbon utilize the $[CI](1 \rightarrow 0)$ transition, which is easier to detect with the currently available instrumentation. However, observations of the $[CI](2 \rightarrow 1)$ transition have shown that the ratio of the two lines is a sensitive probe of the physical conditions of the gas. Both lines have modest critical densities ($n_{\text{crit}} \approx [0.3 - 1.1] \times 10^3 \text{ cm}^{-3}$), and are therefore often thermalized in molecular clouds ($n_{\text{H}_2} \gtrsim 10^3 \text{ cm}^{-3}$). They arise from states with energy levels 24 K and 62 K above ground, such that their ratio is sensitive to the gas temperature if $T \lesssim 100 \text{ K}$. The first observations of $[CI](2 \rightarrow 1)$ in Galactic molecular clouds were combined with previous detections of $[CI](1 \rightarrow 0)$ to show that both lines are likely optically thin, and that the excitation temperatures are $T_x \approx 30 - 80 \text{ K}$ [128]. The two lines have been measured simultaneously in M82 [112], and the large ratio indicates $T_{\text{kin}} > 50 \text{ K}$ and $n \gtrsim 10^4 \text{ cm}^{-3}$. Aside from M82, however, $[CI](2 \rightarrow 1)$ has been detected in only a few galaxies (in the local Universe) [2, 3], so the excitation of neutral carbon in galaxies has yet to be fully characterized.

2.1.2 Mid-J CO Observations

The $J = 6 \rightarrow 5$ and $J = 7 \rightarrow 6$ transitions of CO arise from states with energy levels 116 K and 155 K above ground and have critical densities $n_{\text{crit}} \approx 3 \times 10^5$

cm^{-3} , and are thus sensitive probes of warm, dense molecular gas. The layer of warm CO found at the C^0/CO transition in dense PDRs is expected to produce bright mid-J CO emission. This can be seen in observations of CO $J = 7 \rightarrow 6$ in the Orion molecular cloud and interface region, in which the $J = 7 \rightarrow 6$ intensity peaks at the interface region and shows a good spatial correspondence with the $J = 1 \rightarrow 0$ and [CII] maps. Velocity resolved studies of the interface show that the $J = 7 \rightarrow 6$, $J = 1 \rightarrow 0$, and [CII] lines also have similar spectral profiles, strongly suggesting a common PDR origin for all 3 tracers [102, 110, 53].

In addition to the FUV-heated gas in PDRs, shock-heated gas may also produce strong mid-J CO emission. Stellar outflows in the massive star formation regions W51 and DR 21 produce luminous, broad-lined CO $J = 7 \rightarrow 6$ emission that dominates over the narrow-lined PDR component [59]. The CO $J = 7 \rightarrow 6$ emission from the circumnuclear disk in the Galactic center also arises in dynamically-heated gas, in this case by the dissipative decay of turbulence [9].

The FIRAS experiment on the Cosmic Background Explorer (COBE) satellite detected emission in the CO $J = 1 \rightarrow 0$ through $J = 8 \rightarrow 7$ transitions in the central region of the Galaxy, and found that the brightest line was $J = 4 \rightarrow 3$ [25]. The density and kinetic temperature required to significantly populate a CO rotational level both increase with J (see Fig. 6.3), such that the brightest CO transition in a system is a reflection of the gas excitation. A recent study of the CO cooling curves in a sample of nearby galaxies found that the brightest CO transitions are $J = 4 \rightarrow 3$ and $J = 5 \rightarrow 4$ in normal galactic nuclei [3], suggesting similar excitation as in the Galaxy. The ISM in the centers of starburst galaxies is more highly excited, such that the $J = 6 \rightarrow 5$ and $J = 7 \rightarrow 6$ transitions are the

Table 2.1: Selected Extragalactic Probes Available to ZEUS

Species	Transition	E_{upper}/k_B (K) ^a	λ (μm)	A (s^{-1}) ^b	n_{crit} (cm^{-3}) ^c
O ⁰	$^3\text{P}_1 \rightarrow ^3\text{P}_2$	228	63.184	8.9×10^{-5}	8.5×10^5
O ⁺⁺	$^3\text{P}_1 \rightarrow ^3\text{P}_0$	163	88.356	2.6×10^{-5}	5.1×10^2
C ⁺	$^2\text{P}_{3/2} \rightarrow ^2\text{P}_{1/2}$	91	157.741	2.3×10^{-6}	2.8×10^3
N ⁺	$^3\text{P}_1 \rightarrow ^3\text{P}_0$	70	205.178	2.1×10^{-6}	4.4×10^1
C ⁰	$^3\text{P}_2 \rightarrow ^3\text{P}_1$	62	370.414	2.7×10^{-7}	1.1×10^3
¹² CO	$J = 8 \rightarrow 7$	199	325.225	5.5×10^{-5}	6.5×10^5
	$J = 7 \rightarrow 6$	155	371.650	3.7×10^{-5}	4.4×10^5
	$J = 6 \rightarrow 5$	116	433.556	2.3×10^{-5}	2.8×10^5
¹³ CO	$J = 8 \rightarrow 7$	190	340.181	4.8×10^{-5}	5.7×10^5
	$J = 6 \rightarrow 5$	111	453.498	2.0×10^{-5}	2.5×10^5

^aEnergy of the upper level above ground in units of degrees Kelvin.

^bEinstein spontaneous emission coefficient.

^cThe critical densities of the CO transitions are calculated by equating the spontaneous emission rate with the collisional de-excitation rate from the upper level to the lower level [111], while for the atomic transitions we include collisional depopulation of the upper level to all other levels [86]. We assume CO and C⁰ are excited by collisions with H₂ molecules, C⁺ and O⁰ by collisions with H atoms, and N⁺ and O⁺⁺ by collisions with electrons.

brightest CO lines in these systems [3].

2.2 Observing Program

The broad wavelength coverage of ZEUS allows us access to important cooling lines emitted by galaxies in the local Universe and at high redshift (Table 2.1). In nearby starburst galaxies and Ultraluminous Infrared Galaxies (ULIRGs) we will observe mid-J CO rotational emission and [CI] fine-structure line emission, and use these observations to model the physical conditions of the warm molecular gas and to address these key questions: How does the central starburst interact with the natal ISM, and does this interaction help or hinder further star formation? What is the origin of the [CII] deficit in ULIRGs? We will also observe FIR fine-structure line emission from dusty galaxies at high redshift, most

importantly the [CII] transition, which we can use to estimate the intensities of the UV fields powering these systems. Are submillimeter galaxies indeed powered by bursts of star formation, and if so, how intense are these starbursts?

2.2.1 Starburst Galaxies

Star formation in our Galaxy occurs in molecular clouds distributed throughout the ~ 30 kpc disk. A total gas mass of $M_{\text{gas}} \sim 10^{10} M_{\odot}$ is producing stars at a rate of $\sim 4 M_{\odot} \text{ yr}^{-1}$, corresponding to a gas depletion timescale of $\sim 2 \times 10^9$ yr. This is an appreciable fraction of the $\sim 10^{10}$ yr age of the Galaxy, and is consistent with the picture of a steady star formation history.

In the central $\sim 0.1 - 1$ kpc regions of many nearby galaxies, however, stars are being formed at comparable rates out of much smaller gas reservoirs. This enhanced star formation efficiency results in shorter depletion timescales of $\sim 10^8$ yr, indicating that these are temporary phenomena, which are often referred to as 'starbursts'. This high efficiency is the result of a large central gas concentration, typically created by a merger/interaction with a nearby system, or by the channeling of material to the nucleus with the aid of a stellar bar. Starburst nuclei are an important component of local stellar production, with an estimated $\sim 25\%$ of all high mass star formation within 10 Mpc occurring in just 4 starburst galaxies (M82, NGC 253, M83, and NGC 4945) [46]. It is therefore important to understand these systems to provide a complete census of local star formation.

Nearby starburst nuclei also offer an excellent opportunity to study the physical processes at work in environments of enhanced star formation, includ-

ing an examination of the interaction between the young stars and the surrounding ISM. As an example, [8] use observations of the CO line intensities to model the excitation of the molecular gas in the starburst nucleus of NGC 253. They find that the bulk of the $\sim (2 - 5) \times 10^7 M_{\odot}$ of gas in the central 180 pc is warm ($T \sim 120$ K) and dense ($n_{\text{H}_2} \sim 10^{4.5} \text{ cm}^{-3}$), and that this is far too much mass to be heated by UV photons in PDRs. It is more likely that cosmic rays produced by the many supernovae in the nucleus penetrate the cores of molecular clouds and heat the full volume of molecular gas, rather than just the photodissociated cloud surfaces. Studies such as this help us to better understand the starburst phenomenon, and these systems may serve as useful templates for star-forming galaxies at higher luminosity and redshift.

2.2.2 Ultraluminous Infrared Galaxies

One of the most exciting results from the Infrared Astronomy Satellite (IRAS) was the detection of a new class of galaxies that emit the bulk of their radiation at infrared wavelengths. At bolometric luminosities greater than $2 \times 10^{11} L_{\odot}$ these infrared galaxies become the dominant population in the local Universe [107]. At the high luminosity end are the Ultraluminous Infrared Galaxies (ULIRGs), formally defined as objects with $L_{\text{IR}} \geq 10^{12} L_{\odot}$. Follow-up study has shown that nearly all ULIRGs are advanced mergers between gas-rich spirals, and contain massive central concentrations of gas and dust [99]. The infrared luminosity is a direct result of the merger, which triggers either an extreme burst of star formation and/or accretion onto a central black hole (an active galactic nucleus [AGN]). While the relative importance of the two energy generation mechanisms has been debated since their discovery, most ULIRGs are now thought

to be powered primarily by star formation, although many also contain a luminous AGN [31, 24].

While ULIRGs may be powered by star formation, the physical conditions in these sources are quite different from those in the nuclei of lower luminosity starburst galaxies. One of the surprising results from the Infrared Space Observatory (ISO) mission was the discovery that the ratio of the [CII] line to FIR continuum emission in ULIRGs is ~ 7 times weaker than in lower luminosity systems [73], in which the [CII] cooling accounts for 0.1 – 1% of the total FIR luminosity [109]. This [CII] deficit may be understood if the emission is produced in PDRs which are either illuminated by intense FUV fields or have high gas densities, which would reduce the fraction of the FIR luminosity emerging in the gas cooling lines and/or shift the cooling budget to the [OI] $63 \mu\text{m}$ transition. An alternative explanation is that the PDRs in ULIRGs and starburst galaxies are similar, but that the continuum emission from ULIRGs is produced in a non-PDR component that dilutes the global $L_{\text{[CII]}}/L_{\text{FIR}}$ ratio [73].

Observations of [CI] and the mid-J CO lines provide a means of testing these scenarios. If the [CII] deficit is only an apparent affect produced by a dominant non-PDR source of FIR continuum, then we would expect to see the line to continuum ratios of CO, [CI], and [CII] reduced by similar amounts. If in fact the [CII] deficit is caused by PDRs with large values of n or G_0 , then we would expect to see these line ratios change accordingly. As an example, [89] recently reported the detection of CO $J = 6 \rightarrow 5$ emission in the ULIRG Mrk 231, and find that the total CO cooling approaches that of [CII]. This is quite different from the case in most galaxies, where the [CII] cooling dominates [3]. The low $F_{\text{[CII]}}/F_{\text{CO}}$ and $F_{\text{[CII]}}/F_{\text{FIR}}$ ratios in Mrk 231 may be explained by a high PDR gas

density, which has the effect of moving the $C^+/C^0/CO$ transition to lower A_V , thereby reducing the C^+ column and increasing the surface temperature of the CO layer [89]. This high density scenario can be tested with observations of the CO $J = 7 \rightarrow 6$ and [CI](2 \rightarrow 1) lines at $371 \mu\text{m}$, which have critical densities of $4.4 \times 10^5 \text{ cm}^{-3}$ and $1.1 \times 10^3 \text{ cm}^{-3}$, respectively. The $F_{CO(7 \rightarrow 6)}/F_{[CI](2 \rightarrow 1)}$ ratio is therefore a sensitive density probe, increasing by an order of magnitude in PDRs as the density is increased from 10^3 cm^{-3} to 10^5 cm^{-3} [60].

2.2.3 Luminous, Dusty Galaxies at High Redshift

While ULIRGs dominate the high end of the local luminosity function, they account for only a small fraction of the infrared energy density [106]. This picture changes at earlier times, however, where a cosmologically significant population of ultraluminous infrared galaxies has been discovered at $z \sim 2$.

The existence of infrared-luminous galaxies at high redshift was implied by the COBE satellite's detection of a Cosmic Infrared Background (CIB), which peaks at $\approx 200 \mu\text{m}$ and contains an energy density comparable to that in the optical background [26, 18]. Since the discovery of the CIB, many surveys at mid-IR through millimeter wavelengths have been undertaken in an attempt to resolve the underlying galaxy population. Some of the most successful of these surveys have used the SCUBA camera on the James Clerk Maxwell Telescope (JCMT) to identify a large population of dusty, high-redshift galaxies through deep integrations at $850 \mu\text{m}$. The number counts of these submillimeter galaxies (SMGs) can directly account for $\approx 60\%$ of the CIB at $850 \mu\text{m}$, and with a reasonable extrapolation of the counts below the detection limit, the full CIB is

reproduced [105].

One of the most complete samples of SMGs was assembled by [13], who combined radio interferometry and optical spectroscopy to measure the redshifts of 73 SMGs. This radio-detected sample has a median redshift of $z = 2.2$, and a median total IR luminosity (integrated between 8 and 1100 μm) of $L_{\text{TIR}} = 8.5 \times 10^{12} L_{\odot}$. As with ULIRGs in the local Universe, the large dust obscuration in these sources makes it difficult to unambiguously rule out the presence of an energetically dominant AGN. However, the UV/optical spectra of this sample, combined with the X-ray fluxes and size estimates of the general SMG population, imply that less than $\approx 30\%$ of the IR luminosity is powered by AGN activity [13, and references therein]. Converting the remaining luminosities into star formation rates, the star formation rate density (SFRD; activity per unit co-moving volume) of bright SMGs is obtained as a function of redshift. This is compared with estimates of the SFRD obtained through observations at other wavelengths in Figure 2.2. Although the SFRD of bright SMGs only accounts for the most luminous of the IR galaxy population, it is still comparable to the SFRD inferred from observations of the rest-frame UV emission of galaxies at $z \sim 2 - 3$. Extrapolation of the SMG number counts to include fainter sources (small squares and dashed line in Fig. 2.2) suggests that infrared-luminous galaxies may dominate the star formation activity at $z \sim 2$, with a peak SFRD more than an order of magnitude larger than in the local Universe.

The large SFRD found at $z \sim 2$ implies significant evolution of the IR energy density from $z = 0 \rightarrow 2$, and this is confirmed by observations in the mid-IR. For a sample of Spitzer MIPS 24 μm sources extracted from a blank field survey, [67] find that the IR energy density increases as $(1 + z)^{3.9}$ out to $z \sim 1$. This is caused

Table 2.2: Redshift Coverage for Far-Infrared Fine-Structure Line Observations with ZEUS

Transition	Redshift Interval			
	350 μm	450 μm	610 μm	870 μm
[OI] 63 μm	4.22 – 5.01	5.65 – 6.60		
[OIII] 88 μm	2.73 – 3.30	3.75 – 4.43		
[CII] 158 μm	1.09 – 1.41	1.66 – 2.04	2.63 – 3.06	4.23 – 5.09
[NII] 205 μm	0.61 – 0.85	1.05 – 1.34		

Note. – The redshift intervals shown for each transition correspond to the range currently accessed by ZEUS in the 350 and 450 μm telluric windows. We also show the intervals which could be accessed in the 610 and 870 μm windows for [CII] observations, achieved by operating the grating in 3rd and 2nd order.

primarily by an increase in the mean luminosity of the IR galaxy population, such that systems with $L_{\text{IR}} \geq 10^{11} L_{\odot}$ dominate the emission beyond $z \gtrsim 0.7$, and ULIRGs account for more than 10% of the energy production by $z = 1$. This is in contrast with the evolution of the UV luminosity density, which scales only as $(1+z)^{-2.5}$. Thus by $z \sim 1$ and beyond, ultraluminous infrared galaxies account for a significant fraction of the star formation activity.

While the infrared continuum flux traces the total luminosity, dust mass, and dust temperature, spectroscopy of redshifted FIR fine-structure lines can provide a wealth of information on the physical conditions of the gas, and on the nature of the ambient UV radiation fields. With ZEUS on the CSO, we can detect several of the brightest FIR fine-structure lines from distant galaxies when their redshifted wavelengths fall into the available submillimeter windows, including the [OI] 63 μm , [OIII] 88 μm , [CII] 158 μm , and [NII] 205 μm lines (Table 2.2).

Our primary diagnostic for distant galaxies is the 158 μm [CII] transition. This is the brightest line from most star-forming galaxies, where it dominates the cooling of photodissociated gas on the surfaces of molecular clouds. We

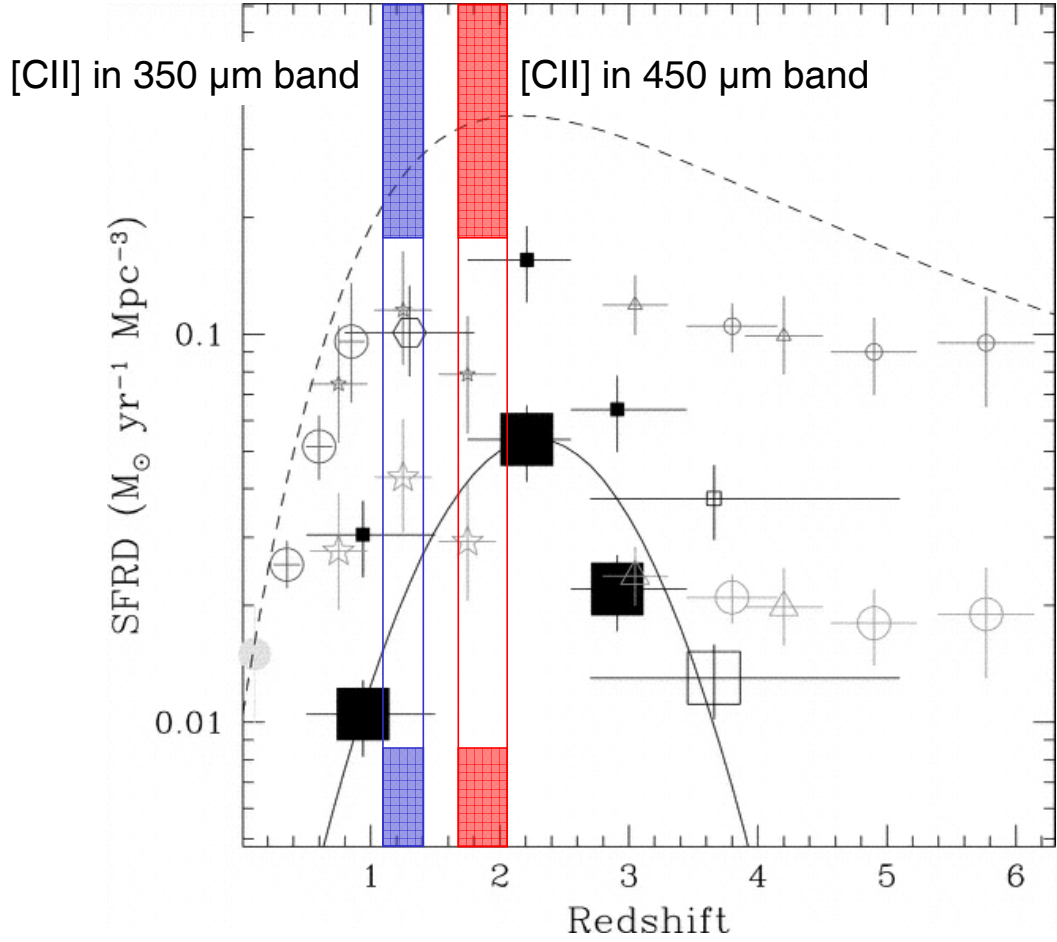


Figure 2.2: Evolution of the energy density (parametrized by SFRD) in the Universe with epoch from [13, and references therein]. The submillimeter measurements from [13] (*large squares*) are compared with the published estimates from optical/UV surveys and radio/IR tracers of the star formation density. The smaller symbols for the optical estimates indicate dust-corrected estimates. A Gaussian fit is shown for the four submillimeter galaxy points, tracing an evolution comparable to luminous radio-selected quasars. For the submillimeter sources, the smaller points show a simple redshift-independent correction to the luminosity density to match the submillimeter extragalactic background down to $F_{850 \mu\text{m}} = 1 \text{ mJy}$, below the detection limit used by [13]. The dashed line is the best fit for a simple parametric model constrained by the counts of sources in the FIR/submillimeter and the spectrum of the extragalactic background. The two partially filled columns show the redshift coverage corresponding to observing the [CII] $158 \mu\text{m}$ line in the 350 and 450 μm telluric bands.

can use ZEUS to begin a survey of the [CII] line emission from distant galaxies, which is shifted into our primary 350 and 450 μm telluric windows for redshifts of $z = 1.09 - 1.41$ and $z = 1.66 - 2.04$ (Fig. 3.1). Such a survey is critical to understanding the star formation history of the Universe, as it is within this $z \sim 1 - 2$ range that the star formation rate strongly evolves to its peak (Fig. 2.2). We will use the ratio $F_{\text{[CII]}}/F_{\text{FIR}}$ of the [CII] line to FIR continuum flux along with PDR modeling to constrain the strength of the ambient FUV field, G_0 (see Fig. 7.5), which is a reflection of the concentration of the starburst. Very high $G_0 \sim 10^5$ is associated with highly compact star-forming regions, such as the region hosting the Orion PDR, in which the gas is $\sim 0.1 - 0.2$ pc from the OB cluster. More modest values of $G_0 \sim 10^3$ are representative of starburst nuclei, while for normal galaxies with star formation distributed throughout the disk, $G_0 \sim 1 - 100$. For galaxies which are powered by an AGN, the intense FUV fields are expected to produce a small $F_{\text{[CII]}}/F_{\text{FIR}}$ ratio.

2.2.4 First Sources: NGC 253 and MIPS J142824.0+352619

In chapter 6 we present the first result from our program to characterize the molecular ISM in starburst galaxies, with a study of the nucleus of NGC 253. This is the nearest starburst galaxy, and is often considered to be an archetype which may be used as a template for more distant and luminous systems. It is the brightest extragalactic source of mid-J CO emission, and in addition to the main ^{12}CO isotopologue, we were able to detect emission in the ^{13}CO $J = 6 \rightarrow 5$ transition. The combination of both isotopologues enables a detailed excitation analysis, and facilitates a study of the stellar feedback mechanisms in this starburst.

In chapter 7 we present the first result from our high-redshift program, with a detection of [CII] emission at $z = 1.325$. MIPS J142824.0+352619 is a hyperluminous infrared galaxy ($L_{\text{FIR}} > 10^{13} L_{\odot}$) recently discovered by the MIPS instrument on the Spitzer satellite, and has been shown to be a starburst-dominated system with an apparent star formation rate of $\sim 5500 M_{\odot} \text{ yr}^{-1}$. As such, it is similar to the luminous, star-forming submillimeter galaxies found at comparable redshifts. It has been well studied from the optical through the radio, and our observations, combined with the literature data, allow for a detailed modeling of the PDRs powering this galaxy.

CHAPTER 3

INSTRUMENT OVERVIEW: OPTICAL AND CRYOGENIC DESIGN

In the previous chapter we presented the scientific case for an observing program to study far-infrared line emission from high-redshift galaxies, and submillimeter line emission from nearby systems. This project requires the construction of a sensitive submillimeter spectrometer optimized for detecting broad lines from extragalactic sources. In this chapter we justify the choice of a grating spectrometer, and describe the optical and cryogenic design of ZEUS.

3.1 Introduction

3.1.1 Coherent vs. Direct-Detection

Two different detection techniques are used in submillimeter astronomy: heterodyne systems coherently sample the incoming electromagnetic wave, while direct-detection systems measure the total power of the incident photons. Heterodyne receivers are routinely used for spectroscopy, and have made several extragalactic detections at high frequencies in recent years [124, 2, 3, 40, 89]. These systems can provide very high spectral resolution, and by retaining the phase information are also ideal for interferometry. However, this detection technique requires the simultaneous measurement of the amplitude and phase of the wave, and limits to the accuracy of this measurement are set by the Heisenberg uncertainty principle. As a consequence, heterodyne receivers produce an unavoidable quantum noise. Expressing this noise as the equivalent temperature of a radiation field which would produce the same noise, one

finds a minimum receiver temperature of $T_{\text{rx,qn}}(\text{DSB}) = 2h\nu/k_B = 82 \rightarrow 64$ K at $\lambda = 350 \rightarrow 450 \mu\text{m}$. The fundamental limit to the sensitivity of any spectrometer arises from fluctuations in the background photon arrival rate (see section 4.6.1), which corresponds to a noise temperature $T_{\text{bg}} = (\text{emissivity} \times \text{temperature}) \sim 150 - 200$ K at $\lambda = 350 - 450 \mu\text{m}$. Thus at short submillimeter wavelengths, the quantum noise term makes a significant contribution to the system noise in an otherwise background-limited system.

The backends used in heterodyne systems also suffer from limited bandwidth. Spectral line observations are currently limited to instantaneous bandwidths of ≈ 1.8 GHz [63, 89], corresponding to velocity widths of $\Delta v = 630 \rightarrow 810$ km s⁻¹ at $\lambda = 350 \rightarrow 450 \mu\text{m}$. Many submillimeter galaxies have linewidths as large as $\Delta v \sim 800$ km s⁻¹ [38], however, requiring a larger velocity coverage. Added bandwidth is also helpful for observing lines from distant galaxies whose redshifts may only be approximately known (e.g., from photometric redshifts, or redshifts from PAH features).

Direct-detection systems do not experience quantum noise and can be constructed with large bandwidths, and arrays of semiconductor bolometers are now routinely used for background-limited continuum observations [50, 19]. A background-limited spectrometer is more difficult to implement than a broadband instrument, however, due to the reduced power falling on each detector. The bolometers must be intrinsically low-noise, and care must be taken to filter out any unwanted radiation. Nevertheless, an earlier direct-detection submillimeter spectrometer, SPIFI, achieved sensitivities within factors of 1.5 – 3 of the background limit [10], and encouraged by this success we choose a direct-detection design for ZEUS.

3.1.2 Spatial vs. Spectrally Multiplexing

For background-limited operation the two spectrometer choices are a Fabry-Perot Interferometer (FPI) and a grating spectrometer. An FPI provides instantaneous two-dimensional spatial coverage in one spectral bin, and must be scanned to complete the spectrum. A grating spectrograph provides instantaneous spectra across a one-dimensional slit projected on the sky, and must spatially scan to produce a two-dimensional image. At the spatial resolution obtainable with the current class of submillimeter telescopes ($\lambda/D_{\text{tel}} \approx 7''$ at $350 \mu\text{m}$ on the CSO, corresponding to 2.7 kpc at $z = 0.02$ and 56 kpc at $z = 1.2$), high-redshift galaxies and even local ULIRGs are expected to be unresolved. Imaging capabilities are not required, and by choosing a spectrally multiplexed grating monochromator we simultaneously observe in several spectral bins, achieving large instantaneous bandwidth.

3.2 Grating Design

We begin our selection of the grating parameters by considering the spectral regions available in the short submillimeter wavelength regime. In Figure 3.1 we show the atmospheric transmission on Mauna Kea, which identifies our two primary telluric bands centered at 350 and $450 \mu\text{m}$. As discussed in chapter 2, these windows transmit the important $\text{CO}(6 \rightarrow 5)$, $\text{CO}(7 \rightarrow 6)$, $\text{CO}(8 \rightarrow 7)$, and $[\text{CI}](2 \rightarrow 1)$ lines, which are dominant coolants of the warm, dense molecular gas in local ULIRGs, and are thus of prime interest to our work (see Table 2.1). These windows also correspond to redshift bins of $z \approx 1.09 - 1.41$ and $z \approx 1.66 - 2.04$ for $[\text{CII}]$ observations, and access to these redshift bins allows us to study the evo-

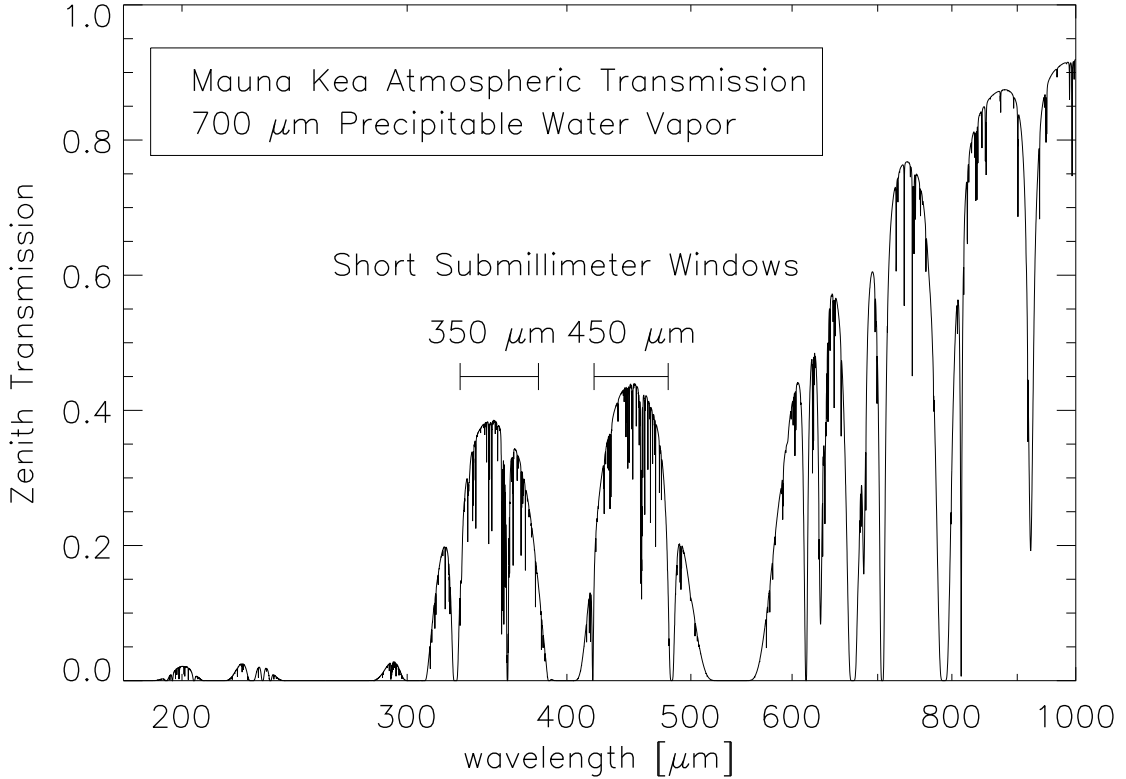


Figure 3.1: Submillimeter atmospheric transmission for a precipitable water vapor level of $700 \mu\text{m}$, a good night on Mauna Kea. ZEUS currently operates in the 350 and $450 \mu\text{m}$ telluric windows, and has access to the indicated ranges.

lution of the star formation history of the Universe from its peak at $z \sim 2.2$ to the current epoch (Fig. 2.2).

The resonance condition of a diffraction grating is described by the grating equation:

$$\frac{n\lambda}{d} = (\cos \gamma)(\sin \alpha + \sin \beta), \quad (3.1)$$

where n is the diffraction order, d is the groove spacing, α and β are the angles of incidence and diffraction with respect to the grating normal, and γ is the angle of the incident beam out of the dispersion plane. Thus a grating tuned to resonate at $355 \mu\text{m}$ in 5th order will also resonate at $444 \mu\text{m}$ in 4th order, giving us access to both the 350 and $450 \mu\text{m}$ telluric bands. Such combinations of resonances are also found in higher orders, but by remaining in low order the free spectral

range ($\delta\lambda = \lambda/n$) is $\approx 20\%$ at $350 \mu\text{m}$ and $\approx 25\%$ at $450 \mu\text{m}$, large enough to cover the $\approx 15\%$ wide telluric windows. With this design, the 610 and $870 \mu\text{m}$ windows can also be accessed by operating the grating in 3rd and 2nd order, respectively. A compact and efficient grating mounting configuration is Littrow mode, in which the incident and diffracted beams are cospatial (i.e., $\alpha = \beta$, $\gamma = 0$). We choose an R2 echelle (blazed at $\alpha = \tan^{-1}(2) = 63.4^\circ$), which then determines $d = 992 \mu\text{m}$ from equation 3.1. By rotating the grating over $\alpha = 57^\circ - 74^\circ$ the full 350 and $450 \mu\text{m}$ telluric bands can be covered.

For the background-limited observation of a spectral line of width $\delta\nu$, the detection sensitivity is maximized by selecting a resolving power of $R \approx c/\delta\nu$. We estimate a representative velocity width is $\delta\nu = 300 \text{ km s}^{-1}$ for our target sources, and choose $R = 1000$. The slit-limited resolving power of a grating spectrometer operated in Littrow mode is

$$R = \frac{2(\tan \alpha)G_{\text{proj}}}{\theta_{\text{slit}}D_{\text{tel}}}, \quad (3.2)$$

where G_{proj} is the diameter of the collimated beam incident on the grating, θ_{slit} is the angular size of the slit projected onto the sky, D_{tel} is the telescope diameter, and the above equation holds in the limit of $\theta_{\text{slit}} > \lambda/D_{\text{tel}}$. For background-limited observations of a point source, the sensitivity is maximized by selecting $\theta_{\text{slit}} = 1.2\lambda/D_{\text{tel}}$. As a compromise between satisfying this condition for our two primary windows we initially chose $\theta_{\text{slit}} = 8.7''$, corresponding to $1.2\lambda/D_{\text{tel}}$ at $\lambda = 364 \mu\text{m}$. To attain $R \approx 1000$ we illuminate the grating with a $G_{\text{proj}} = 10 \text{ cm}$ beam, giving $R = 1000$ at $\lambda = 361 \mu\text{m}$ and $\lambda = 451 \mu\text{m}$ (see Table 3.1). After it was discovered that the system was not fully background-limited we opened the slit to $10.8''$ to increase our sensitivity, which decreased the resolving power by 25%. We note that the $10.8''$ slit corresponds to λ/D_{tel} at $\lambda = 545 \mu\text{m}$, so equation 3.2 holds for the entire 350 and $450 \mu\text{m}$ bands.

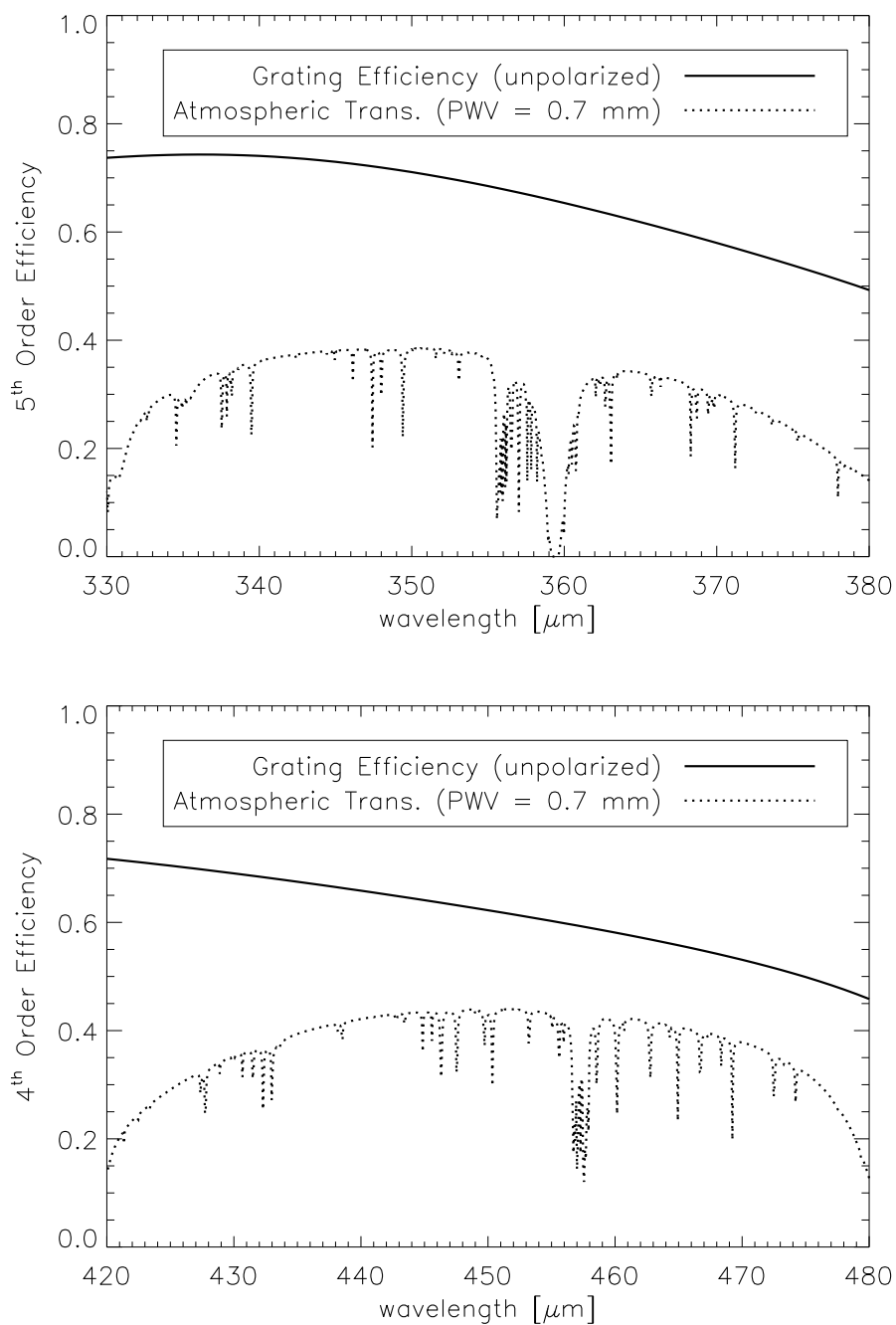


Figure 3.2: Grating efficiency superposed on the zenith atmospheric transmission in the 350 and 450 μm telluric windows. The plotted range shows the extent of our spectral coverage, limited by the range of incidence angles $\alpha = 57^\circ - 74^\circ$.

Table 3.1: ZEUS Resolving Power

α [degrees]	λ (5 th order) [μm]	λ (4 th order) [μm]	R^a	R^b
57	333	416	706	565
59	340	425	763	610
62	350	438	862	690
65	360	450	983	786
68	368	460	1134	908
71	375	469	1331	1065
74	381	477	1598	1279

Note. – Slit-limited resolving power of a grating spectrometer in which the grating is operated in Littrow mode, has a groove spacing of $d = 992 \mu\text{m}$, and is illuminated by a collimated beam with diameter $G_{\text{proj}} = D_{\text{tel}}/104$.

^a $\theta_{\text{slit}} = 8.7''$, used for initial observing runs in 2006.

^b $\theta_{\text{slit}} = 10.8''$, used for subsequent observing runs in 2007, 2008, and 2009.

We model the blaze efficiency of the grating using the program PC Grate-1E [37]. Figure 3.2 shows the predicted efficiency of the grating in Littrow mode in 5th order (350 μm) and 4th order (450 μm) for unpolarized light, which ranges from $\approx 45 - 75\%$ over the two bands. To accommodate a 10 cm beam at the steepest useful angle of $\alpha = 73^\circ$ requires the grating to be at least 100 mm wide and 342 mm long. The 126 mm \times 350 mm gold-coated, diamond-turned aluminum grating was manufactured by Zumtobel Staff GmbH (Austria).

3.3 Optics

The ZEUS detector array uses 1 mm \times 1 mm square pixels (see chapter 4), and the optics are designed to match this pixel size to a diffraction-limited beam on the sky. This is approximately achieved in the 350 and 450 μm bands by imaging onto the focal plane at $f/2.75$, corresponding to a plate scale of $7.2''/\text{pixel}$,

or λ/D_{tel} at $364 \mu\text{m}$. The optical layout inside the cryostat is shown in Figure 3.3. The telescope delivers an $f/12$ beam to the Nasmyth platform, and an elliptical/flat pair of foreoptics reimages the telescope focus to a location inside the entrance window, conserving the focal ratio. The beam is then passed through an f -converter stage consisting of two fold mirrors (M1 and M3) and two off-axis paraboloids (M2 and M4) in Czerny-Turner configuration, which reimages at $f/2.75$ onto the entrance slit of the echelle stage. The telescope secondary is imaged to a plane between M3 and M4, and baffles are placed here to form a Lyot stop.

The echelle is mounted in an Ebert-Fastie configuration, with a single off-axis paraboloid (M5) serving as both collimator and camera. The center of M5 is offset from the plane of the M1 – M4 section, such that the 10 cm collimated beam is incident on the grating with a small angle out of the dispersion plane, and the diffracted beam returns to M5 offset in the cross-dispersion direction. This quasi-Littrow mode of operation separates the image from the entrance slit, and allows the introduction of a flat pickoff mirror (M6) to direct the beam onto the detector. The Zemax ray-trace program was used to assist the optical design, and shows diffraction-limited spot sizes over the $1 \text{ mm} \times 32 \text{ mm}$ focal plane. All mirrors are gold-plated, diamond-turned aluminum with a protective SiO coating.

3.4 Dewar

The dewar was originally constructed for the KEGS instrument [48] by Precision Cryogenics, Inc. (Indianapolis, IN), and was modified to be reused for ZEUS.

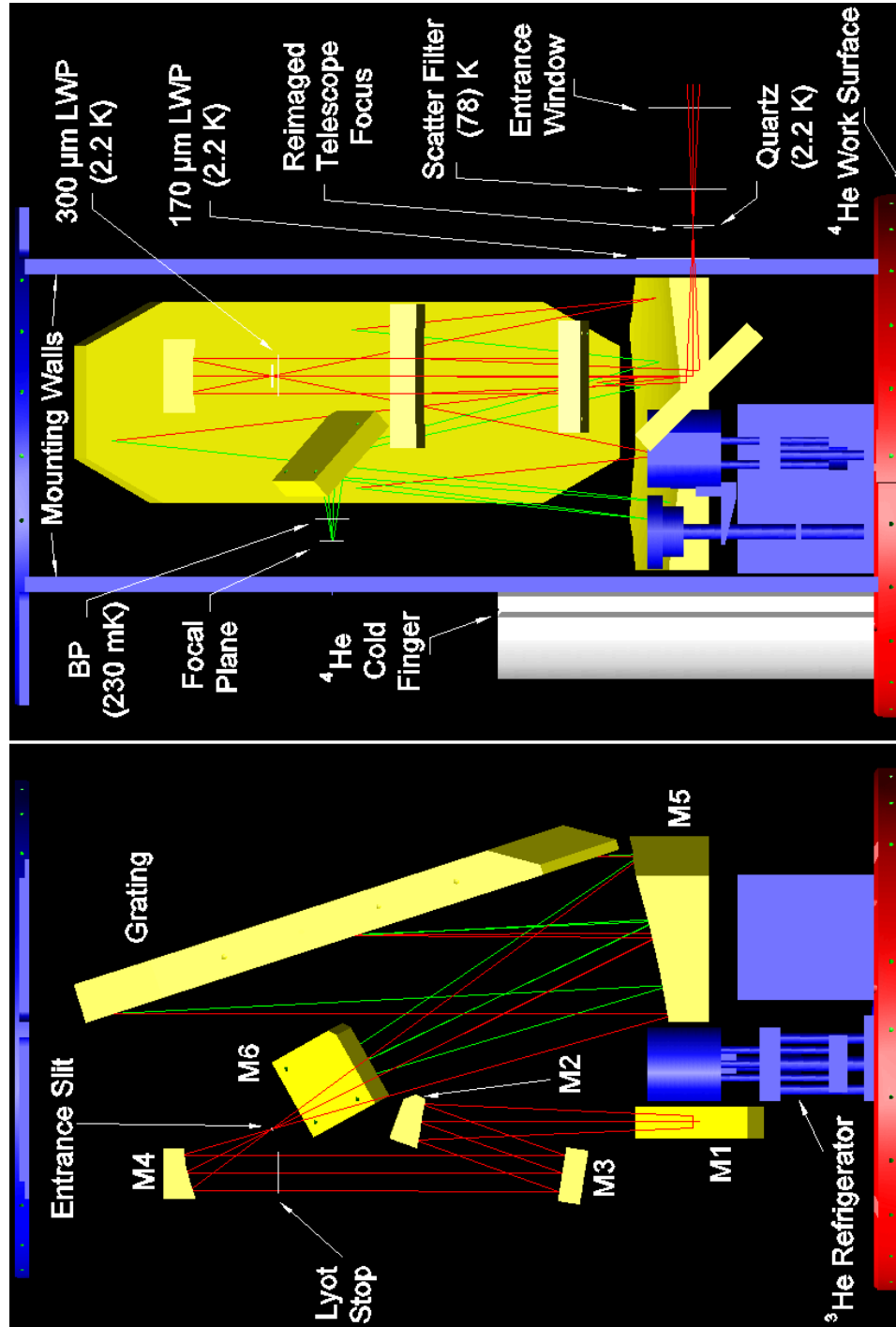


Figure 3.3: ZEUS Optical Layout. *Left*: Front view of the optical layout, with the rays traced from the entrance window to the grating (*red*) and from the grating to the focal plane (*green*). *Right*: Side view, which additionally shows the filters, ^4He cold finger, and the optics mounting walls. Not shown are the pair of baffling boxes which form light-tight enclosures leading from the first optics mounting wall to the Lyot stop, and from the Lyot stop to the entrance slit.

The cylindrical vacuum shell is 92.7 cm tall and 41.3 cm in diameter, and contains nitrogen and helium cryostats suspended from the top plate by a pair of 0.5 mm thick G-10 fiberglass rings (Fig. 3.4). The helium work surface supports a pair of mounting walls which are connected by a strut and a bottom plate to form a rigid structure to which the detector, grating, and 5 of the 6 mirrors are mounted. This structure is made light-tight with additional pieces of thin aluminum, and to ensure that the full spectrometer section is cooled to the helium bath temperature we also add an outer helium-cooled radiation shield. An external stepper motor is connected through the top plate of the vacuum shell to the internal grating drive train by a ferrofluidic feedthrough.

To reduce the conductive heat load on the cryostats both necks are stainless steel, and aside from the G-10 rings the rest of the dewar is aluminum. The nitrogen tank contains 3.4 liters of liquid, which holds for 18 hours. The main helium reservoir holds 5.7 liters, and we added a cold finger that extends down one of the walls and increases this volume to 6.7 liters. After the helium bath is pumped down to 2.2 K the hold time is about 15 hours, and both the nitrogen and helium tanks are filled twice daily.

3.5 ^3He Refrigerator

To obtain the requisite sensitivity we cool the detector package to 230 mK using a dual-stage ^3He refrigerator (Chase Research Cryogenics Ltd., Sheffield, UK), shown schematically in Figure 3.5. Each stage is a closed-cycle system consisting of a cold head, a charcoal adsorption pump with attached heating element, and a gas-gap heat switch linking the pump to the ^4He bath. The cycle begins

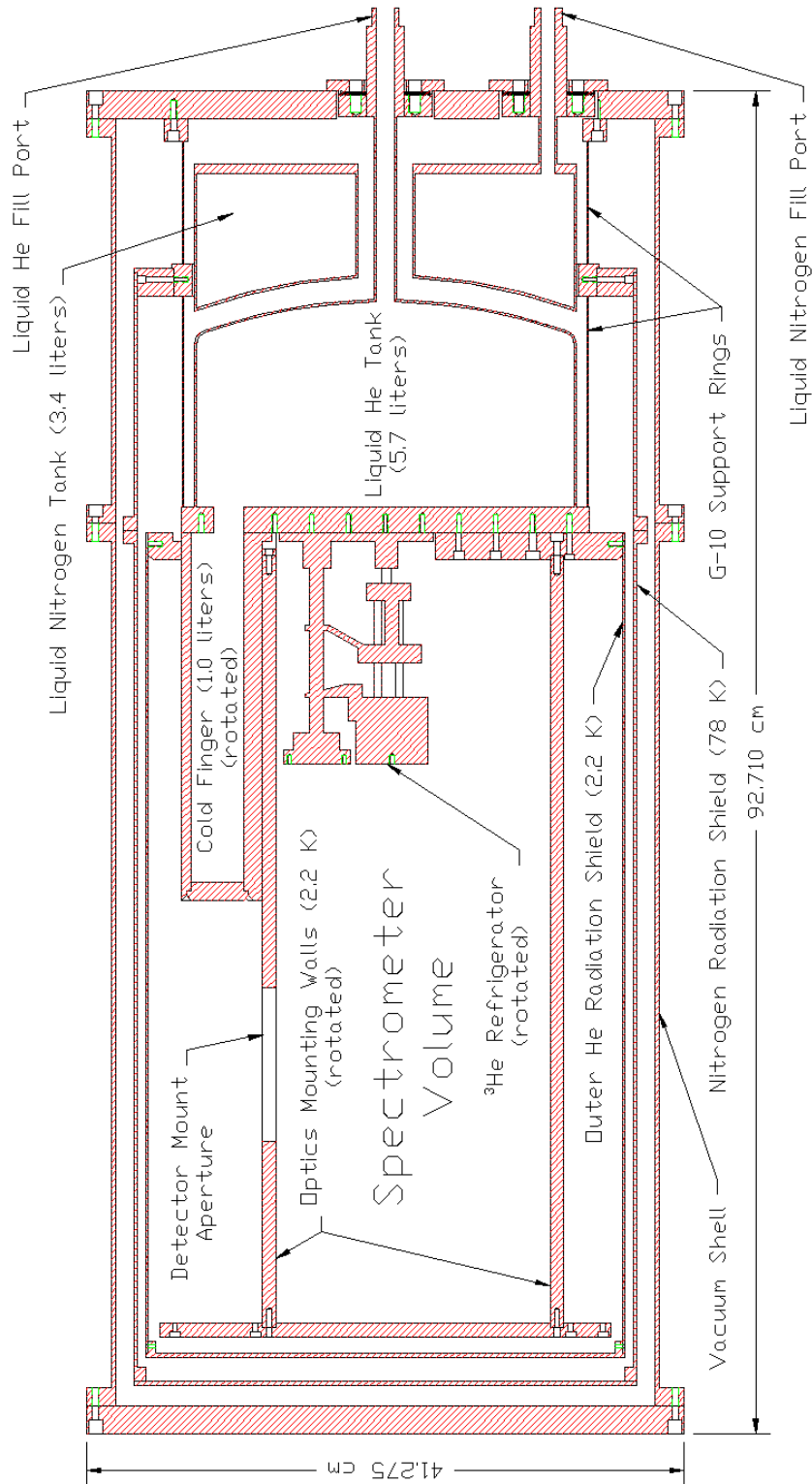


Figure 3.4: Mechanical drawing of the ZEUS cryostat. For clarity, the cold finger, the optics mounting walls, and the ^3He refrigerator are shown rotated by 90° about the central axis.

by isolating the pump and heating it to above 50 K to drive the ^3He gas into the pipe leading to the cold head. A segment of the pipe directly above the cold head is thermally linked to the pumped 2.2 K ^4He bath, and here the ^3He condenses out and drips into the head. The two pumps are heated in series for an hour to allow the ^3He to condense and cool the otherwise isolated cold heads, as well as the attached detector package. The heat switches are then closed to cool the charcoal, which then adsorbs the evaporated ^3He and lowers the vapor pressure over the liquid, allowing it to cool to 300 mK and below.

The intermediate stage uses a heat exchanger to extract enthalpy from the cold gas and cool the pipes leading to the cold head, thereby reducing the heat load conducted from the ^4He bath. The residual heat load limits the operating temperature of the intermediate cold head to 300 mK. The heat exchanger and intermediate head are coupled to the gas pipe leading to the ultracold head, absorbing the conductive load and allowing the ultracold head to cool to 225 mK. The detector package is suspended from one of the ^4He mounting walls by a thermally-isolating system of Kevlar cord. The suspension system consists of 12 segments of 0.25 mm diameter and 18 mm long cord, giving a total cross-section to length ratio of 0.033 mm. The integrated thermal conductivity of Kevlar from 2.2 K down to 230 mK is $10 \mu\text{W mm}^{-1}$ [122], giving a total heat load of $0.33 \mu\text{W}$. The detector package is coupled to the ultracold head by an 18 cm long copper heat strap, and the power conducted through the Kevlar mount raises the detector package temperature to 230 mK.

The ultracold head, the detector housing, and the cold section of the Kevlar suspension mount contribute about 350 grams of copper which must be cooled from 2.2 K to 225/230 mK. The specific heat of copper at low temperatures is

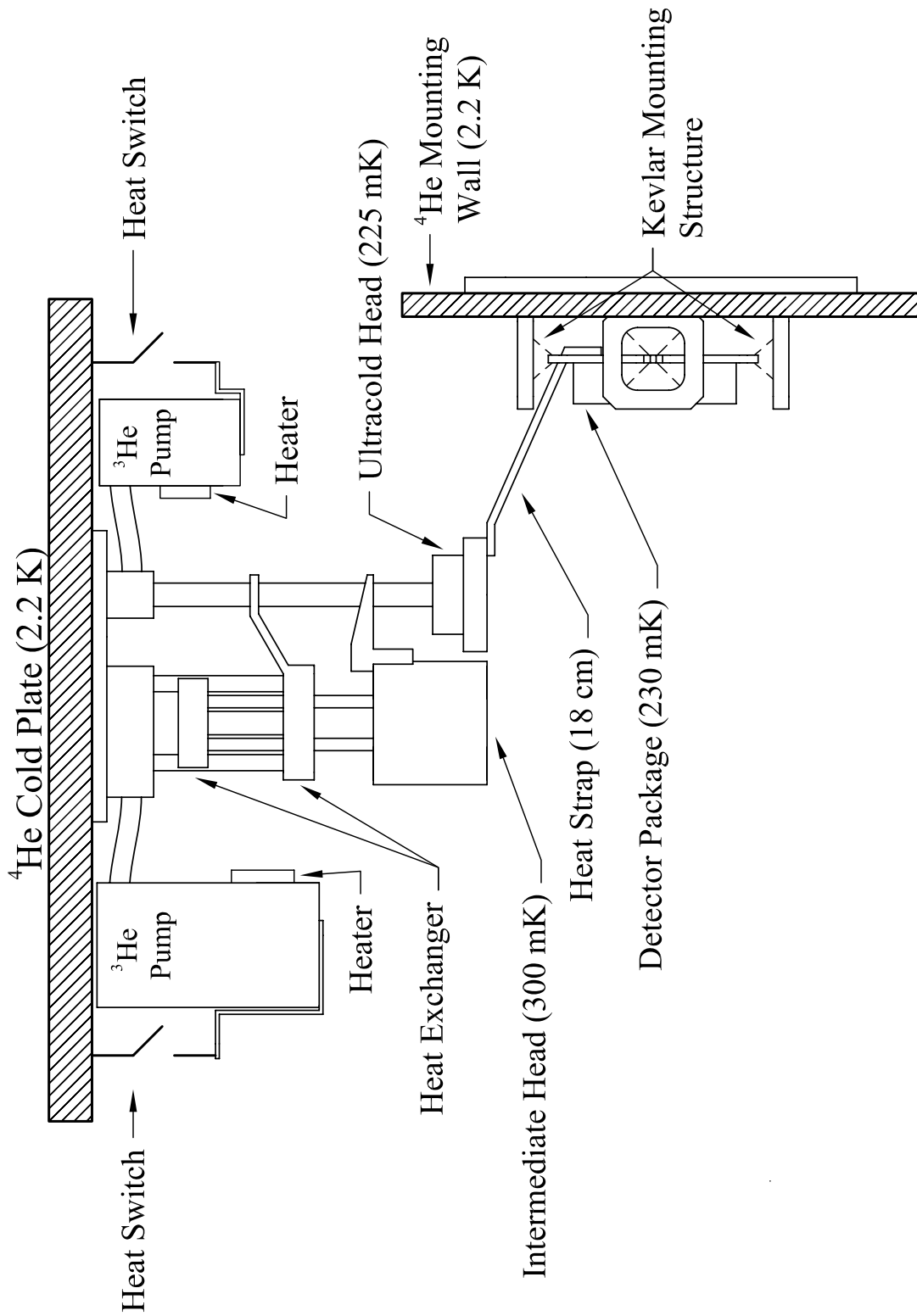


Figure 3.5: Simplified sketch of the (unfolded) ^3He refrigerator, also showing the Kevlar suspension mount used to thermally isolate the detector package.

$C(T) = 11(T/K) + 1.0(T/K)^3$ mJ kg⁻¹ K⁻¹, and integrating from 2.2 K down to 225 mK requires 32 mJ kg⁻¹, or 11 mJ total. This will evaporate about 0.00027 moles of ³He, much less than the 0.13 moles contained in the ultracold stage. The detector reaches 260 mK about 2 hours after the start of the cycle, and approaches the 230 mK operating temperature over the next 2 – 3 hours.

The system hold time is limited by the capacity of the intermediate stage, which absorbs the power conducted from the ⁴He bath. Manufacturer testing indicates that $\approx 67\%$ of the 0.54 moles of ³He contained in the intermediate stage is liquified and cooled to 300 mK in a successful cycle. For a latent heat of evaporation of 27 Joules per mole, this corresponds to a cooling capacity of 9.6 Joules. When run from an unpumped 4.2 K ⁴He bath, the parasitic heat load conducted through the gas pipes to the intermediate head is ≈ 50 μ W. We also run 78 manganin signal and thermometry wires to the detector which are sunk to both the heat exchanger and the intermediate head, and which add a small additional heat load to the intermediate head. The diameters of these wires range from 0.102 – 0.127 mm and the distance from the heat exchanger to the intermediate head is 35 mm, giving a total cross-section to length ratio of 0.019 mm. The integrated thermal conductivity of manganin from the 1.3 K temperature of the heat exchanger to the 0.3 K temperature of the intermediate head is 0.062 W m⁻¹, so the total additional heat load conducted through the wires is only 1.2 μ W. Under a 50 μ W total heat load the 9.6 Joule cooling capacity should provide a 52 hour run time, somewhat longer than the 36 hours we achieve. While additional heat sources cannot be ruled out, it is more likely that our routine for cycling the refrigerator condenses and cools only $\approx 50\%$ of the total ³He mass in the intermediate stage.

When operating from a pumped 2.2 K ^4He bath, the conductive load on the intermediate head is reduced and the hold time increases to more than 60 hours. Under normal operation at the telescope the ^4He bath is continuously pumped to 2.2 K and the ^3He refrigerator is cycled every 2 days.

3.6 Filtration

As bolometers are sensitive to all wavelengths of light, it is important to reject stray and out of band radiation, particularly the short wavelength radiation ($\lambda \lesssim 100 \mu\text{m}$) emitted by sources at 78 – 300 K. We describe the filtration and baffling working inward from the entrance window (see Fig. 3.3). A snout on the nitrogen-cooled radiation shield blocks light incident from large angles, and a 78 K scatter filter placed over the shield aperture scatters short wavelength radiation ($\lambda \lesssim 100 \mu\text{m}$) out of the beam. The light must then pass through a quartz filter mounted on the outer helium radiation shield near the reimaged telescope focus, which reflects or absorbs radiation between $5 \mu\text{m} < \lambda < 45 \mu\text{m}$. Behind the quartz a long wavelength pass (LWP) ($\lambda \gtrsim 170 \mu\text{m}$) filter blocks the aperture in the optics mounting wall. Light passing through this filter enters a light-tight baffling box which allows radiation to escape only through the Lyot stop, where there is a second LWP ($\lambda \geq 300 \mu\text{m}$) filter. A second baffling box then connects the Lyot stop to the entrance slit. A bandpass (BP) filter with a fractional width of $\lambda/\Delta\lambda \approx 8$ is mounted directly in front of the bolometers on the 230 mK detector package, and selects the grating diffraction order. Both our LWP and BP filters were constructed by P. A. R. Ade and C. E. Tucker at Cardiff University, Cardiff, UK. The elements in the ZEUS optical train are listed in Table 3.2.

Table 3.2: Elements in the ZEUS Optical Train

Component	T [K]	Filtration	Transmission	
			330 – 380 μm	420 – 480 μm
Polyethylene Window	280	–	0.96	0.96
Scatter Filter	78	$\lambda \gtrsim 100 \mu\text{m}$	0.80 – 0.94	0.84 – 0.88
Quartz	2.2	$\lambda \gtrsim 45 \mu\text{m}$	0.90	0.90
170 μm LWP Filter	2.2	$\lambda \gtrsim 170 \mu\text{m}$	0.88 – 0.92	0.87 – 0.98
Mirror ($\times 7$)	2.2	–	0.98 ⁷	0.98 ⁷
300 μm LWP Filter	2.2	$\lambda \gtrsim 300 \mu\text{m}$	0.74 – 0.85	0.87 – 0.92
Grating	2.2	$\lambda/\Delta\lambda \sim 1000$	0.49 – 0.74	0.45 – 0.72
BP Filter	0.230	$\lambda/\Delta\lambda \approx 8$	0.15 – 0.75	0.21 – 0.93
Total			0.04 – 0.22	0.08 – 0.34

Note. – At the centers of the 350 and 450 μm bands the peak system transmission is 0.22 and 0.34, respectively. This drops at the edges of the windows due to a decreased transmission of the BP filters.

In the current configuration, two bandpass filters are placed adjacently over the array, such that the system simultaneously obtains spectra in both the 350 and 450 μm telluric windows. The grating and filters ensure that the detector array sees spectrally pure radiation from the astronomical source, and unavoidable background radiation from the sky and telescope. This background power amounts to ~ 1 pW, which is ~ 130 times less power than emitted by a cm^2 blackbody at 2.2 K, and this illustrates the challenge in baffling/filtering unwanted radiation from the detectors. With the final BP filter tied to the 230 mK detector package we minimize the radiative load generated by the 2.2 K pumped ^4He bath.

CHAPTER 4

DETECTORS AND ELECTRONICS

In the previous chapter we described how radiation is directed from the telescope through the spectrometer to the focal plane. In this chapter we describe how the power is detected by the bolometer array, and how the signal is read out by subsequent electronics. We then characterize the detectors, estimate the optical transmission of the full system, and estimate the system sensitivity.

4.1 Introduction

When ZEUS was constructed, the most sensitive detectors available for direct-detection submillimeter astronomy were semiconductor bolometers. A bolometer is a device that thermalizes absorbed photons, such that the bolometer's temperature is a measure of the incident optical power. A detector consists of a thermally coupled thermistor and absorber at temperature T connected by a weak thermal link to a heat sink at temperature T_0 . The power conducted through the thermal link is $W = G_s(T, T_0)(T - T_0)$, where $G_s(T, T_0)$ is the static thermal conductance. The thermistor has a temperature-dependent electrical impedance $R(T)$ and is biased in series with a load resistor with $R_L \gg R$, such that the thermistor is approximately current-biased. Small changes in the absorbed optical power translate to small changes in the electrical impedance, and the resulting change in the output voltage is measured as the signal. In addition to the quantum efficiency η_{dqe} of the absorber and the temperature T_0 of the heat sink, the detector is characterized by the functions $R(T)$ and $G_s(T, T_0)$.

4.2 Implementation

The 1×32 ZEUS bolometer array was fabricated by S. H. Moseley and collaborators at NASA Goddard Space Flight Center, Greenbelt, MD, and is similar to one of the 32-element rows developed for use in the SHARC II and HAWC cameras [84, 19, 123]. Each of the thermistors is formed on a $1 \mu\text{m}$ thick, $1 \text{ mm} \times 1 \text{ mm}$ silicon membrane by ion-implanting the front face with phosphorous and boron. Conduction in the thermistor is via variable range hopping within the valence band, and the impedance has the form $R(T) = R^* \exp\left(\sqrt{T_g/T}\right)$. The membrane is attached to a thick silicon frame with legs extending in two opposite directions, allowing the 32 bolometers to be closely packed in the orthogonal direction. The silicon frame serves as the heat sink, and the thermal link provided by the legs is modeled to have a static thermal conductance $G_s(T, T_0) = g_s (T^{\beta+1} - T_0^{\beta+1}) / (T - T_0)$. Two edges of the bolometer and the legs are degenerately doped to form an electrical contact between the thermistor and traces on the frame, which terminate in a series of wire bond pads. The back face of each detector is metalized with a chromium gold film with an impedance of $155 \Omega/\text{square}$, and the detector is mounted 0.4 mm from a metalized backshort. This provides an absorption efficiency of $\approx 0.58 - 0.82$ over most of the 350 and $450 \mu\text{m}$ telluric windows.

The silicon detector frame and the G-10 fiberglass circuit board containing the load resistors are mounted together in the copper detector house. The circuit board contains 32 metal film chip resistors with temperature-independent impedances of $50 \text{ M}\Omega$. The bond pads on the detector frame are wire bonded to the circuit board traces, which are in turn wire bonded to the load resistors. Twisted pairs of copper wire carry the signal from the board to a pair of 37 pin

micro-D connectors mounted to the side wall of the detector house. The order-sorting bandpass filters are fixed directly to the front face of the house, with half of the array covered by the 350 μm bandpass filter and the other half by the 450 μm filter. The entire package is held at 230 mK.

The detector package is suspended from the ^4He mounting wall by a Kevlar support structure (see Fig. 3.5). An aluminum baseplate bolted to the wall supports 3 aluminum towers, each of which is 5 cm tall and contains a 2.5 cm \times 2.5 cm aperture. A pair of Kevlar cords are strung diagonally across the aperture to form a cross. At the point of intersection the cords are epoxied to a tab protruding from the side of a copper plate, such that the plate is fixed at three points, and is thermally isolated from the aluminum towers. The detector package is bolted to this plate, and connected to the ^3He refrigerator by a copper heat strap.

4.3 Electronics and Software

A schematic of the readout electronics is shown in Figure 4.1. As the signal produced by the detectors has a high source impedance, it is subject to microphonic pickup and electrical interference, and the first step is to buffer it with a JFET source follower. The 32 JFETs are mounted on 2 boards and attached to the nitrogen tank, loosely linked such that they self-heat to 250 K. The signal is taken from the detector package to the JFET boards with twisted pairs of 38 AWG manganin wire woven into a ribbon cable, and epoxied into micro-D connectors. To reduce any microphonic pickup the cables are tensioned and fastened to the cryostat when possible. To minimize the conductive heat loading the cables are well sunk to the ^4He work surface, the ^3He refrigerator heat

exchanger, and the intermediate cold head on their path from the JFETs to the detector package.

The signal is then taken through stainless steel coaxial cables to the warm preamplifier circuit, housed in a box mounted directly to the dewar. Here the signal is sent through a high-pass filter ($f_0 = 0.16$ Hz) before amplification by a factor of 100 by a low-noise operational amplifier, and subsequently amplified by a factor of 1 – 1000 by a programmable gain chip. The output is then carried by twisted pair cables to two 16-channel, 16-bit IOtech DBK80 A/D boards, driven by an IOtech DaqLab/2001 data acquisition device. The chopper reference is also digitized here, and the output is sent to the instrument PC by a dedicated Ethernet cable. A custom Labview program communicates with the telescope computer to control the chopping and nodding, and co-adds the data stream using a lockin routine with the chopper signal as reference. To minimize electronic interference the bias is provided by a battery inside the preamplifier box, and the preamplifier circuits and the JFET drain supply are powered by batteries housed in a shielded box. The DaqLab is connected to the building power by an isolation transformer, and the dewar is connected to earth ground.

4.4 Bolometer Characterization

In this section we describe our use of load curve measurements to fully characterize the bolometers. We begin by obtaining estimates of the four parameters describing the intrinsic thermal and electrical properties of each bolometer, and then use these results to estimate the optical loading and the responsivity. The load curve analysis used in this section follows the work of [114, 127].

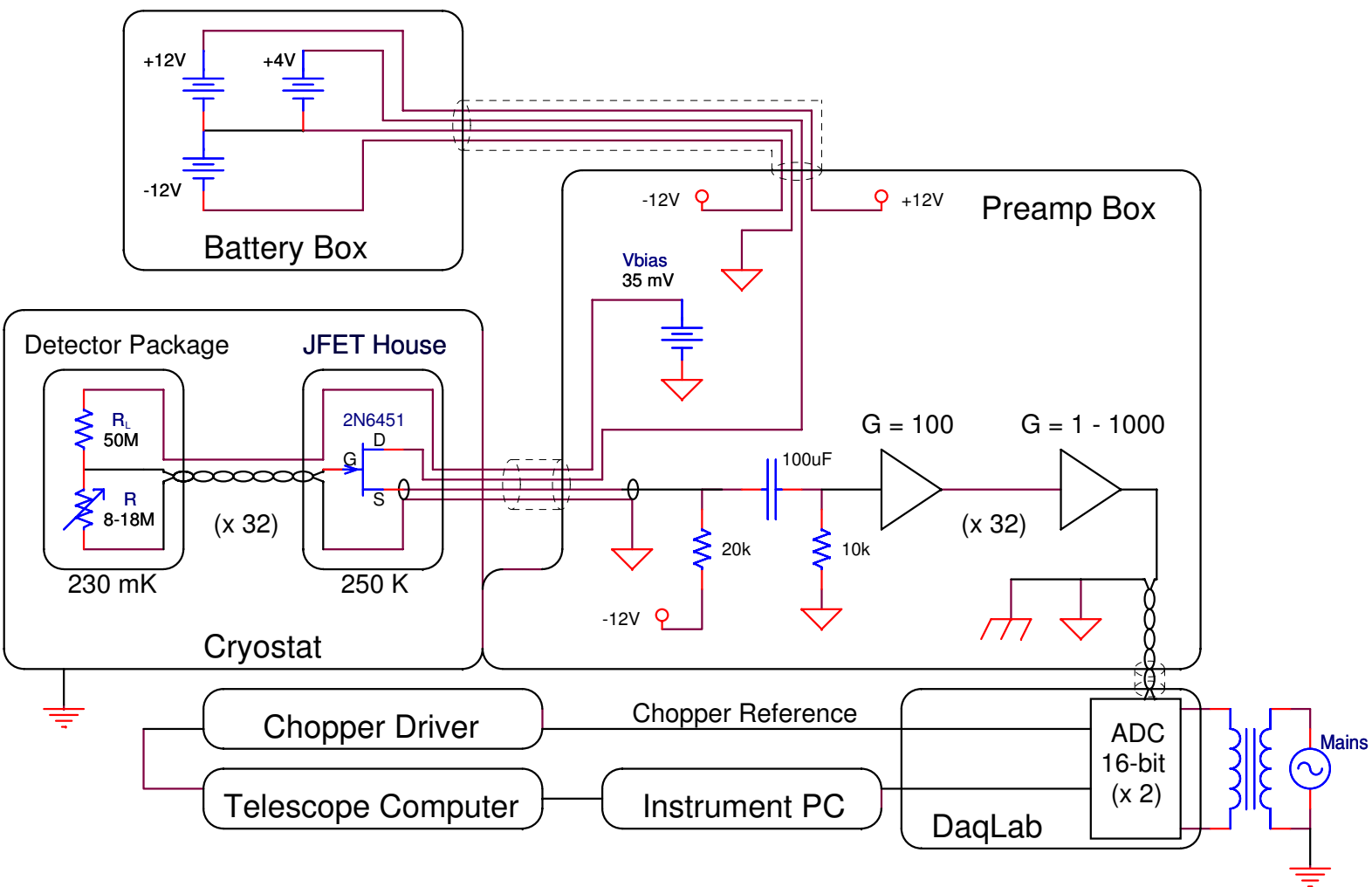


Figure 4.1: Sketch of the ZEUS electrical layout, illustrating the biasing, readout, amplification, and digitization.

4.4.1 Dark Load Curves

For a bolometer in thermal equilibrium, the sum of the absorbed optical power and dissipated electrical power is balanced by the cooling flow through the thermal link. This balance is expressed by the equation

$$P + Q = g_s (T^{\beta+1} - T_0^{\beta+1}), \quad (4.1)$$

where P is the electrical power, Q is the optical power, T is the bolometer temperature, T_0 is the sink temperature, and g_s and β are properties of the thermal link. The electrical impedance of the bolometer is given as

$$R(T) = R^* \exp\left(\sqrt{T_g/T}\right), \quad (4.2)$$

where R^* and T_g are material properties of the thermistor. The first step in our analysis is to measure g_s , β , R^* , and T_g for our bolometers. This is accomplished by taking dark load curves.

A bolometer is probed by measuring its current-voltage relation, otherwise known as its $I - V$ curve or load curve. We begin by obtaining load curves with the detector package sealed off, such that the bolometers are exposed to a T_0 radiation field and absorb a negligible amount of optical power. We take a series of 6 such load curves with different values of the sink temperature T_0 . For each curve we extrapolate the impedance down to the limit of no electrical power, where with $P = Q = 0$ the bolometer is expected to be at the sink temperature $T = T_0$. In this manner we build up a set of points $R_0(T_0) = R(T = T_0)$ which samples the $R(T)$ curve defined in equation 4.2, and allows us to estimate R^* and T_g .

With $Q = 0$, equations 4.1 and 4.2 can be combined to form

$$P(R) = X \left[\left(\frac{T_g/T_0}{[\ln(R/R^*)]^2} \right)^Y - 1 \right], \quad (4.3)$$

where $X = g_s T_0^{\beta+1}$ and $Y = \beta + 1$. Armed with our estimates of R^* and T_g , a single load curve can be fit for the two free parameters X and Y , giving estimates of g_s and β . In principle any load curve associated with a particular T_0 can be used for this fit, but we choose to use the load curve taken with the coldest $T_0 = 225$ mK, as this is very close to the sink temperature in normal operation. In Figure 4.2 we show a sample set of dark load curves analyzed with this method.

This process is repeated for each bolometer, and in Table 4.1 we list the measured ranges of T_g , R^* , g_s , and β . With these parameters we have a complete thermal model, which can be used to predict the performance of each bolometer.

4.4.2 Unblanked Load Curves

The next step in our analysis is to estimate the total absorbed optical power Q , and the change in absorbed optical power ΔQ resulting from a change in the external radiation field. We begin by taking a pair of load curves with the spectrometer first exposed to an ambient temperature ($T = 280$ K) radiation field, and then with the instrument entrance window filled with a cold ($T = 78$ K) load. A sample pair of such load curves is shown in Figure 4.3, along with a theoretical $Q = 0$ load curve created from the thermal model. The bolometer temperature, and therefore its electrical impedance, depends only on the sum $P + Q$. Therefore if we change the optical loading by an unknown amount ΔQ and adjust the electrical power by a known amount ΔP such that the electrical

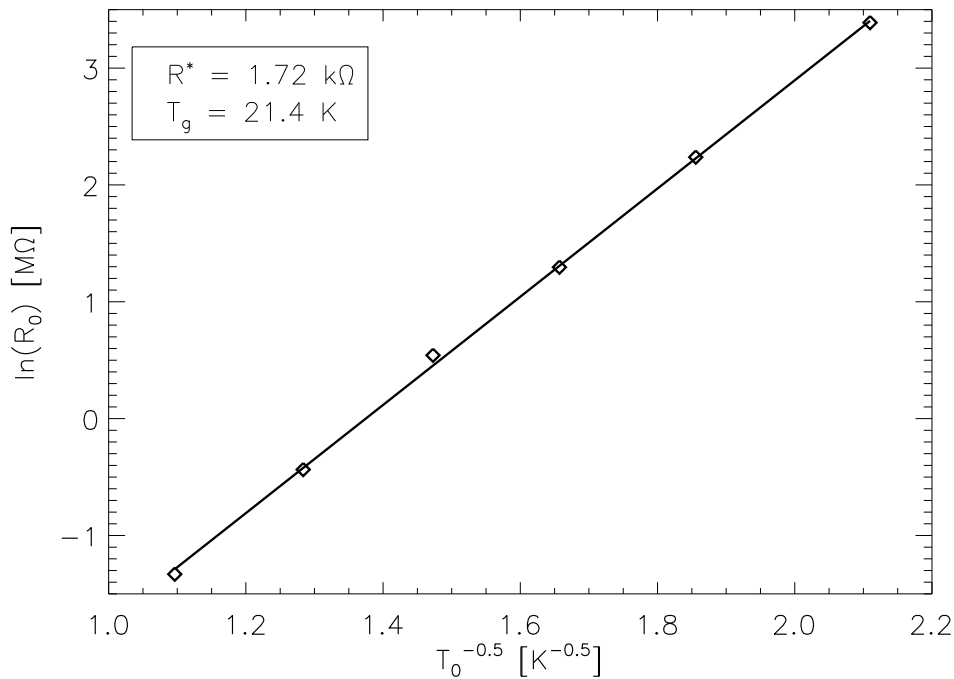
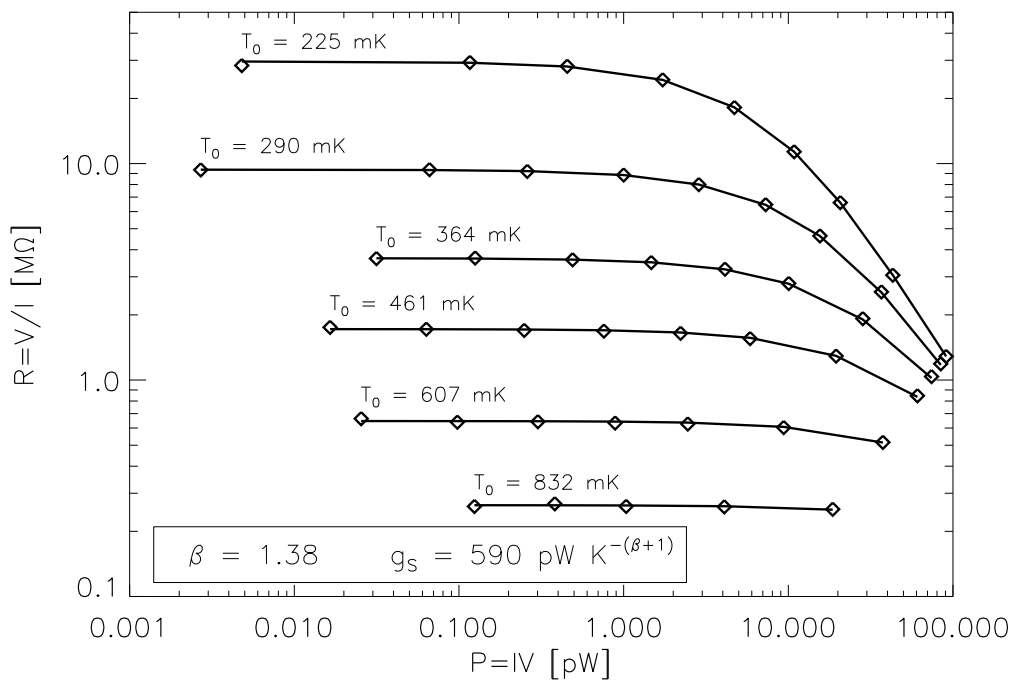


Figure 4.2: Dark Load Curves. *Top*: Series of dark load curves taken with varying sink temperature T_0 . A fit to the $T_0 = 225$ mK curve with the values of R^* and T_g obtained from the bottom plot are used to derive β and g_s , and these parameters are used to overlay models for the other 5 curves. *Bottom*: Plot of the zero-bias impedance R_0 vs. T_0 , used to obtain estimates of R^* and T_g .

Table 4.1: ZEUS Bolometer Parameters

Parameter	Symbol	450 μm half (1 – 16)	350 μm half (17 – 32)	Units
Quantum Efficiency	η_{dqe}	0.58 – 0.76	0.68 – 0.82	
Sink Temperature	T_0	230	230	mK
$W(T, T_0) = g_s (T^{\beta+1} - T_0^{\beta+1})$	β	1.23 – 1.46	1.42 – 1.58	
	g_s	420 – 670	536 – 864	pW/K $^{\beta+1}$
$R(T) = R^* \exp(\sqrt{T_g/T})$	R^*	1.44 – 2.80	1.17 – 1.67	k Ω
	T_g	19.2 – 22.5	19.1 – 23.3	K
Operating Impedance	R	9.6 – 15.1	8.0 – 17.7	M Ω
Operating Temperature	T	260 – 280	250 – 270	mK
Dynamic Thermal Conductance	G_d	186 – 254	166 – 273	pW/K
Optical Loading	Q^a	4.2 – 4.7	2.8 – 3.9	pW
Electrical Responsivity	S_E	2.6 – 4.5	2.6 – 4.8	10 8 V/W
Photon Noise	NEP_{photon}^b	2.0 – 3.5	3.3 – 4.4	10 $^{-17}$ W/ $\sqrt{\text{Hz}}$
	NEV_{photon}	5.9 – 15.3	9.5 – 21.3	nV/ $\sqrt{\text{Hz}}$
Johnson Noise	NEV_{Johnson}	8.8 – 9.6	7.9 – 9.8	nV/ $\sqrt{\text{Hz}}$
Thermal Noise	NEP_{thermal}^b	2.4 – 2.8	2.2 – 2.8	10 $^{-17}$ W/ $\sqrt{\text{Hz}}$
	NEV_{thermal}	7.3 – 10.8	6.9 – 12.3	nV/ $\sqrt{\text{Hz}}$
Thermistor 1/f Noise at 2 Hz	$NEV_{1/f}$	3.5 – 6.5	3.2 – 8.4	nV/ $\sqrt{\text{Hz}}$
Electrical Noise	$NEV_{\text{FET+Amp}}$	≈ 14	≈ 14	nV/ $\sqrt{\text{Hz}}$
Total Noise	NEV_{total}	$\approx 20 - 26$	$\approx 20 - 31$	nV/ $\sqrt{\text{Hz}}$
Measured Noise	NEV_{measured}^c	28	28	nV/ $\sqrt{\text{Hz}}$

^aAveraged over each half of the array.

^bRefers to detected (rather than incident) power.

^cMeasured at the centers of the telluric windows during the March 2008 observing run. In subsequent runs in December 2008 and March 2009 the electrical noise was reduced and the responsivity increased, thereby bringing the system noise closer to the background photon limit.

Table 4.1 (Continued)

Note. – Detectors 1 – 16 operate in the $450\ \mu\text{m}$ band, and detectors 17 – 32 operate in the $350\ \mu\text{m}$ band. Unless otherwise noted, the ranges specified for each parameter include variations both with detector and with operating wavelength in the $\lambda \approx 430 - 470\ \mu\text{m}$ and $\lambda \approx 340 - 370\ \mu\text{m}$ regions in which the bandpass filters are highly transmissive. The parameters η_{dqe} and NEP_{photon} are assumed to be detector-independent, and are calculated over the same spectral bands. The ranges specified for β , g_s , R^* , and T_g refer to variations with detector.

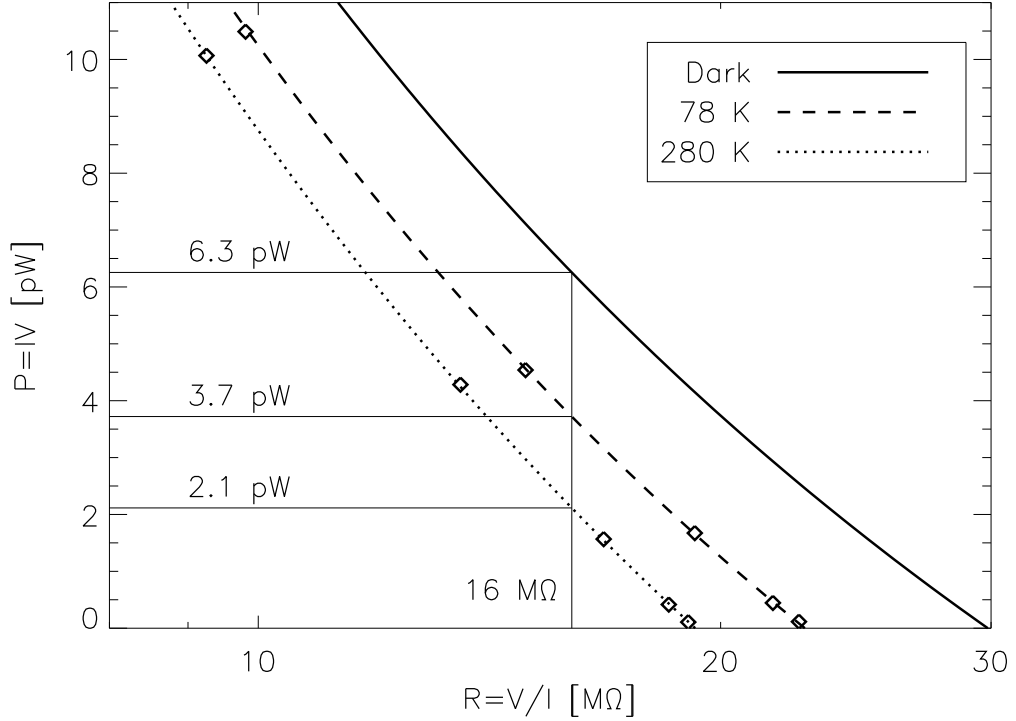


Figure 4.3: Pair of unblanked load curves with different optical loading, along with simple model fits used to interpolate between data points. Also shown is a theoretical load curve calculated for no optical loading. Differencing any two curves gives the differential loading ΔQ between the two configurations.

impedance is unchanged, we have $\Delta P = -\Delta Q$. Differencing any pair of curves in Figure 4.3 at fixed R therefore gives the change in optical loading between the two configurations.

As an example, it takes 2.1, 3.7, and 6.3 pW of electrical power to fix the bolometer at $R = 16 \text{ M}\Omega$ when exposed to a 280 K external load, a 78 K external load, and when blanked off, respectively. This implies that when the temperature of the external radiation field increases from 78 K to 280 K the optical load increases by $\Delta Q = 3.7 - 2.1 = 1.6 \text{ pW}$, and the total optical loading under normal operation is $Q = 6.3 - 2.1 = 4.2 \text{ pW}$. This estimate of Q is included in Table 4.1.

An important characteristic of a bolometer is the electrical responsivity S_E ,

defined as the change in output voltage with respect to a small change in the optical loading ($S_E = dV/dQ$). The responsivity can be determined from the shape of a single load curve by [80]

$$S_E = \frac{-1}{2I} \left(1 - \frac{Z}{R}\right) \frac{R_L}{Z + R_L}, \quad (4.4)$$

where the dynamic impedance is $Z = dV/dI$. Estimates of S_E derived in this manner from the 280 K load curves are included in Table 4.1, and typical values are $S_E \approx 3.6 \times 10^8$ V/W.

A second estimate of S_E may be obtained by fixing the bias voltage and measuring the change in output voltage ΔV resulting from a change in the external radiation field. Dividing this by the corresponding estimate of ΔQ obtained above allows us to compute $S_E \approx \Delta V/\Delta Q$. We note that changing the external radiation temperature by the large value of ≈ 200 K will change the operating condition of the bolometer in a way that changing the radiation temperature by a small amount (as when chopping between a source and blank sky during normal operation) won't. This 'large-signal' responsivity may therefore be somewhat different than the 'small-signal' responsivity estimated from the shape of the load curve. The two methods generally agree to within 10%, however, so we consider this latter estimate as supporting the accuracy of the first method.

The bolometer operating temperature T is derived from the measured resistance and equation 4.2. We are then able to calculate the dynamic conductance of the thermal link, defined as $G_d(T) = dW/dT = g_s(\beta + 1)T^\beta$. The estimates of R , T , and G_d are included in Table 4.1, and are used in section 4.6.2 to estimate the noise produced by the bolometers.

4.5 System Transmission

An estimate of the optical transmission of the full system may be obtained from the load curve analysis presented in section 4.4.2. When the temperature of the external radiation field is increased from 78 K to 280 K, the resulting increase in the power absorbed by a detector is given as

$$\Delta Q = \frac{\lambda^2 [B_\nu(280K) - B_\nu(78K)]}{2} m \Delta \nu \eta_{\text{sys}}, \quad (4.5)$$

where $B_\nu(T)$ is the Planck function, the number of spatial and polarization modes sampled is $m = 2A\Omega/\lambda^2$, $\Delta \nu$ is the bandwidth collected by the detector, and η_{sys} is the optical transmission of the full system, including the dewar entrance window, the cold optical elements, and the detector quantum efficiency. The solid angle Ω of the external radiation field seen by the detectors is limited by the cold Lyot stop such that $m = 2 \times (455 \mu\text{m}/\lambda)^2$, and the linear dispersion of the spectrometer determines $\Delta \nu \approx \nu/1500$. Estimates of ΔQ obtained from load curves taken with the grating at two different settings were combined with equation 4.5 to estimate the transmission at $\lambda = 340 \mu\text{m}$, $371 \mu\text{m}$, $432 \mu\text{m}$, and $468 \mu\text{m}$, and the derived values of η_{sys} from a pair of representative detectors are shown in Figure 4.4.

A second method of estimating the system transmission is to chop between the two external loads in a simulated observation, and examine the recorded AC signal. The power difference ΔQ is then obtained by dividing this voltage by the detector responsivity (S_E) and the post-detection amplification (G), and η_{sys} is then calculated using equation 4.5. As this calculation involves an accurate knowledge of the $(G \times S_E)$ product it is inherently less reliable than the first method. However, measurements of the AC voltage response are available over

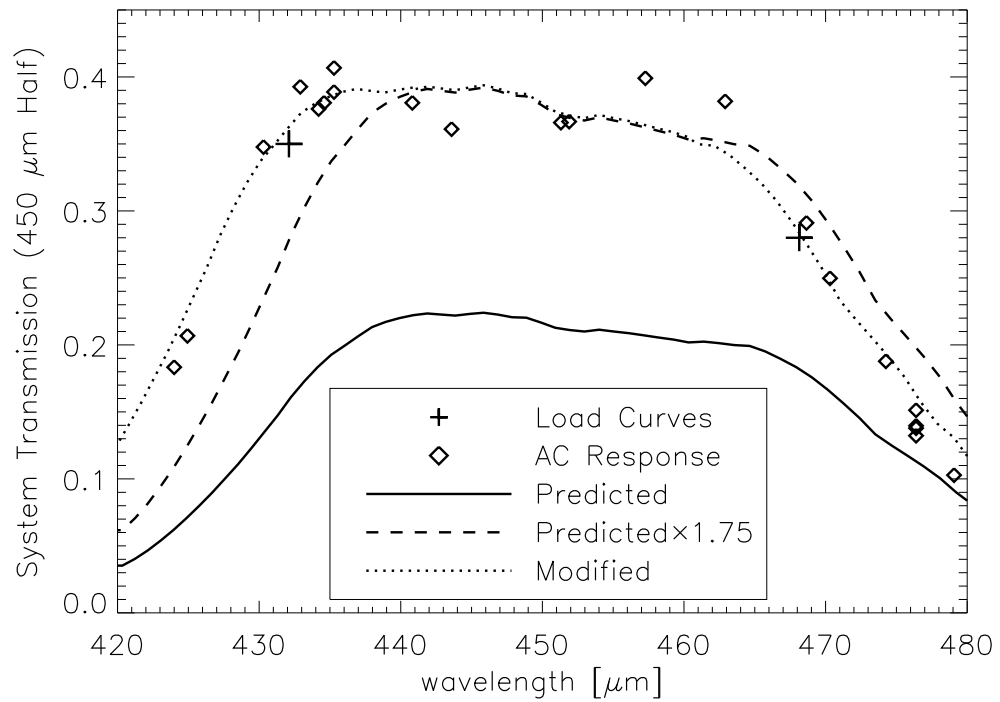
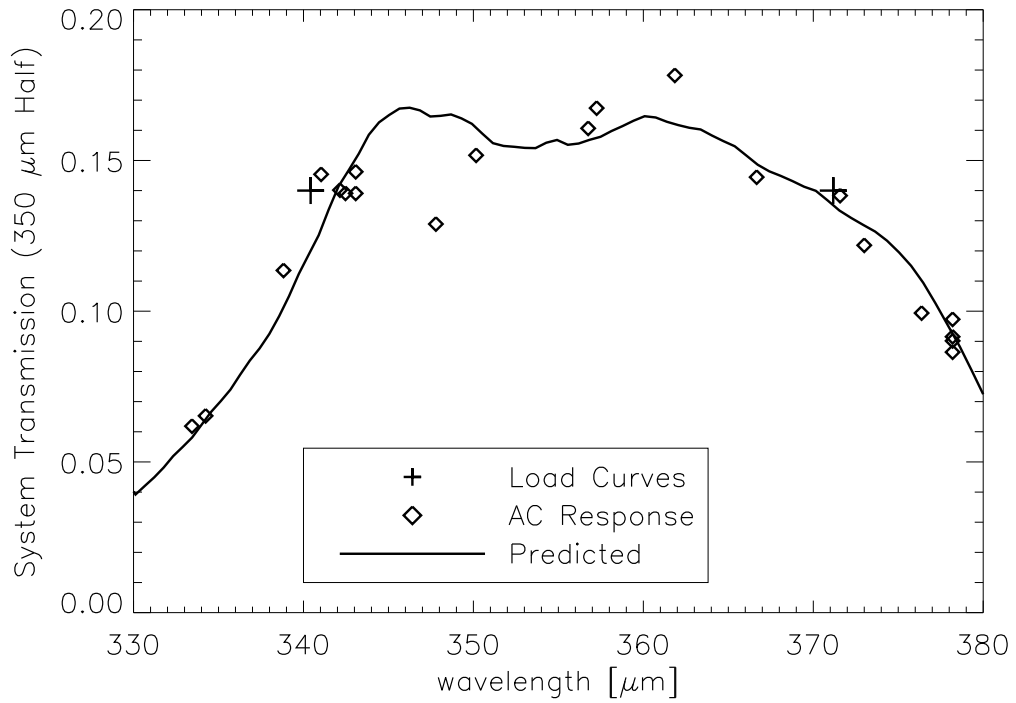


Figure 4.4: Full System Optical Transmission. *Top*: Estimates of η_{sys} obtained from load curves (*crosses*) and AC response measurements (*diamonds*), along with a curve showing the predicted transmission (*solid*). *Bottom*: Same as the top, with additional curves showing a scaled ($\times 1.75$) model (*dashed*) and a scaled and shifted model (*dotted*).

the full spectral range, so we use this data to complement the pair of load curve measurements. These resulting values of η_{sys} are also included in Figure 4.4.

An examination of Figure 4.4 shows that the two methods of estimating η_{sys} are in good agreement. We create a model of η_{sys} by multiplying the estimated transmission of the dewar entrance window and cold optical elements (discussed in section 3.6) with the detector quantum efficiency, and include this model in Figure 4.4. We find good agreement between the data and the model in the 350 μm band, but in the 450 μm band the measured transmission is higher than predicted. The measurements at the center of the band require the transmission model to be scaled by ≈ 1.75 , and the data points at the edge of the window additionally require the corners of the bandpass filter to be shifted to shorter wavelengths. The modified scaled and shifted model profile is shown as the dotted line in Figure 4.4.

At present we are unable to explain this excess power, but suggest that it arises from an underestimate of the transmission of one or more of the optical elements and/or of the detector quantum efficiency. It is also possible that the error lies in our estimate of the $(m\Delta\nu)$ product rather than in η_{sys} . However, as the factors that determine this product (Ω is defined by the Lyot stop and $\Delta\nu$ by the grating dispersion) are common to both halves of the array, we consider it unlikely that our model for estimating $(m\Delta\nu)$ succeeds on the 350 μm half but not on the 450 μm half. The resolution of this discrepancy is the subject of ongoing investigation.

4.6 Noise Contributions

In this section we estimate the noise produced by fluctuations in the background radiation field, noise produced by the detectors themselves, and noise added to the system by the readout electronics, and compare the modeled full system noise with measurements.

4.6.1 Photon Noise

The fundamental limit to the sensitivity of a direct-detection spectrometer is set by fluctuations in the photon arrival rate. For a detector exposed to a thermal source with temperature T and emissivity ϵ , the variance in detected power is [4]

$$\sigma_P^2 = \frac{(h\nu)^2}{t_{\text{int}}} \left[m\Delta\nu\epsilon\tau\eta_{\text{dqe}}n \left(1 + \epsilon\tau\eta_{\text{dqe}}n \right) \right], \quad (4.6)$$

where the total integration time is t_{int} , the power is detected over a narrow bandwidth $\Delta\nu$, the cold optics have transmission τ , the detector quantum efficiency is η_{dqe} , and the mode occupation number is $n = (\exp(h\nu/kT) - 1)^{-1}$. In general the power from each source coupling to the detector must be considered separately, but in our case the noise power is dominated by emission from the warm optics, telescope, and atmosphere, which we describe with a single emissivity and $T = 265$ K.

The noise is traditionally expressed in terms of the noise equivalent power (NEP), which is defined as the signal power giving a signal to noise ratio of 1, divided by the square root of the electrical bandwidth Δf . For a direct integration

of time t_{int} we have $\Delta f = 1/(2t_{\text{int}})$ [95], so

$$\begin{aligned} NEP_{\text{photon}} &= \sqrt{2t_{\text{int}}\sigma_P} \\ &= (h\nu) \sqrt{2m\Delta\nu\epsilon\tau\eta_{\text{dqe}}n(1 + \epsilon\tau\eta_{\text{dqe}}n)}. \end{aligned} \quad (4.7)$$

The warm emissivity is calculated as

$$\epsilon = 1 - \eta_{\text{win}} + \eta_{\text{win}}(1 - \eta_{\text{tel}} + \eta_{\text{tel}}(1 - \eta_{\text{atm}})), \quad (4.8)$$

where $\eta_{\text{win}} = 0.96$ is the transmission of the warm polyethylene entrance window, $\eta_{\text{tel}} = 0.75$ is the forward telescope coupling (measured in section 5.1), and η_{atm} is the atmospheric transmission. The cold transmission is $\tau \approx 0.23$ and $\tau \approx 0.35$ at the centers of the two bands (see section 3.6), the detector quantum efficiency is $\eta_{\text{dqe}} = 0.58 - 0.82$, and the bandwidth is $\Delta\nu \approx \nu/1500$. While the results of section 4.5 indicate that the optical efficiency of the system in the 450 μm band may be larger than modeled, for the purposes of this calculation we use the nominal transmission values.

In Table 4.1 we list the theoretical values of NEP_{photon} for ZEUS, where η_{atm} is the zenith atmospheric transmission calculated for a precipitable water vapor level of 700 μm . At the centers of both bands the photon noise reaches $NEP_{\text{photon}} \approx 4 \times 10^{-17} \text{ W}/\sqrt{\text{Hz}}$, and it drops at the edges of the windows as the bandpass filter transmission tapers off. Multiplying by the electrical responsivity gives the noise equivalent voltage (NEV) at the detector, and we find peak values of $NEV_{\text{photon}} \approx 15$ and 21 $\text{nV}/\sqrt{\text{Hz}}$ on the 450 and 350 μm halves of the array, respectively.

4.6.2 Detector Noise

The two fundamental sources of noise originating in a bolometer are Johnson noise and thermal noise, and are characterized by [80]. Johnson noise is produced by the thermal motion of charge carriers in the bolometer, which results in an NEV at the detector output of

$$NEV_{\text{Johnson}} = \sqrt{4k_B T R} \left(\frac{Z + R}{2R} \frac{R_L}{Z + R_L} \right), \quad (4.9)$$

where the dynamic impedance is $Z = dV/dI$. The first term in this expression is the normal voltage noise across a resistor, and the second term accounts for the noise reduction from electrothermal feedback. A voltage fluctuation which adds to the bias voltage will increase the power dissipated in the bolometer, thereby increasing the temperature and decreasing the impedance. As the bolometer is approximately current-biased, this decreased impedance will reduce the net voltage increase across the detector. A voltage fluctuation with the opposite polarity will be partially countered in an analogous manner, and for the ZEUS bolometers this electrothermal feedback correction term is ≈ 0.7 . The dynamic impedance Z is derived from the shape of the load curve, and the mean value of the Johnson noise is $NEV_{\text{Johnson}} \approx 9 \text{ nV} / \sqrt{\text{Hz}}$.

Fluctuations in the power flow between the bolometer and the thermal sink produce a noise described by

$$NEP_{\text{thermal}} = \sqrt{4k_B G_d T^2} \sqrt{\frac{\beta + 1}{2\beta + 3} \frac{x^{2\beta+3} - 1}{x^{\beta+1} - 1} \frac{1}{x^{\beta+2}}}, \quad (4.10)$$

where the first term is appropriate for an isothermal system at T , the second term is ≈ 0.9 and corrects for the lower mean temperature of the thermal link, and $x = T/T_0$. The thermal noise is $NEP_{\text{thermal}} \approx 2.5 \times 10^{-17} \text{ W} / \sqrt{\text{Hz}}$, and multiplying by S_E gives a mean value of $NEV_{\text{thermal}} \approx 9 \text{ nV} / \sqrt{\text{Hz}}$.

In addition to Johnson noise and thermal noise, ion-implanted silicon thermistors exhibit excess low frequency noise which follows a $1/f$ profile. The dependence of this noise on the temperature scale T_g , the operating temperature T , and the thermistor volume has been characterized by [42], and for the ZEUS bolometers we estimate it contributes $NEV_{1/f} \approx 5 \text{ nV}/\sqrt{\text{Hz}}$ at 2 Hz.

4.6.3 Amplifier Noise

As the detector signal is buffered and amplified it picks up additional noise from the JFET impedance converters and the warm preamplifier electronics. The JFETs generate an input noise voltage e_N applied at the gate, which can be explained as the Johnson noise resulting from the FET transconductance. Shot noise from the gate leakage current (I_g) also produces a current noise $I_N = \sqrt{2qI_g}$. This current is drawn through the bolometer, such that the resultant voltage noise at the gate is $V_N = RI_N$. In addition to these white noise sources, FETs also show $1/f$ -like noise whose origins are not completely understood, and which we don't attempt to characterize here.

The JFETs used in ZEUS (InterFET 2N6451) are specified to have a high frequency voltage noise below $e_N = 3 \text{ nV}/\sqrt{\text{Hz}}$ and a gate leakage current below 0.1 nA. This leakage current would correspond to a current noise of $I_N = 5.7 \times 10^{-15} \text{ A}/\sqrt{\text{Hz}}$, which when drawn through the $\approx 13 \text{ M}\Omega$ bolometers would produce $V_N \approx 74 \text{ nV}/\sqrt{\text{Hz}}$. However, the gate leakage current is expected to decrease by a factor of 2 for every 10 degree drop below room temperature [52]. Operating at 250 K, the current noise should then be a factor of $\approx \sqrt{32}$ lower, corresponding to $V_N \approx 13 \text{ nV}/\sqrt{\text{Hz}}$. The first stage of the

warm preamplifier circuit is a low noise OPA27 operational amplifier, specified to provide a typical input white noise of $3 \text{ nV}/\sqrt{\text{Hz}}$ which increases to $5 \text{ nV}/\sqrt{\text{Hz}}$ at 2 Hz. Combined, these electronics should produce a maximum noise of $NEV_{\text{FET+Amp}} \approx 14 \text{ nV}/\sqrt{\text{Hz}}$, plus a possible additional $1/f$ excess from the JFETs.

4.6.4 Measured Noise

Summing the above estimates of the photon noise, detector noise, and amplifier noise in quadrature, we obtain estimates of the full system noise of $NEV_{\text{total}} \approx 20 - 26 \text{ nV}/\sqrt{\text{Hz}}$ for $\lambda \approx 430 - 470 \mu\text{m}$ and $NEV_{\text{total}} \approx 20 - 31 \text{ nV}/\sqrt{\text{Hz}}$ for $\lambda \approx 340 - 370 \mu\text{m}$. These ranges reflect the systematic changes in NEP_{photon} and in the detector operating conditions across these bands, as well as differences between individual detectors. During the March 2008 observing run the median noise measured at the centers of both telluric windows was $NEV_{\text{measured}} \approx 28 \text{ nV}/\sqrt{\text{Hz}}$, in good agreement with the noise model. This indicates that for the system configuration used in March 2008, the detectors and electronics combined to increase the noise by a factor of ~ 2 above the photon noise limit.

In subsequent observing runs in December 2008 and March 2009 the instrument setup was modified, such that the system noise is now closer to the background photon limit. The most important modification was an improved heat strap connecting the detector package to the ^3He refrigerator, which provides a lower sink temperature to the bolometers and results in a larger responsivity. This change in the responsivity increases the photon voltage noise more than it does any other noise term, thereby increasing the fractional contribution of

NEV_{photon} to NEV_{total} . We also exchanged the $350 \mu\text{m}$ bandpass filter for a new filter which has good transmission over a broader wavelength range, resulting in an increased system transmission at the edges of the telluric window. The sensitivity estimates made in the next section refer to this new configuration.

4.7 Sensitivity Estimate

The sensitivity of a direct-detection spectrometer is typically characterized by the noise equivalent flux density (NEFD), referred to a point source above the atmosphere. To estimate the NEFD of ZEUS on the CSO we begin by measuring the system response V_{cal} to a chopped thermal load $\Delta I_{\nu,\text{cal}} = B_{\nu}(T_{\text{hot}}) - B_{\nu}(T_{\text{cold}})$ placed at the front of the foreoptics. We then make a blank sky observation on a night with good atmospheric transmission and measure the system noise σ_{ν} . Defining the signal to noise ratio as $(S/N)_{\text{cal}} = V_{\text{cal}}/\sigma_{\nu}$, the NEFD is then calculated as

$$NEFD = \Delta I_{\nu,\text{cal}} \frac{\sqrt{2t_{\text{int}}}}{(S/N)_{\text{cal}}} \frac{\Omega_0}{\eta_{\text{atm}}\eta_{\text{ps}}}, \quad (4.11)$$

where Ω_0 is the solid angle on the sky which we expect to sample given the ZEUS optical design, and $\eta_{\text{ps}} = 0.25 - 0.41$ is the point source coupling. The formal definitions of Ω_0 and η_{ps} are given in chapter 5. We calculate η_{atm} as the zenith transmission for a precipitable water vapor level of $700 \mu\text{m}$, which is comparable to the line of sight transmission at the time of our noise measurements. The NEFD measured at several wavelengths is tabulated in Table 4.2.

These NEFD values are obtained from measurements of continuum sources (laboratory thermal loads and planets), in which the flux density is constant over a broad spectral range. For sources which emit radiation in narrow spectral

Table 4.2: ZEUS/CSO Sensitivity

Wavelength [μm]	$NEFD^a$ [Jy/ $\sqrt{\text{Hz}}$]	$NEFD_{\text{BL}}^b$ [Jy/ $\sqrt{\text{Hz}}$]	$T_{\text{rx}}(\text{SSB})^c$ [K]
336	14	13	12
342	11	9.3	2
347	12	10	6
350	12	9.3	18
357	15	12	17
367	16	12	28
371	21	15	42
378	37	30	8
423	26	12	247
427	13	7.8	92
435	8.2	5.9	35
438	7.3	5.6	24
446	12	5.8	140
459	14	6.1	187
469	26	7.8	407

^aRefers to a point source above the atmosphere, and includes the $\times 2$ sensitivity loss incurred by beam switching (chopping). The assumed atmospheric transmission is the zenith transmission for a precipitable water vapor level of $700 \mu\text{m}$.

^bNEFD for a background-limited spectrometer with the same optical efficiency and point source coupling as ZEUS on the CSO.

^cEquivalent receiver temperature for a single sideband heterodyne receiver (this quantity is telescope-independent).

lines, the relevant quantity to compare with this NEFD is the flux density averaged over a detector bandwidth, $\langle F_\nu \rangle_{\text{detector}}$. The signal to noise ratio achieved by a single detector is then given as

$$S/N = \alpha \frac{\langle F_\nu \rangle_{\text{detector}}}{NEFD} \sqrt{2t_{\text{int}}}, \quad (4.12)$$

where α is a correction term of order unity which accounts for the detailed spectral distribution of the emission. For broad lines $\alpha = 1$, and in the monochromatic limit $\alpha = 0.84 \rightarrow 0.76$ at $\lambda = 330 \rightarrow 480 \mu\text{m}$.

4.7.1 Comparison with the Background Limit

It is of interest to compare the measured sensitivity with that of an idealized spectrometer which is subject only to the noise from background photons, but which is otherwise identical to ZEUS on the CSO. Using equation 4.7 we can express the NEFD of such a background-limited system as

$$\begin{aligned}
 NEFD_{\text{BL}} &= 2 \times \frac{NEP_{\text{photon}}}{\eta_{\text{win}} \tau \eta_{\text{dqe}}} \frac{2}{\lambda^2 m \Delta \nu} \frac{\Omega_0}{\eta_{\text{atm}} \eta_{\text{ps}}} \\
 &= 2 \times \frac{2h\nu}{\lambda^2} \sqrt{\frac{2\epsilon n (1 + \epsilon \tau \eta_{\text{dqe}} n)}{m \Delta \nu \tau \eta_{\text{dqe}}}} \frac{\Omega_0}{\eta_{\text{win}} \eta_{\text{atm}} \eta_{\text{ps}}}, \quad (4.13)
 \end{aligned}$$

where the additional factor of 2 accounts for chopping losses (see section 5.2.3). As discussed in section 4.5, the 450 μm half of the detector array appears to receive more power from external sources than expected, likely due to an underestimate of the system transmission. We must therefore evaluate equation 4.13 using an increased estimate of $(\tau \eta_{\text{dqe}})$, chosen to match the modified transmission profile derived in section 4.5. This amounts to an increase of $(\tau \eta_{\text{dqe}})$ by a factor of ≈ 1.75 at the center of the band.

The resulting estimates of the $NEFD_{\text{BL}}$ are tabulated in Table 4.2. A comparison with the measured values of the NEFD shows that the sensitivity of the current system is within a factor of ≈ 1.4 of the background limit over the full 350 μm telluric window, and over most of the window (shortward of $\lambda \approx 365 \mu\text{m}$) it is within a factor of $\approx 1.2 - 1.3$. The best sensitivity achieved in the 450 μm window is at $\lambda = 438 \mu\text{m}$, where the NEFD is ≈ 1.3 times higher than the background-limited value. We note that if we would choose to account for the apparent excess system transmission in the 450 μm band by increasing our estimate of $(m \Delta \nu)$ rather than of $(\tau \eta_{\text{dqe}})$, we would find that the $NEFD_{\text{BL}}$ is a factor of ≈ 1.2 smaller, and conclude that the system is correspondingly farther from

this fundamental sensitivity limit. These estimates of the NEFD/NEFD_{BL} ratios are consistent with the noise budget discussed in section 4.6 and the recent improvements to the system sensitivity described in section 4.6.4.

4.7.2 Comparison with Heterodyne Receivers

It is also useful to express the sensitivity of ZEUS with the same terminology used for heterodyne instruments, which are characterized by a receiver temperature T_{rx} . The measured signal to noise ratio on our chopped thermal load is used to calculate a temperature noise σ_T by

$$(S/N)_{\text{cal}} = \frac{\lambda^2}{2k_B} \frac{\Delta I_{\nu, \text{cal}}}{\sigma_T}. \quad (4.14)$$

This is then related to T_{rx} by the radiometer equation

$$\sigma_T = \frac{2(T_{\text{rx}} + T_{\text{bg}})}{\sqrt{\Delta\nu t_{\text{int}}}}, \quad (4.15)$$

where the factor of 2 accounts for chopping losses. The contribution of the background radiation to the system noise is given by

$$T_{\text{bg}} = [1 - \eta_{\text{tel}} + \eta_{\text{tel}}(1 - \eta_{\text{atm}})] \frac{\lambda^2 B_{\nu}(T_{\text{amb}})}{2k_B}, \quad (4.16)$$

where we take the ambient temperature to be $T_{\text{amb}} = 265$ K. We use these expressions to calculate an equivalent receiver temperature for ZEUS, and include these values in Table 4.2.

It is important to keep in mind that the radiometer equation is generally used to describe systems which couple to $m = 1$ spatial and polarization modes, and which consequently make $\Delta\nu t_{\text{int}}$ independent samples of the background radiation field. For such a system, the lowest possible receiver temperature obtained

using equation 4.15 is $T_{\text{rx}} = 0$. This is equivalent to stating that the ideal receiver does not add any additional noise to that produced by the background photons. A system such as ZEUS which couples to $m > 1$ modes makes a correspondingly larger number of independent samples of the radiation field per unit $\Delta\nu t_{\text{int}}$, and the application of equation 4.15 may therefore yield $T_{\text{rx}} < 0$. As an example, a truly background-limited system with an NEP given by equation 4.7 and with the same optical efficiencies as ZEUS would be described by $T_{\text{rx}} = -20$ K at $\lambda = 350 \mu\text{m}$. In this sense the use of equation 4.15 to describe a multi-moded system such as ZEUS is less physically motivated, but it does facilitate a direct comparison with heterodyne receivers. Specifically, the sensitivity advantage of ZEUS over a single sideband heterodyne receiver with $T_{\text{rx,het}}$, referred to the front of the instrument (i.e., on the T_A scale, see section 5.1.1), is simply equal to $[T_{\text{rx,het}} + T_{\text{bg}}]/[T_{\text{rx,ZEUS}} + T_{\text{bg}}]$. This advantage is a factor of 2 larger if the receiver operates in double sideband mode, as it then receives noise power over twice the bandwidth.

The best reported heterodyne receiver temperature in the $450 \mu\text{m}$ window is $T_{\text{rx}}(\text{SSB}) \approx 250$ K [39]. ZEUS achieves comparable sensitivity over most of the band, and at $\lambda = 438 \mu\text{m}$ is a factor of ≈ 2.2 times more sensitive. In the $350 \mu\text{m}$ window the lowest reported heterodyne receiver temperatures are $T_{\text{rx}}(\text{DSB}) \approx 270$ K at $\lambda = 340 \mu\text{m}$, decreasing to $T_{\text{rx}}(\text{DSB}) = 205$ K at $\lambda = 375 \mu\text{m}$ [64]. The sensitivity advantage of ZEUS then decreases from ≈ 5.0 to ≈ 3.4 over the same range.

CHAPTER 5

BEAM COUPLING AND CALIBRATION

In this chapter we describe the optical coupling between ZEUS and the telescope, estimating the various efficiencies and the beam profile. We focus on characterizing the system used in the December 2006 observing run, which was the first run in which the atmospheric transmission was sufficiently high to allow accurate measurements of our coupling to the planets. When necessary, we supplement this discussion with auxiliary measurements made in subsequent runs. We also describe our procedures for flux calibration, spectral calibration, and sky subtraction.

5.1 Beam Coupling

5.1.1 Coupling Terms and Definitions

We begin by introducing the terms and conventions commonly used in millimeter- and submillimeter-wave astronomy to describe the brightness of a radiation source and the signal recorded by a spectrometer. A source with specific intensity I_ν is described by a radiation temperature T_R as

$$T_R = \frac{\lambda^2}{2k_B} I_\nu, \quad (5.1)$$

which is motivated by the fact that for a blackbody radiating in the Rayleigh-Jeans limit, T_R is equal to the physical temperature. It is also customary to report the measured signal as an antenna temperature $T_A = P_\nu/k_B$, where P_ν is the power per unit bandwidth delivered to the instrument. We convert all ZEUS measurements to the T_A scale by first measuring the system voltage response

V_{cal} to a chopped load with radiation temperature ΔT_{cal} placed in front of the foreoptics. We define the system gain as $G = V_{\text{cal}}/\Delta T_{\text{cal}}$, and convert all subsequent voltage measurements to an equivalent antenna temperature $T_A = V/G$.

Observations of an astronomical source with peak radiation temperature T_R through an atmosphere with line of sight transmission η_{atm} will yield an antenna temperature T_A given by [66]

$$T_A = T_R \eta_{\text{tel}} \eta_{\text{atm}} \eta_{\text{fss}} \eta_c. \quad (5.2)$$

To understand the origins of each of the coupling terms in equation 5.2, we consider the instrument to be a source of radiation, and examine how the telescope transmits and distributes this radiative power. The fraction of the power sent by the telescope toward the sky is equal to η_{tel} , a term which accounts for ohmic loss in the telescope mirrors and scattering toward the ground and the dome. The fraction of this forward-directed power which is sent within a solid angle Ω_d is equal to η_{fss} , where the size of Ω_d is chosen to differentiate between power associated with the main diffraction pattern and power scattered to large forward angles. Within Ω_d the power is distributed in a power pattern $P_n(\Omega)$, and the fraction of this power which couples to a source is given by

$$\eta_c = \frac{\int P_n(\Omega) B_n(\Omega) d\Omega}{\int_{\Omega_d} P_n(\Omega) d\Omega}, \quad (5.3)$$

where $B_n(\Omega)$ is the source distribution, and both P_n and B_n are normalized to have peak values of unity.

5.1.2 Estimate of η_{tel}

We estimate η_{tel} by conducting skydips, which consist of chopping between a calibrated load and the blank sky at several telescope elevations between the

zenith and the horizon. Under the assumption that the telescope, the dome, and the ground have the same radiation temperature T_{amb} , we can write the response as

$$T_A = T_{\text{cal}} - \left[(1 - \eta_{\text{tel}})T_{\text{amb}} + \eta_{\text{tel}}T_{\text{sky}}(1 - e^{-\tau_z A}) \right], \quad (5.4)$$

where τ_z is the zenith sky opacity, A is the airmass, and T_{sky} is the radiation temperature of the sky in the limit $A \rightarrow \infty$. In Figure 5.1 we show two skydips measured simultaneously in the 350 and 450 μm bands in March 2007 along with the model fits, in which τ_z and η_{tel} are taken as free parameters. A subsequent pair of skydips suggested somewhat larger values of η_{tel} , and consequently we adopt a mean value of $\eta_{\text{tel}} = 0.75$ in both bands.

5.1.3 Estimate of η_{fss}

We estimate η_{fss} with observations of large planets, which are the brightest objects in the sky at submillimeter wavelengths. This procedure requires accurate knowledge of the atmospheric transmission, and we use the transmission information provided by the CSO. The observatory uses a pair of sky monitors to estimate the atmospheric opacity at $\nu = 225$ GHz and $\lambda = 350$ μm . Each instrument performs a 10 minute skydip and reports the resultant zenith opacity at the relevant wavelength, either τ_{225} or τ_{350} . The CSO also provides an atmospheric transmission model [90], such that either τ_{225} or τ_{350} may be converted to a zenith opacity at the wavelength of interest. We find that τ_{350} gives systematically larger opacities than τ_{225} , and as τ_{350} is measured close to our operating wavelengths we use it to estimate the atmospheric transmission in this section.

For the December 2006 observing run the only large planet available was

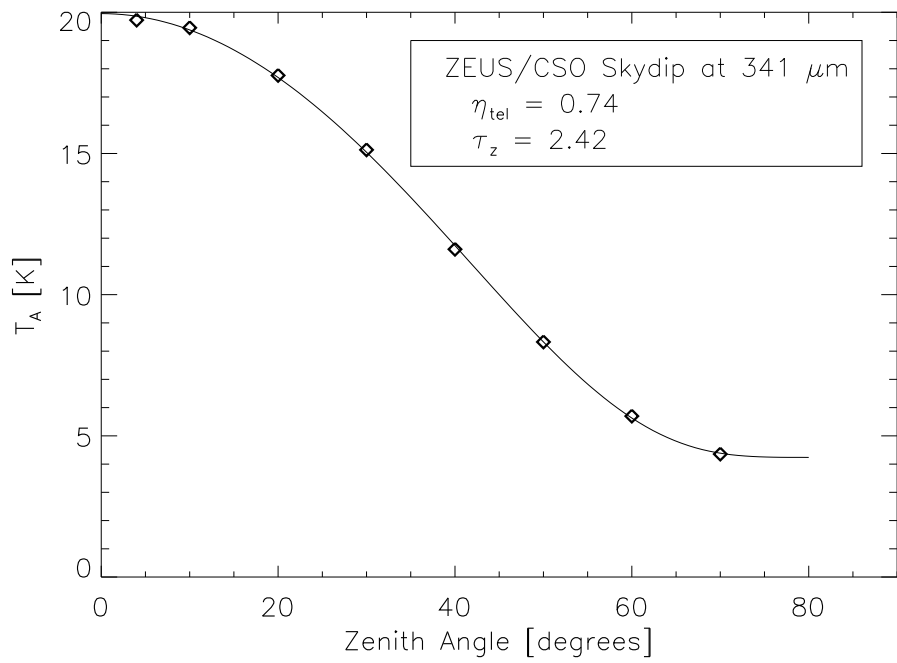
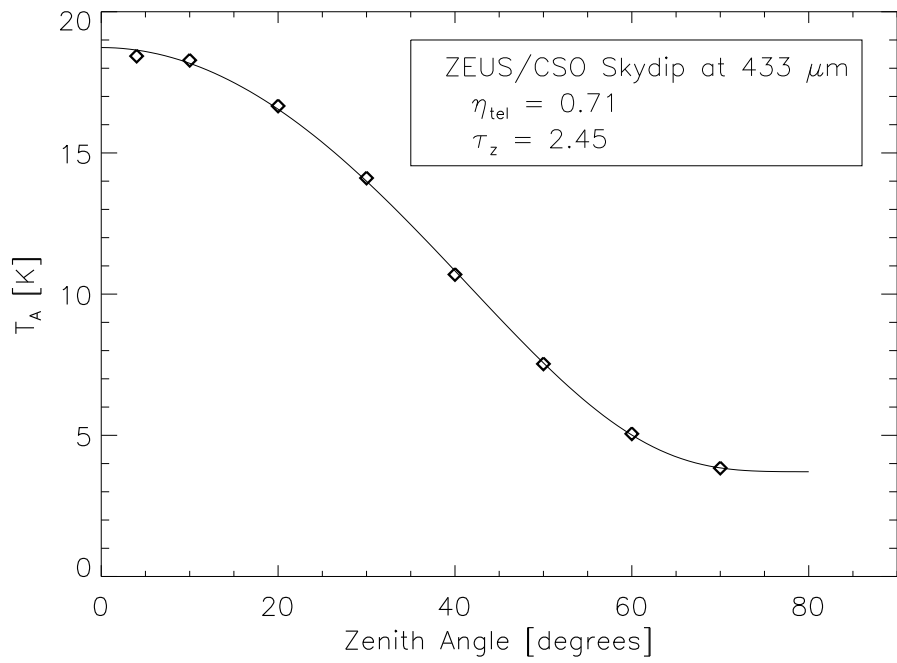


Figure 5.1: ZEUS/CSO skydips obtained in March 2007, along with model fits used to derive η_{tel} .

Saturn, which had a $19''$ diameter disk. Model fits to broadband measurements indicate that the radiation temperature of Saturn ranges from 90–93 K in the $350\ \mu\text{m}$ window, and 99 – 105 K in the $450\ \mu\text{m}$ window [49]. However, high resolution spectroscopy shows a $\approx 25\%$ PH_3 absorption feature centered at $\lambda \approx 375\ \mu\text{m}$ with a width of $\Delta\lambda \approx 12\ \mu\text{m}$ [85], and at wavelengths longer than $\lambda = 360\ \mu\text{m}$ we reduce the broadband-measured temperature accordingly. We observed Saturn at several wavelengths throughout the run, and for each measurement calculate an atmospheric-corrected coupling $\eta_{\text{Sat}} = T_A / (T_{R,\text{Sat}}\eta_{\text{atm}})$. Averaging over all measurements we find $\eta_{\text{Sat}} = 0.24$ in the $450\ \mu\text{m}$ band and $\eta_{\text{Sat}} = 0.21$ in the $350\ \mu\text{m}$ band, with estimated standard deviations of $\approx 10\%$.

While observations of Saturn allow us to directly measure the efficiency with which ZEUS/CSO couples to a $19''$ source, it is preferable to use a larger solid angle Ω_d to estimate η_{fss} . In subsequent observing runs in March 2007 and March 2008 both Saturn and Jupiter were available, with Saturn at diameters of $19'' - 20''$ and Jupiter at diameters of $36'' - 40''$. Observations of the two planets indicate that while the absolute coupling to either varied somewhat from run to run, the ratio $\eta_{\text{Jup}} \approx 1.4\eta_{\text{Sat}}$ was roughly constant and the same in both windows. Assuming this ratio is appropriate for the December 2006 observations, we adopt a $40''$ diameter for Ω_d and estimate $\eta_{\text{fss}} = 1.4\eta_{\text{Sat}}/\eta_{\text{tel}} = 0.45$ in the $450\ \mu\text{m}$ band, and $\eta_{\text{fss}} = 0.39$ in the $350\ \mu\text{m}$ band.

5.1.4 Contributions to η_{fss}

The above estimates of η_{fss} suggest that more than half of the forward-directed power is distributed outside of the central $40''$, and here we attempt to account

for this loss. The low value of η_{fss} is due in part to beam spillover at the secondary mirror, which results in power sent directly to large angles on the sky. The telescope illumination is controlled by the Lyot stop in ZEUS, which is linearly oversized by 14%, resulting in a corresponding over-illumination of the secondary. By placing chopped loads directly in front of and adjacent to the secondary, we find that only 68% of the power reaching the plane of the secondary falls within the mirror aperture, with the rest spilling over. We define this efficiency as $\eta_{\text{sec}} = 0.68$.

Additionally, a fraction of the power is scattered to large forward angles by irregularities in the primary mirror surface. This effect is characterized by the Ruze efficiency, which for the simplified case of random small-scale surface errors with variance σ^2 is given as [35]

$$\eta_{\text{Ruze}} = \exp\left[-\left(\frac{4\pi\sigma}{\lambda}\right)^2\right]. \quad (5.5)$$

The form of the above equation allows us to estimate σ if η_{Ruze} is measured at two wavelengths. We previously estimated that the coupling to Saturn in the 450 μm band is 1.15 times better than the coupling in the 350 μm band, and attributing this to differences in the Ruze efficiency at $\lambda = 450 \mu\text{m}$ and $\lambda = 350 \mu\text{m}$ we derive $\sigma = 17 \mu\text{m}$. This estimate of σ then gives mean values of $\eta_{\text{Ruze}} = 0.80$ in the 450 μm band and $\eta_{\text{Ruze}} = 0.69$ in the 350 μm band, with a small variation across either window. We note that while the absolute values of η_{Sat} vary from measurement to measurement with a 10% scatter, the ratio of couplings in the two bands are better constrained. The CSO employs a surface correction system which actively adjusts the primary mirror panels to compensate for gravitational deformation, and which can potentially lower the surface deviations from $\sigma = 25 \mu\text{m}$ to $\sigma = 10 \mu\text{m}$ [68]. Our above analysis suggests that ZEUS/CSO benefits from this system, but does not achieve the ultimate surface

accuracy.

The scattered power is redistributed in a Gaussian error pattern with a FWHM of $\Delta\theta \approx 1.06\lambda/c$, where c is the correlation length of the surface irregularities [1]. It is unlikely that c is larger than the 1.15 m size of the primary mirror panels, which for $\lambda = 350 \mu\text{m}$ would correspond to $\Delta\theta \approx 67''$, and only 22% of this pattern would couple to the 40'' diameter Ω_d . Combining the above estimates of η_{Ruze} and η_{sec} we find $\eta_{\text{Ruze}}\eta_{\text{sec}} = 0.54$ in the 450 μm band and $\eta_{\text{Ruze}}\eta_{\text{sec}} = 0.47$ in the 350 μm band, factors of ≈ 1.2 larger than the values of η_{fss} estimated above. Thus if we assume that most of the scattered power falls outside of Ω_d , the deviations of η_{fss} from unity can largely be explained by the combined effects of spillover at the secondary and scattering from an imperfect primary.

5.1.5 Beam Mapping

To estimate the last term in equation 5.2, η_c , we must first measure the normalized beam power pattern $P_n(\Omega)$. The ZEUS/CSO power pattern is determined by a combination of the telescope diffraction and the finite sizes of the slit and pixel. The expected beam profile is a convolution of the Airy pattern with a two-dimensional rectangle function, with the latter having a length equal to the pixel size and a width equal to the slit width. For the 10.4 m diameter CSO primary, the 7.2'' pixel size, and the 8.7'' slit width, this construction gives functions with a FWHM of 9'' – 11'' and aspect ratios of 1.05 – 1.10 across the 350 and 450 μm bands. Due to the limited precision with which $P_n(\Omega)$ may be measured, we model it as an axisymmetric Gaussian, with a fixed width for a given telluric

window.

In December 2006 we mapped the beam profile by taking total power scans across Uranus, which was $3.5''$ in diameter. Two such maps obtained simultaneously in the 350 and $450 \mu\text{m}$ bands are shown in Figure 5.2. The faintness of the source prevents a detailed measurement of the power pattern at large angles, but within $10''$ of the boresight the measured beam maps are well approximated by Gaussians of FWHM $10.2''$ and $10.9''$ convolved with a uniform brightness $3.5''$ diameter disk. Other beam maps obtained during this run give consistent sizes, and we model the main component of $P_n(\Omega)$ in the 350 and $450 \mu\text{m}$ windows as a Gaussian with $10''$ and $11''$ FWHM, respectively. This measured power pattern is somewhat broader than expected, likely due to the accumulation of optical aberrations in the instrument and telescope. Defining Ω_0 as the integrated solid angle of the expected power pattern, and Ω_{mb} as the integrated solid angle of the measured Gaussian beam profile, we find a mean ratio of $\Omega_{\text{mb}}/\Omega_0 \approx 1.1$.

The relative couplings to Uranus and Saturn are consistent with our model of $P_n(\Omega)$, but the coupling to Jupiter (assuming $\eta_{\text{Jup}} \approx 1.4\eta_{\text{Sat}}$) is $\approx 25\%$ larger than expected. This indicates the presence of an error pattern which becomes important at distances greater than $\approx 10''$ from the boresight. For observations of sources smaller than $\approx 20''$ the exact shape of this error pattern is not important, simply that its existence increases the denominator of equation 5.3 to $\int_{\Omega_d} P_n(\Omega)d\Omega \approx 1.25\Omega_{\text{mb}}$. With this model of $P_n(\Omega)$, our previous estimates of η_{tel} and η_{fss} , a measurement of η_{atm} , and knowledge of the source distribution $B_n(\Omega)$, the peak radiation temperature T_R may be estimated from the measured T_A using equations 5.2 and 5.3. In Table 5.1 we summarize the ZEUS/CSO beam

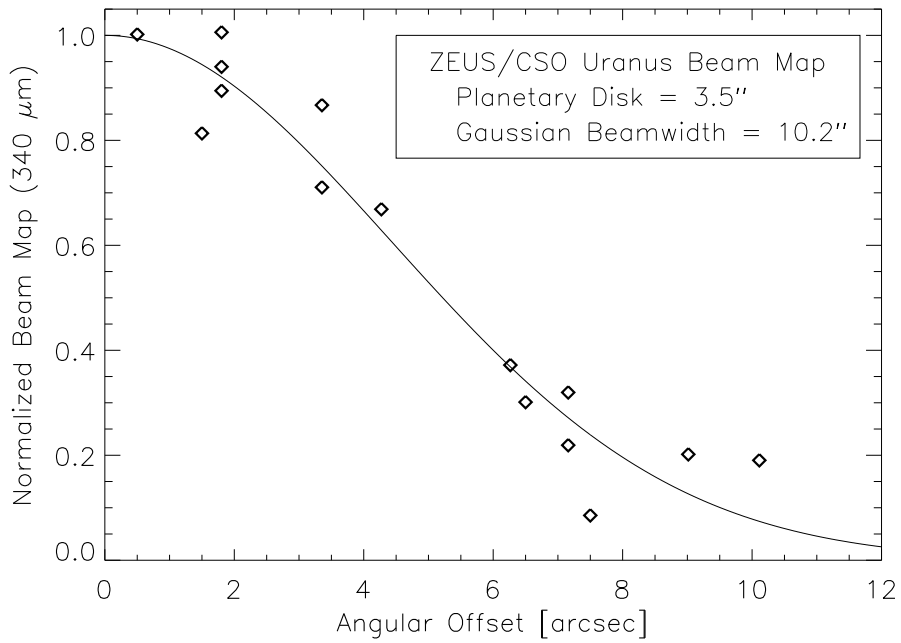
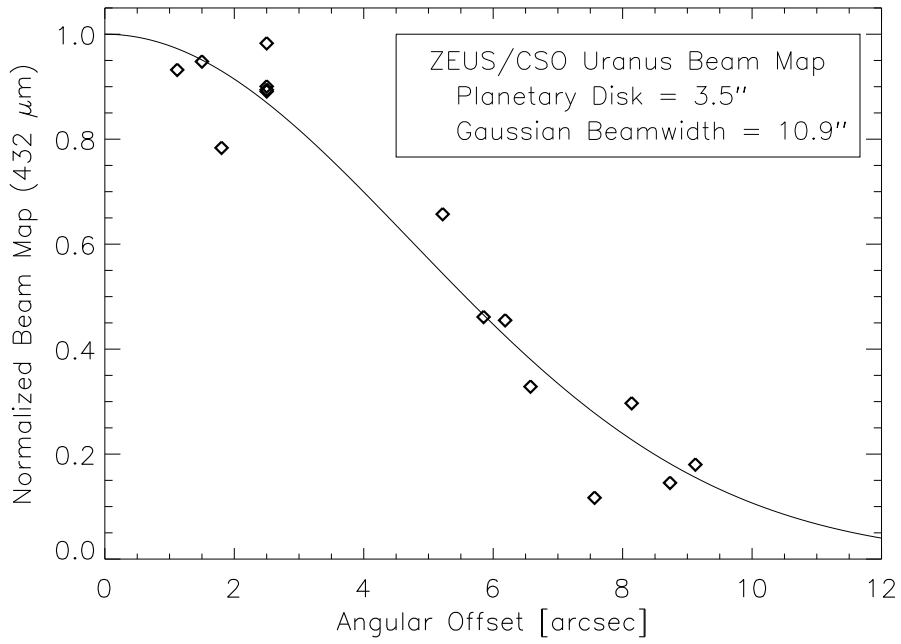


Figure 5.2: Radial profile of the ZEUS/CSO beam map obtained on Uranus in December 2006. Model curve is a convolution of the uniform temperature planet disk with the Gaussian beam profile.

Table 5.1: ZEUS/CSO Beam Parameters

Parameter	Symbol	450 μm	350 μm
Telescope Efficiency ^a	η_{tel}	0.75	0.75
Forward Efficiency ^b	η_{fss}	0.45	0.39
Secondary Coupling ^c	η_{sec}	0.68	0.68
Ruze Efficiency ^d	η_{Ruze}	0.80	0.69
Main Beam Width ^e	B	11'' \rightarrow 11.5''	10'' \rightarrow 11.5''
Main Beam Efficiency ^f	η_{mb}	0.36	0.32
Point Source Coupling ^g	η_{ps}	0.27 \rightarrow 0.38	0.21 \rightarrow 0.27

Note. – Beam Parameters measured for ZEUS on the CSO in December 2006. Also shown are the increased values of B and η_{ps} measured during the most recent observing run in March 2009. With the exception of η_{ps} , all parameters are assumed to be constant across the specified telluric window.

^aFraction of the power transmitted by the telescope in the forward direction.

^bFraction of the forward-directed power coupling to the central 40''.

^cAccounts for spillover off the secondary mirror onto the sky (subsumed in η_{fss}).

^dAccounts for the power scattered by the primary mirror to large forward angles (subsumed in η_{fss}).

^eFWHM of the Gaussian main beam power pattern. After the December 2006 run the slit width was increased from 8.7'' to 10.8'', and consequently the beam sizes measured in March 2009 were larger.

^fFraction of the forward-directed power coupling to the main Gaussian power pattern.

^gCoupling to a point source, relative to that which would be expected with a lossless telescope and the tightest possible beam profile. This parameter increases by a factor of ≈ 1.2 across a given telluric window, and here we list the mean value for both bands. The point source coupling in March 2009 was a factor of $\approx 1.3 - 1.4$ larger than in December 2006, likely due to an improved optical alignment between ZEUS and the telescope.

parameters.

5.2 Calibration

5.2.1 Flux Calibration

The coupling terms discussed in section 5.1 may be used to calculate the radiation temperature of a source given its normalized brightness distribution $B_n(\Omega)$,

but in general this function is not known. We therefore report our measurements on the main beam brightness temperature scale, T_{mb} . This temperature is defined as the equivalent radiation temperature of a source which uniformly fills the main beam, but which doesn't couple to any error patterns or sidelobes. It is related to the antenna temperature by

$$T_A = T_{\text{mb}}\eta_{\text{tel}}\eta_{\text{atm}}\eta_{\text{mb}}, \quad (5.6)$$

where η_{mb} is the fraction of the forward-directed power distributed in the main Gaussian component, and the product $T_{\text{mb}}\eta_{\text{mb}}$ replaces $T_R\eta_{\text{fss}}\eta_c$ in equation 5.2. We calculate η_{mb} directly from our previous estimates of the Saturn coupling by writing $\eta_{\text{Sat}} = \eta_{\text{tel}}\eta_{\text{mb}}\eta_{P,\text{Sat}}$, where $\eta_{P,\text{Sat}}$ is the fraction of the main beam which couples to the planet. For a Gaussian beam of width B centered on a uniform disk with diameter D we have $\eta_P = 1 - \exp[-\ln(2)D^2/B^2]$, and using our measured beam sizes to calculate $\eta_{P,\text{Sat}}$ we find $\eta_{\text{mb}} = 0.36$ in the $450 \mu\text{m}$ band and $\eta_{\text{mb}} = 0.32$ in the $350 \mu\text{m}$ band. With estimates of η_{tel} and η_{atm} we can then calculate T_{mb} from the measured T_A using equation 5.6.

We can also relate the antenna temperature measured from a point source to the source flux density F_ν by writing

$$T_A = \left(\frac{\lambda^2}{2k_B} \right) \frac{F_\nu}{\Omega_0} \eta_{\text{atm}}\eta_{\text{ps}}, \quad (5.7)$$

where η_{ps} is the point source coupling. This definition of the point source coupling is such that η_{ps} accounts both for the telescope coupling efficiencies that relate T_A/η_{atm} to T_{mb} , and for the reduction in the point source sensitivity that results from having a main beam power pattern which is broader than the tightest profile allowed by the ZEUS optical design. The point source coupling is related to previously defined quantities by

$$\eta_{\text{ps}} = \eta_{\text{tel}}\eta_{\text{mb}} \frac{\Omega_0}{\Omega_{\text{mb}}}, \quad (5.8)$$

and using the parameter values measured in December 2006 we calculate $\eta_{\text{ps}} = 0.19 \rightarrow 0.22$ for $\lambda = 330 \rightarrow 380 \mu\text{m}$ and $\eta_{\text{ps}} = 0.24 \rightarrow 0.29$ for $\lambda = 420 \rightarrow 480 \mu\text{m}$. In the March 2009 observing run the point source coupling increased to $\eta_{\text{ps}} = 0.25 \rightarrow 0.28$ for $\lambda = 330 \rightarrow 380 \mu\text{m}$ and $\eta_{\text{ps}} = 0.35 \rightarrow 0.41$ for $\lambda = 420 \rightarrow 480 \mu\text{m}$. This increase is likely due to an improved technique for aligning the instrument to the telescope, which has improved our coupling to the secondary mirror and may also have helped suppress the error pattern. These most recent values of η_{ps} are used in section 4.7 to calculate the point source sensitivity of ZEUS on the CSO.

The above values of η_{mb} and η_{ps} are calculated from Saturn observations using τ_{350} to estimate the atmospheric transmission (see section 5.1.3), and consistency requires that we use τ_{350} to calculate η_{atm} for the source observations as well. The sky opacities estimated from τ_{225} are systematically lower than those estimated from τ_{350} , but as long as the same sky monitor is used to calculate η_{atm} for the source and calibrator observations there is no systematic difference in the resulting values of T_{mb} or F_{ν} . To increase the statistical accuracy of the atmospheric correction, we compute two independent values of T_{mb} (or F_{ν}) using either τ_{225} or τ_{350} for both the source and calibrator observations, and average the results.

5.2.2 Spectral Calibration

Absolute spectral calibration may be obtained in the laboratory by placing a submillimeter-transparent vessel filled with CO gas between the instrument and a chopped hot load. The spectrometer is then exposed to the CO lines in ab-

sorption, and a measurement of the focal plane location of multiple lines may be measured as a function of grating incidence angle. The ray-trace and the grating equation are combined to construct a model $\lambda(x, \alpha)$ specifying the wavelength of the radiation imaged to a location (x) in the focal plane for a given incidence angle (α). This model has been verified by laboratory measurements of $^{12}\text{CO}(6\rightarrow5)$, $^{13}\text{CO}(6\rightarrow5)$, and $^{12}\text{CO}(7\rightarrow6)$, which require grating angles of $\alpha = 59^\circ$, 64° , and 69° , spanning the full useful range.

The absolute position of the grating is measured with limit switches located at either end of the grating range. Each time the instrument is cooled the position of the grating with respect to the limit switch reference is allowed to change by a small amount, which can be measured by applying the calibration model $\lambda(x, \alpha)$ to the measurement of a single spectral line. In principle this line measurement may be done in the laboratory, but due to pressure broadening in the laboratory environment the lines are ≈ 1.5 pixels wide. The final calibration is therefore obtained by observing a narrow-line Galactic source such as Orion (BN-KL).

5.2.3 Sky Subtraction

Due to the bright atmospheric emission at submillimeter wavelengths, we must carefully subtract the warm background, which is done by chopping and nodding the telescope. The secondary mirror chops at 2 Hz in azimuth with a $30''$ throw between the source and empty sky, and the ZEUS data acquisition program uses a lockin routine to difference the on-source and off-source signal. After ≈ 2 minutes the telescope nods $30''$, after which we chop between the source

and the empty sky location on the opposite side. By nodding the telescope back and forth we obtain the difference between the source position and the average of the positions offset in azimuth by $\pm 30''$. This procedure reduces the system sensitivity by a factor of 2, since we collect noise during the full integration but signal for only half the time.

CHAPTER 6
THE WARM, DENSE MOLECULAR GAS IN THE STARBURST NUCLEUS
OF NGC 253

We report the detection of $^{13}\text{CO } J = 6 \rightarrow 5$ emission from the nucleus of the starburst galaxy NGC 253. This is the first extragalactic detection of the $^{13}\text{CO } J = 6 \rightarrow 5$ transition, which traces warm, dense molecular gas. We employ a multi-line LVG analysis and find $\approx 35\% - 60\%$ of the molecular ISM is both warm ($T \sim 110$ K) and dense ($n_{\text{H}_2} \sim 10^4 \text{ cm}^{-3}$). We analyze the potential heat sources, and conclude that UV and X-ray photons are unlikely to be energetically important. Instead, the molecular gas is most likely heated by an elevated density of cosmic rays or by the decay of supersonic turbulence through shocks. If the cosmic rays and turbulence are created by stellar feedback within the starburst, then our analysis suggests the starburst may be self-limiting. This chapter presents an extended discussion of work published in the *Astrophysical Journal Letters* [41].

6.1 Introduction

NGC 253 is a nearby ($d \approx 2.5$ Mpc) [81], highly inclined ($i \approx 78^\circ$) [91] Sc galaxy undergoing a nuclear starburst [94]. The IR luminosity in the central $30''$ is $1.5 \times 10^{10} L_\odot$ [118], and the mid-IR morphology indicates most of this emission arises from a $7''$ region centered within $1''$ of the $2 \mu\text{m}$ nucleus [117]. Near-IR images show a prominent stellar bar [104] which likely plays a major role in channeling gas into the central starburst [92, 16]. Estimates of the gas mass in the central ~ 300 pc are in the range $(0.4 - 4.2) \times 10^8 M_\odot$ [65, 81, 44].

The $J = 6 \rightarrow 5$ and $J = 7 \rightarrow 6$ transitions of CO arise from states with

energy levels 116 K and 155 K above ground and have critical densities of $n_{\text{crit}} \approx 3 \times 10^5 \text{ cm}^{-3}$, and are thus sensitive probes of the warm, dense molecular gas found in regions of massive star formation. Observations of these lines in the starburst nucleus of NGC 253 [43, 8, 2, 40] have indeed shown that much of the molecular gas is highly excited, although a consensus on the details of the excitation have yet to be reached [40]. Using a multi-line excitation analysis, [8] find the central 180 pc contain a large mass ($[2 - 5] \times 10^7 M_{\odot}$) of warm ($T \sim 120 \text{ K}$), dense ($n_{\text{H}_2} \sim 4.5 \times 10^4 \text{ cm}^{-3}$) molecular gas, most likely heated by cosmic rays injected into the ISM by the many supernovae ($\sim 0.1 \text{ yr}^{-1}$) [121]. This model finds large optical depths in the mid-J¹ ^{12}CO lines, and thus predicts bright ^{13}CO emission. To further constrain the excitation and energetics of the molecular gas we observed the $^{13}\text{CO } J = 6 \rightarrow 5$ transition, which provides a strong constraint on the $^{12}\text{CO } J = 6 \rightarrow 5$ opacity. This is the first extragalactic detection of the $^{13}\text{CO } J = 6 \rightarrow 5$ transition, and the first detection of any ^{13}CO transition greater than $J = 3 \rightarrow 2$ from beyond the Magellanic Clouds.

6.2 Observations

We observed $^{12}\text{CO } J = 6 \rightarrow 5$ (433.56 μm), $J = 7 \rightarrow 6$ (371.65 μm), $^{13}\text{CO } J = 6 \rightarrow 5$ (453.50 μm), and the [CI] $^3\text{P}_2 \rightarrow ^3\text{P}_1$ fine-structure line (370.41 μm) toward NGC 253 in December 2006 with ZEUS at the Caltech Submillimeter Observatory (CSO) on Mauna Kea, Hawaii. We obtained flux calibration with observations of Saturn, as described in section 5.2.1, which was assumed to have brightness temperatures of 116 K, 118 K, and 97 K at 434 μm , 453 μm , and 371 μm , respectively [49, 85]. We observed the four lines over the course of three

¹In this chapter we use the term ‘mid-J’ to describe transitions with $J_{\text{upper}} = 3 - 7$.

nights in good submillimeter weather, with $\tau_{225 \text{ GHz}} = 0.04 - 0.06$. Observations of NGC 253 were centered at R.A. = $00^{\text{h}}47^{\text{m}}33^{\text{s}}.2$, decl. = $-25^{\circ}17'18''$ (J2000.0), and small maps in the ^{12}CO lines verified that the beam was centered within $4''$ of the CO emission peak (see Fig. 6.1). We used total power maps of Uranus to measure the FWHM of the beam to be $11''$ at $434 \mu\text{m}$ and $453 \mu\text{m}$ and $10''$ at $371 \mu\text{m}$. The spectra of $^{12}\text{CO } J = 6 \rightarrow 5$, $^{13}\text{CO } J = 6 \rightarrow 5$, and the $^{12}\text{CO } J = 7 \rightarrow 6$ and [CI] pair shown in Figure 6.2 represent total integrations times of 6, 70, and 5 minutes, respectively. A linear baseline is removed from all spectra, and the integrated intensities are listed in Table 6.1. In addition to the nuclear spectra we obtained a simultaneous map in the $^{12}\text{CO } J = 7 \rightarrow 6$ and [CI] lines, which is in preparation for journal submission (T. Nikola et al. 2009, in preparation).

6.3 Results: CO Excitation Analysis

6.3.1 LVG Model

To examine the CO excitation we assemble the lower-J line intensities from the literature, and correct all measurements to a common $15''$ beam. The $^{12}\text{CO } J = 4 \rightarrow 3$ intensity is obtained from [40], and the $J = 3 \rightarrow 2$ and lower transitions are taken from [44]. The $^{12}\text{CO } J = 6 \rightarrow 5$ map of [2] is used to correct the intensities measured here to a $15''$ scale, and when necessary the intensities obtained from [44] are corrected using power law interpolations as outlined in [8]. The line intensities used in our analysis are listed in Table 6.1. Figure 6.3 shows rotational level diagrams of ^{12}CO and ^{13}CO .

To quantitatively analyze the CO line SED we employ a large velocity gradi-

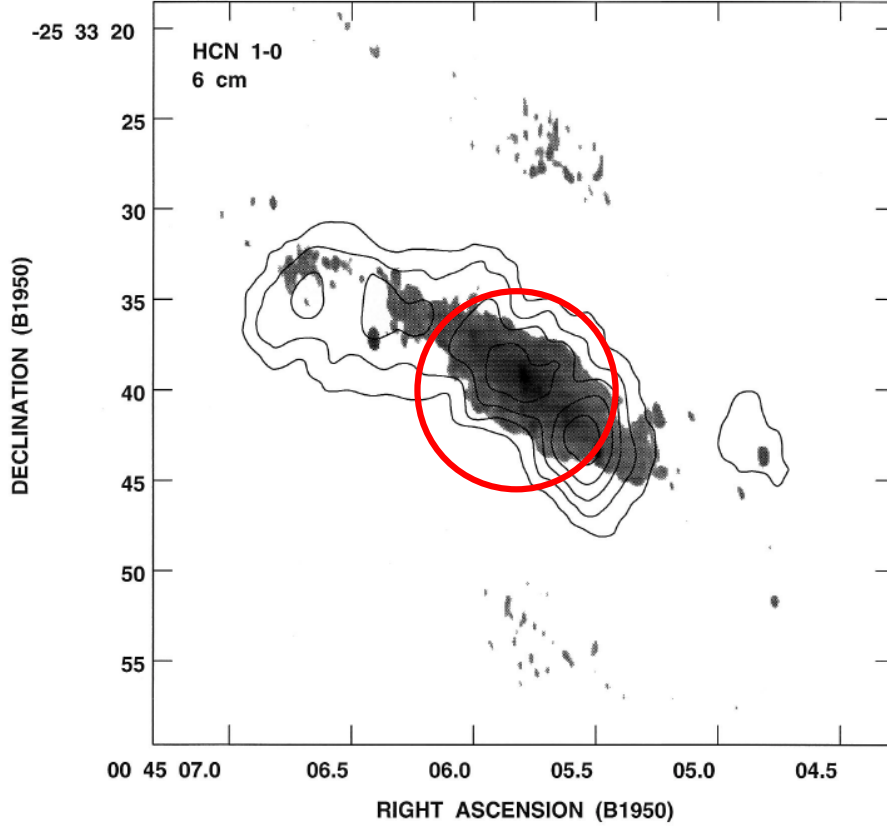


Figure 6.1: HCN $J = 1 \rightarrow 0$ emission (*contours*) and 6 cm map (*gray scale*) from [87, and references therein]. The 11'' beam used for the ^{12}CO and ^{13}CO $J = 6 \rightarrow 5$ observations is shown (*red circle*) centered at the location of all observations made in this work. Small maps in the ^{12}CO lines verified that the beam was centered within 4'' of the CO emission peak

ent (LVG) model, in which the excitation and opacity of the CO are determined by a gas density (n_{H_2}), kinetic temperature (T_{kin}), and CO abundance per velocity gradient ($[\text{CO}/\text{H}_2]/dv/dr$) (for a description of this model see Appendix A). We use an escape probability formalism with $\beta = (1 - e^{-\tau})/\tau$, derived for a spherical cloud undergoing uniform collapse [12, 33]. The source is assumed to contain a large number of these unresolved clouds, such that the absolute line intensities are proportional to a beam-averaged CO column density (N_{CO}). We increase the CO- H_2 collisional rate coefficients from [27] by 21% to account for collisions with He [8], and fix the H_2 ortho/para ratio at 3. The CO abundance is set to

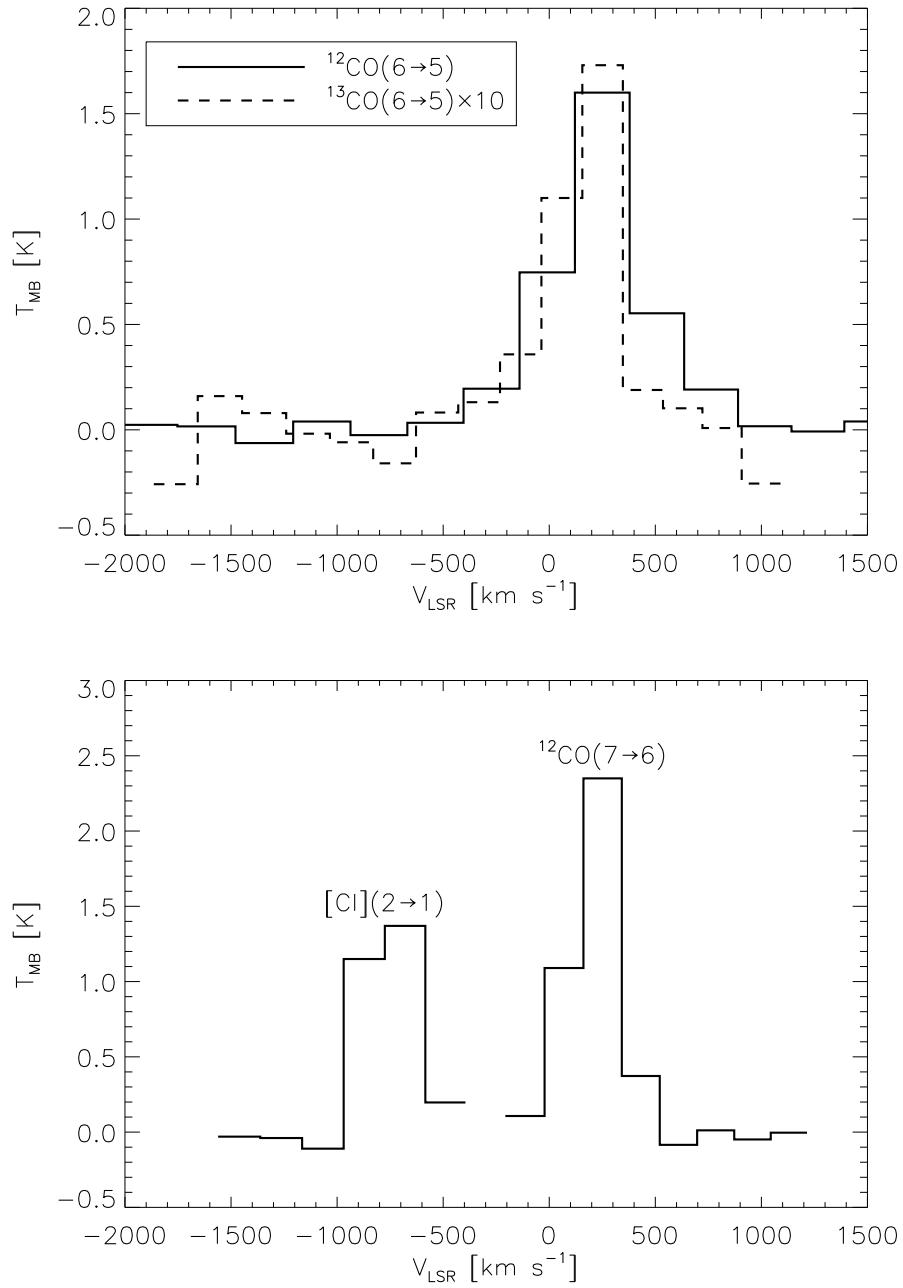


Figure 6.2: *Top:* Spectra of $^{12}\text{CO } J = 6 \rightarrow 5$ and $^{13}\text{CO } J = 6 \rightarrow 5$ (scaled by $\times 10$). *Bottom:* Spectrum of $^{12}\text{CO } J = 7 \rightarrow 6$ and [C I] $^3\text{P}_2 \rightarrow ^3\text{P}_1$ with a rogue pixel removed near the center. The velocity scale is referenced to $^{12}\text{CO } J = 7 \rightarrow 6$.

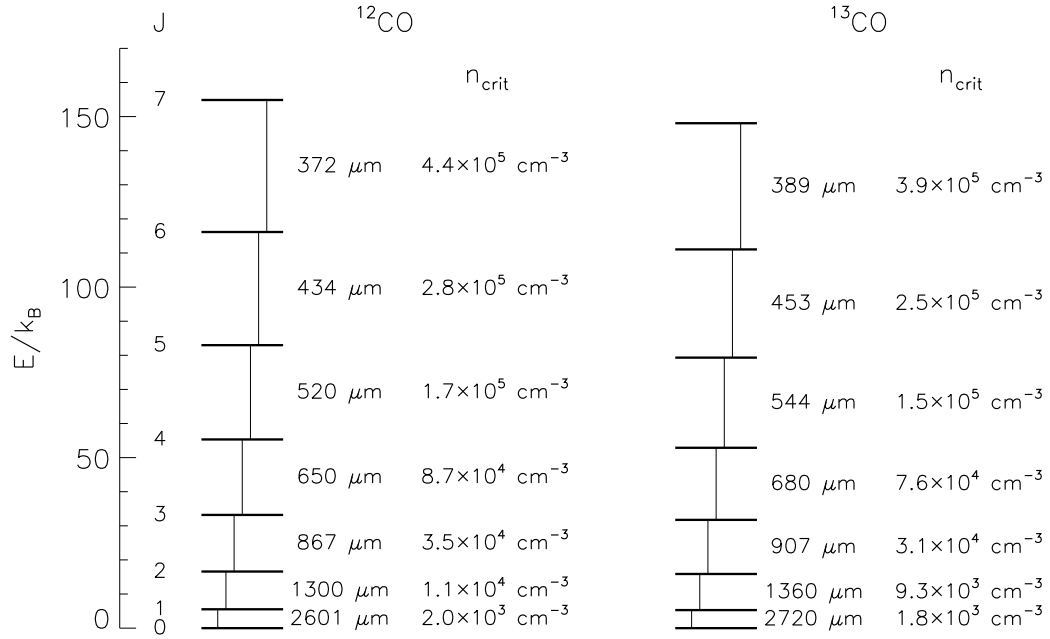


Figure 6.3: Lowest rotational levels of ^{12}CO and ^{13}CO , with the wavelengths and critical densities of each transition.

$[\text{CO}/\text{H}_2] = 8.5 \times 10^{-5}$ [28] and the isotopologue abundance ratio to $[\text{CO}/\text{H}_2]$ = 40 [47].

6.3.2 High Excitation Component

As for [8], we find that any single set of LVG model parameters capable of producing the mid-J emission underpredicts the $J = 2 \rightarrow 1$ and $J = 1 \rightarrow 0$ intensities, necessitating the adoption of a two component model. Previous authors have found that a single component can produce the ^{12}CO intensities and the $J = 3 \rightarrow 2$ and lower transitions of ^{13}CO [40], but such a model would not account for the bright ^{13}CO $J = 6 \rightarrow 5$ emission measured here. We begin by using the $J = 3 \rightarrow 2$ and higher transitions to constrain the high excitation component, and then introduce a low excitation component to account for the excess $J = 2 \rightarrow 1$ and $J = 1 \rightarrow 0$ emission.

Table 6.1: Integrated CO Line Intensities

Transition	Beam [$''$]	I [K km s $^{-1}$]	I [ergs s $^{-1}$ cm $^{-2}$ sr $^{-1}$]	σ [%]
$^{12}\text{CO}(6\rightarrow 5)$	11	854 ± 20	2.89×10^{-4}	30
	15	573	1.94×10^{-4}	30
$^{12}\text{CO}(7\rightarrow 6)$	10	694 ± 30	3.73×10^{-4}	30
	15	$418^{a,b}$	2.25×10^{-4}	30
$^{13}\text{CO}(6\rightarrow 5)$	11	65 ± 5	1.97×10^{-5}	30
	15	43	1.29×10^{-5}	30
$^{12}\text{CO}(1\rightarrow 0)$	15	1105	1.73×10^{-6}	22
$^{12}\text{CO}(2\rightarrow 1)$	15	1500	1.88×10^{-5}	16
$^{12}\text{CO}(3\rightarrow 2)$	15	1134	4.81×10^{-5}	14
$^{12}\text{CO}(4\rightarrow 3)$	15	1040	1.04×10^{-4}	15
$^{13}\text{CO}(1\rightarrow 0)$	15	94	1.29×10^{-7}	20
$^{13}\text{CO}(2\rightarrow 1)$	15	113	1.24×10^{-6}	12
$^{13}\text{CO}(3\rightarrow 2)$	15	117	4.33×10^{-6}	14

Note. – Intensities of $^{12}\text{CO } J = 6 \rightarrow 5$, $J = 7 \rightarrow 6$, and $^{13}\text{CO } J = 6 \rightarrow 5$ from this work, and lower- J intensities from [40] and [44]. All measurements have been corrected to 15'' using a methodology described in section 6.3.1. Intensities measured here have statistical errors listed in column 3, and total uncertainties (30%) dominated by systematic uncertainties in the high frequency sky transmission.

^a10% larger than the intensity reported by [40], and well within the calibration uncertainties.

^b[8] report an intensity calculated for a source which couples to half the power in the Gaussian main beam, rather than to the full main beam as is done here. Reducing their value by the corresponding factor of 2 yields an intensity 10% larger than measured here, well within the calibration uncertainties.

We calculate a four-dimensional grid of model CO line SEDs, varying n_{H_2} , T_{kin} , dv/dr , and N_{CO} over a large volume of parameter space. Comparing these model calculations to the observed mid- J CO line intensities, we find solutions giving $\chi_{\text{reduced}}^2 \lesssim 1$ for values of $dv/dr \gtrsim 3 \text{ km s}^{-1} \text{ pc}^{-1}$. In Figure 6.4 we plot the values of n_{H_2} and T_{kin} giving the best fits for velocity gradients in the range $dv/dr = 3 - 320 \text{ km s}^{-1} \text{ pc}^{-1}$. Over the modeled range of dv/dr these values change by an order of magnitude or more, so to further restrict parameter space we must apply prior constraints to dv/dr and T_{kin} .

In the LVG approximation the velocity gradient is produced by large-scale systematic motion, but for a self-gravitating cloud in virial equilibrium we can approximate $dv/dr \approx 3.1 \text{ km s}^{-1} \text{ pc}^{-1} \sqrt{n_{\text{H}_2}/10^4 \text{ cm}^{-3}}$ [34]. Allowing that dv/dr may be larger due to the presence of an additional stellar mass density or a high-pressure intercloud medium [8], we set an upper limit ~ 10 times larger at $dv/dr \leq 40 \text{ km s}^{-1} \text{ pc}^{-1}$. T_{kin} is restricted by the results of [96], who conclude that the bulk of the warm molecular gas traced by H_2 rotational transitions lies at $T = 195 \text{ K}$. As the mid-J CO transitions arise from lower energy states than those producing the H_2 rotational lines we expect the mid-J CO emission to trace a cooler component, and therefore require $T_{\text{kin}} \leq 200 \text{ K}$. With these two upper limits the velocity gradient is effectively restricted to $dv/dr \approx 7 - 40 \text{ km s}^{-1} \text{ pc}^{-1}$, with corresponding limits to n_{H_2} and T_{kin} (Fig. 6.4).

To quantify the allowed ranges of the model parameters we adopt a Bayesian formalism and calculate a posterior probability density function for each parameter (for a detailed explanation of this method see [124]). We assume a prior expectation of uniform probability per logarithmic interval for each parameter, subject to the upper limits on dv/dr and T_{kin} imposed above. We find $n_{\text{H}_2} = 10^{3.8} - 10^{4.1} \text{ cm}^{-3}$, $T_{\text{kin}} = 80 - 200 \text{ K}$, and the thermal pressure is $P/k_B = (0.8 - 1.4) \times 10^6 \text{ cm}^{-3} \text{ K}$. The beam-averaged CO column density of this warm component is well constrained to be $N_{\text{CO}} = (1.7 - 2.2) \times 10^{18} \text{ cm}^{-2}$, giving an associated H_2 mass of $M_{\text{H}_2} = (1.2 - 1.6) \times 10^7 M_{\odot}$ in the central 180 pc. We take as our benchmark model the best fit solution obtained by fixing $dv/dr = 20 \text{ km s}^{-1} \text{ pc}^{-1}$ and plot it over the data in Figure 6.4.

6.3.3 Low Excitation Component

The residual $J = 2 \rightarrow 1$ and $J = 1 \rightarrow 0$ intensities from the benchmark model can be produced by a broad range of low excitation components with $T_{\text{kin}} \lesssim 40$ K and $n_{\text{H}_2} \sim 10^{2.4} - 10^{3.0} \text{ cm}^{-3}$, contributing a beam-averaged CO column density of $N_{\text{CO}} = (1.5 - 3.2) \times 10^{18} \text{ cm}^{-2}$. We therefore estimate the central 180 pc contain an H_2 mass of $M_{\text{H}_2} \approx 2.9 \times 10^7 M_{\odot}$, 35% – 60% of which is in a warm ($T_{\text{kin}} \sim 110$ K), dense ($n_{\text{H}_2} \sim 10^4 \text{ cm}^{-3}$) phase.

6.3.4 Comparison with Atomic Gas

The $158 \mu\text{m}$ [CII] fine-structure line emission and emission from other ionized and neutral gas tracers have been detected toward the central $45''$ of NGC 253 [11]. Based on a combined HII region and photodissociation region (PDR) model of the line and far-IR continuum flux, they estimate an atomic PDR mass of $M_{\text{HI}} = 2.4 \times 10^6 M_{\odot}$. Scaling from the $^{12}\text{CO } J = 1 \rightarrow 0$ morphology [88] we estimate half of the PDR emission arises from the central $15''$, giving $M_{\text{HI}} \approx 1.2 \times 10^6 M_{\odot}$ in the central 180 pc, a factor of ≈ 12 smaller than the warm molecular gas mass. PDR models generally predict comparable amounts of warm molecular and atomic components, so we conclude that the bulk of the warm molecular gas is not UV-heated gas associated with PDRs. In section 6.4 we explore alternative mechanisms for heating the molecular gas.

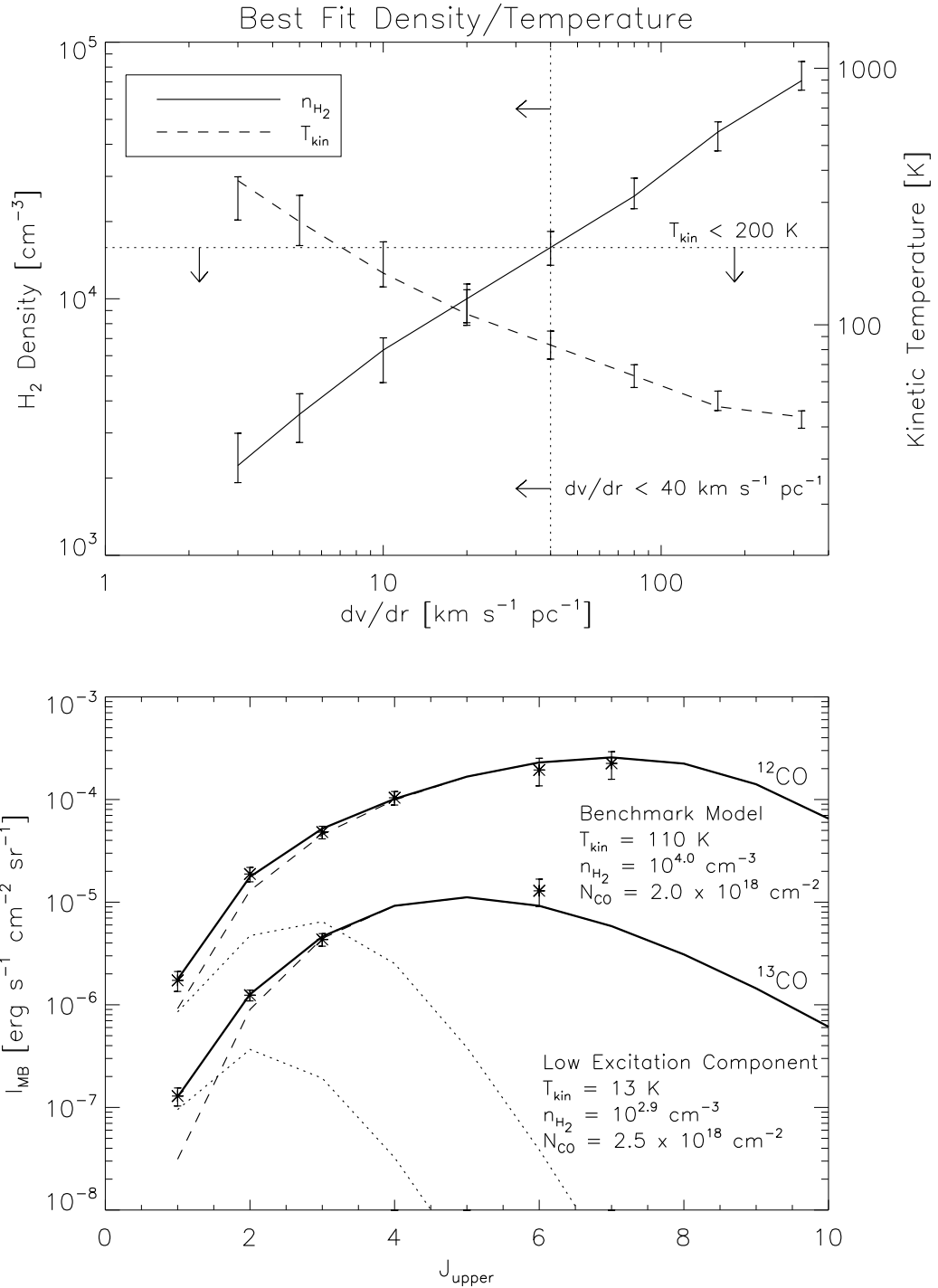


Figure 6.4: Results of LVG Analysis. *Top*: Best fit values of n_{H_2} (solid) and T_{kin} (dashed) as a function of dv/dr , with error bars showing $\pm 1\sigma$ range of the posterior probability density functions. The dotted lines show the upper limits to T_{kin} and dv/dr . *Bottom*: Integrated line intensities along with the benchmark high excitation model (dashed), a representative low excitation component (dotted), and the sum (solid).

6.4 Discussion: What Heats the Gas?

6.4.1 X-Rays

Due to their smaller cross sections, X-ray photons penetrate more deeply than UV photons into clouds and heat a larger volume of the molecular gas. In this section we consider whether an X-ray Dominated Region (XDR) can produce a warm molecular gas mass significantly in excess of the warm atomic gas mass.

The thermal and chemical structure of four model XDRs, with combinations of low or high density ($n_{\text{H}} = 10^{3.0}, 10^{5.5} \text{ cm}^{-3}$) and low or high incident X-ray flux ($F_{\text{X}} = 1.6, 160 \text{ ergs s}^{-1} \text{ cm}^{-2}$), are presented in [82]. For each model they plot the gas abundances and temperature as a function of depth into the cloud, from which we calculate the total column densities of warm C^+ and CO. The $158 \mu\text{m}$ [CII] transition used to trace the warm atomic component arises from a state 91 K above ground, so we include only C^+ warmer than 91 K. We include all CO warmer than 80 K, the minimum temperature allowed by our CO excitation analysis. The large observed ratio of $N_{\text{CO}}/N_{\text{C}^+} \approx 1.7$ (corresponding to $M_{\text{H}_2}/M_{\text{HI}} \approx 12$ as discussed in section 6.3.4) can only be produced by the high density ($n_{\text{H}} = 10^{5.5} \text{ cm}^{-3}$), high flux ($F_{\text{X}} = 160 \text{ ergs s}^{-1} \text{ cm}^{-2}$) model.

The model XDRs use densities which are an order of magnitude larger or smaller than the value of $n_{\text{H}} = 2n_{\text{H}_2} \sim 10^{4.3} \text{ cm}^{-3}$ indicated by our LVG analysis. Interpolating between the high density, high flux model and the lower density models, we estimate an XDR with $n_{\text{H}} = 10^{4.3} \text{ cm}^{-3}$ will match the observed $N_{\text{CO}}/N_{\text{C}^+}$ ratio only if $F_{\text{X}} \gtrsim 10 \text{ ergs s}^{-1} \text{ cm}^{-2}$. However, such an XDR will produce an [OI] $63 \mu\text{m}$ /[CII] $158 \mu\text{m}$ ratio more than ~ 20 times larger than ob-

served [11, 83], and consequently we rule out an XDR as a potential source of the mid-J CO emission.

6.4.2 Cosmic Rays

It is generally accepted that low energy cosmic rays control the thermal and chemical balance in the UV-shielded inner cores of Galactic molecular clouds [36]. The high supernovae rate in the nucleus of NGC 253 is estimated to result in a cosmic-ray ionization rate 750 times higher than in the Galactic plane, and these cosmic rays deposit $(5 - 18) \times 10^{-25}$ ergs s⁻¹ per H₂ molecule in the molecular gas [8]. By summing the integrated intensities predicted by our benchmark LVG model over all rotational transitions, we estimate a warm molecular gas mass of $M_{\text{H}_2} \approx 1.4 \times 10^7 M_{\odot}$ produces a CO luminosity of $L_{\text{CO}} \approx 1.6 \times 10^6 L_{\odot}$, corresponding to a specific cooling rate of $\approx 6.9 \times 10^{-25}$ ergs s⁻¹ per H₂ molecule. As this cooling rate matches the heating rate estimated by [8], we suggest an elevated cosmic-ray density resulting from the starburst may provide the origin of the warm molecular gas.

6.4.3 Shocks

The molecular gas in the center of NGC 253 shows evidence of shock-driven chemistry, including the large gas phase abundance of silicon [11, 29], and the general chemical similarity to shock-dominated molecular clouds in the Galactic center [79]. In this section we consider whether the mid-J CO emission may arise from shock-heated gas.

The emission from C-shocks is modeled by [22] and [21]. In addition to the rotational transitions of CO, the dominant coolants are the H₂ rovibrational transitions and the 63 μm [OI] fine-structure line, and we compare observations of these tracers with the model predictions in an attempt to constrain the possible shock parameters. The thermal emission from shock-heated gas in the central 15'' is estimated to produce an H₂ luminosity of $L_{\text{H}_2} = 1.3 \times 10^6 L_{\odot}$, summed over all infrared rovibrational transitions [23]. The [OI] 63 μm luminosity measured with a 42'' beam is $L_{[\text{OI}]} = 8.8 \times 10^6 L_{\odot}$ [11], and we estimate half of this emission arises from the central 15''. With a total CO luminosity of $L_{\text{CO}} \approx 1.6 \times 10^6 L_{\odot}$ we find that the $L_{\text{H}_2}/L_{\text{CO}} \approx 1$ and $L_{[\text{OI}]} / L_{\text{CO}} \approx 3$ ratios, as well as the general shape of the CO line SED, are reproduced for a low velocity ($v_{\text{shock}} \lesssim 8 \text{ km s}^{-1}$) shock incident on $n_{\text{H}} = 10^4 - 10^5 \text{ cm}^{-3}$ gas.

The molecular gas may be heated by shocks originating in the decay of supersonic turbulence, as is the case in the central 2 pc of the Galactic center [9]. Numerical simulations of magnetohydrodynamic (MHD) turbulence by [74] show that the conversion of dynamical to thermal energy in turbulent gas produces a specific luminosity of

$$\frac{L}{M} = 0.36 \left(\frac{v_{\text{rms}}}{8 \text{ km s}^{-1}} \right)^3 \left(\frac{0.1 \text{ pc}}{\Lambda} \right) \frac{L_{\odot}}{M_{\odot}}, \quad (6.1)$$

where v_{rms} and Λ are the characteristic velocity and length scale of the turbulence. The highest resolution molecular maps of NGC 253 utilize a $\sim 2''$ beam ($\sim 24 \text{ pc}$), so structure on sub-parsec scales remains unresolved. However, molecular gas in the Galactic center shows clumping on scales down to $\sim 0.1 \text{ pc}$ [9], so we adopt $\Lambda = 0.1 \text{ pc}$. For a total molecular gas mass of $M_{\text{H}_2} \approx 2.9 \times 10^7 M_{\odot}$ the luminosity to mass ratio observed in the primary shock coolants is $\approx 0.25 L_{\odot}/M_{\odot}$, comparable to the value obtained from the above equation by setting $v_{\text{rms}} = v_{\text{shock}} = 8 \text{ km s}^{-1}$. We conclude that in addition to an elevated density

of cosmic rays, the dissipation of turbulent energy through low velocity shocks can produce the warm molecular gas emitting in mid-J CO lines.

By keeping a large fraction of the molecular gas warm and therefore less susceptible to gravitational instability, cosmic rays and the decay of turbulence work to halt the starburst. As the cosmic rays are produced in supernovae and the turbulence may be driven by stellar feedback, we suggest the starburst in the nucleus of NGC 253 may be self-limiting.

CHAPTER 7

PHOTODISSOCIATED MOLECULAR GAS IN MIPS J142824.0+352619

In this chapter we present the first result from our program to observe far-IR (FIR) fine-structure line emission from high-redshift galaxies. We detected the ${}^2P_{3/2} \rightarrow {}^2P_{1/2}$ 158 μm [CII] transition in the $z = 1.325$ galaxy MIPS J142824.0+352619 (hereafter MIPS J1428) in March 2008 with ZEUS on the CSO. Prior to this observing run the entrance slit was enlarged to 10.8'', resulting in a main beam size of 13'' in the 350 μm window. This larger slit results in a modest improvement to our point source sensitivity while somewhat reducing the system resolving power. Calibration was achieved with observations of Saturn, as described in section 5.2.1. The total integration time was 135 minutes, with the line of sight transmission decreasing from 0.25 to 0.06 as the zenith transmission worsened and the source progressed to a lower elevation. This corresponds to an equivalent of 50 minutes of observation with 0.25 transmission. A linear baseline has been removed from the final spectrum, shown in Figure 7.1. The line is detected at 6.3σ significance with an integrated flux of $F_\nu\Delta\nu = 700 \text{ Jy km s}^{-1}$, which we compare with other observations in Table 7.1.

We begin our discussion with an introduction to MIPS J1428, which appears to be a starburst-dominated hyperluminous infrared galaxy ($L_{\text{FIR}} > 10^{13} L_\odot$), although the brightness may be aided by a gravitational lens. We then review our understanding of the emission of [CII] from actively star-forming galaxies: it arises from the photodissociated surfaces of molecular clouds exposed to elevated levels of far-UV (FUV) radiation. We employ a PDR model to the observed emission, and derive physical conditions similar to those found in nearby starburst nuclei. This suggests that MIPS J1428 may be undergoing a

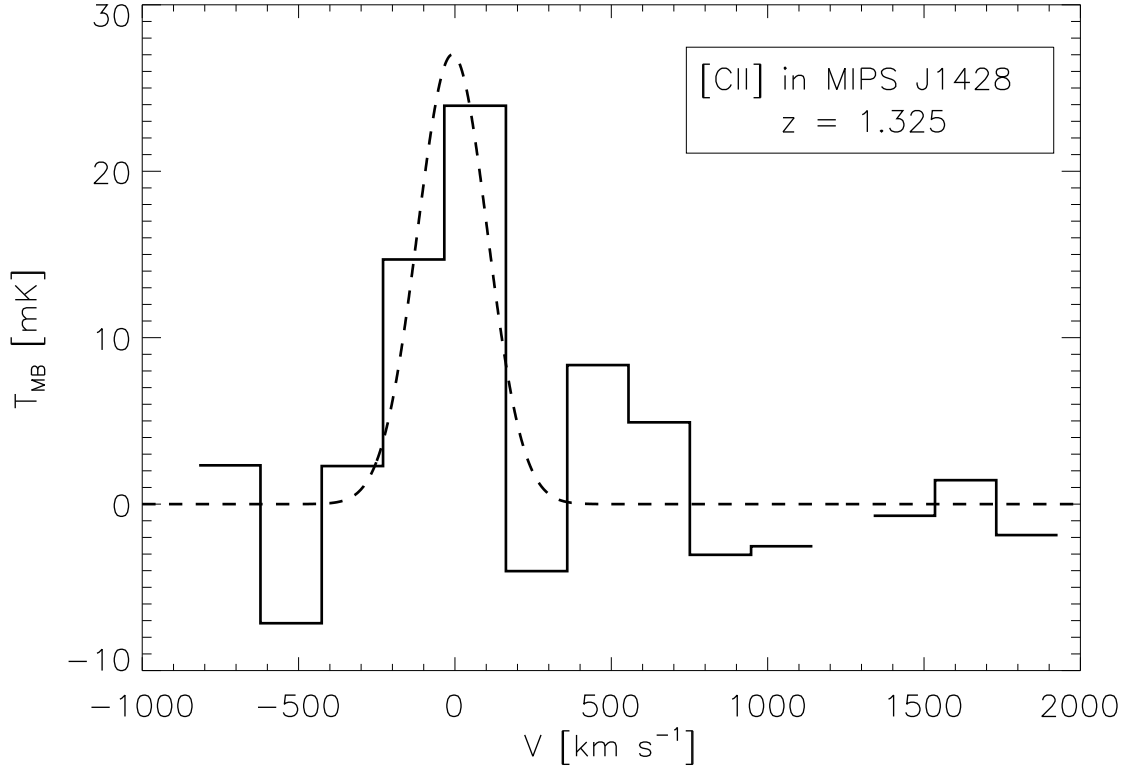


Figure 7.1: ZEUS/CSO spectrum of the $158 \mu\text{m}$ [CII] transition in MIPS J142824.0+352619. The velocity scale is referenced to $z = 1.325$, and the pixel at $v = 1250 \text{ km s}^{-1}$ has been removed due to the presence of a telluric absorption feature. The line is detected at 6.3σ significance.

moderate intensity galaxy-wide starburst, in contrast with the compact ULIRGs seen in the local Universe. The large star formation rate inferred from the FIR luminosity, coupled with the large molecular gas reservoir, make MIPS J1428 a good candidate to be the progenitor of a massive elliptical galaxy at $z = 0$.

7.1 Introduction

MIPS J1428 was identified as an extremely red object in a Spitzer/MIPS blank field survey, and with the help of ancillary optical data was selected as a likely candidate for an $L_{\text{FIR}} \sim 10^{13} L_{\odot}$ galaxy at $z \sim 1 - 2$ [7]. Spectroscopic follow-up with Spitzer/IRS [17] and in the near-IR measured the redshift of $z = 1.325$, and

Table 7.1: Spectral Line and Continuum Observations of MIPS J142824.0+352619

Transition	Flux [Jy km s ⁻¹]	L^a [L_\odot]	σ_L^a [L_\odot]	ref
[CII]	700	5.31×10^{10}	1.59×10^{10}	1
CO(2→1)	5.3	4.9×10^7	1.1×10^7	2
CO(3→2)	13.9	1.92×10^8	0.66×10^8	2
FIR Continuum	...	3.2×10^{13}	0.7×10^{13}	3
Luminosity Ratio		Ratio	σ_R	
$L_{\text{[CII]}}/L_{\text{FIR}}$		1.66×10^{-3}	0.62×10^{-3}	
$L_{\text{CO(3→2)}}/L_{\text{CO(2→1)}}$		3.93	1.62	
$L_{\text{[CII]}}/L_{\text{CO(2→1)}}$		1089	409	

Note. – [CII] flux is scaled by 70% before applying PDR models, to account for contributions from non-PDR origins. Luminosities are calculated using $\Omega_M = 0.27$, $\Omega_\Lambda = 0.73$, $H_0 = 71 \text{ km s}^{-1} \text{ Mpc}^{-1}$. References: (1) this work, (2) [55], (3) [7].

^aUncorrected for lensing

submillimeter continuum observations were obtained to fill out the SED. The FIR continuum emission is well modeled with a dust temperature of $T_d = 42.7$ K and a total luminosity of $L_{\text{FIR}} = 3.2 \times 10^{13} L_\odot$. This low dust temperature is similar to the mean value of 36 K found for a set of IRAS-selected star-forming galaxies in the local Universe, and is lower than the temperatures of $T > 60$ K generally attributed to AGN-heated dust [7, and references therein].

In addition to the low dust temperature, there are several other indications that the IR emission is powered by star formation rather than AGN activity. The mid-IR spectrum shows strong PAH emission, and the $6.2 \mu\text{m}$ feature has a large equivalent width similar to the value seen in starburst galaxies [17]. The high lower limit placed on the [Ne II] $12.8 \mu\text{m}$ /[Ne III] $15.6 \mu\text{m}$ ratio is also cited as evidence for a starburst as the energy source, as is the nondetection in hard X-ray emission [17]. Furthermore, the 20 cm radio flux is consistent with the FIR/radio correlation established for star-forming galaxies, and a 1.6

μm stellar bump expected from the photospheres of late-type giant stars is also apparent [7]. Combined, these facts suggest that MIPS J1428 is an extremely luminous starburst-powered system, with the $L_{\text{FIR}} = 3.2 \times 10^{13} L_{\odot}$ corresponding to a star formation rate of $5500 M_{\odot} \text{ yr}^{-1}$ [7].

The molecular gas content was measured interferometrically at $\sim 2'' - 4''$ resolution ($\sim 16 - 32$ kpc at $z = 1.325$) in CO(3 \rightarrow 2) and CO(2 \rightarrow 1) [55]. Both images show bright, unresolved emission with luminosities corresponding to a large gas mass of $M_{\text{H}_2} \sim 10^{11} M_{\odot}$. As gauged by the large value of either $L_{\text{FIR}}/M_{\text{H}_2}$ or the directly observed $L_{\text{FIR}}/L_{\text{CO}}$, MIPS J1428 is forming stars with high efficiency. In Figure 7.2 we compare the MIPS J1428 data with the $L_{\text{FIR}}/L'_{\text{CO}}{}^1$ ratio in a sample of normal spirals, local ULIRGs, and high-redshift galaxies primarily in the $z \sim 2 - 4$ range [108]. The star formation efficiency in MIPS J1428 is larger than that observed in local ULIRGs and somewhat smaller than the mean value in the high-redshift sources, although within the scatter of the distribution. Thus from the observations discussed to this point, it appears that MIPS J1428 is a hyperluminous infrared galaxy forming stars at a high rate, consistent with the large reservoir of molecular gas.

The large luminosities inferred from the observations are made uncertain, however, by the presence of a foreground gravitational lens. An optical spectrum of MIPS J1428 obtained by [7] shows the presence of absorption features attributed to an elliptical galaxy at $z = 1.034$, which may amplify the background source. A comparison of the optical image with radio and submillimeter interferometric images [54] suggests the source and lens are well aligned, with an

¹ L'_{CO} is the intrinsic velocity-integrated brightness temperature multiplied by the projected size of the telescope beam in the plane of the source, and is expressed in units of $\text{K km s}^{-1} \text{ pc}^2$. It is a measure of the line luminosity, but normalized such that different transitions with the same temperature-velocity product will have the same value of L'_{CO} .

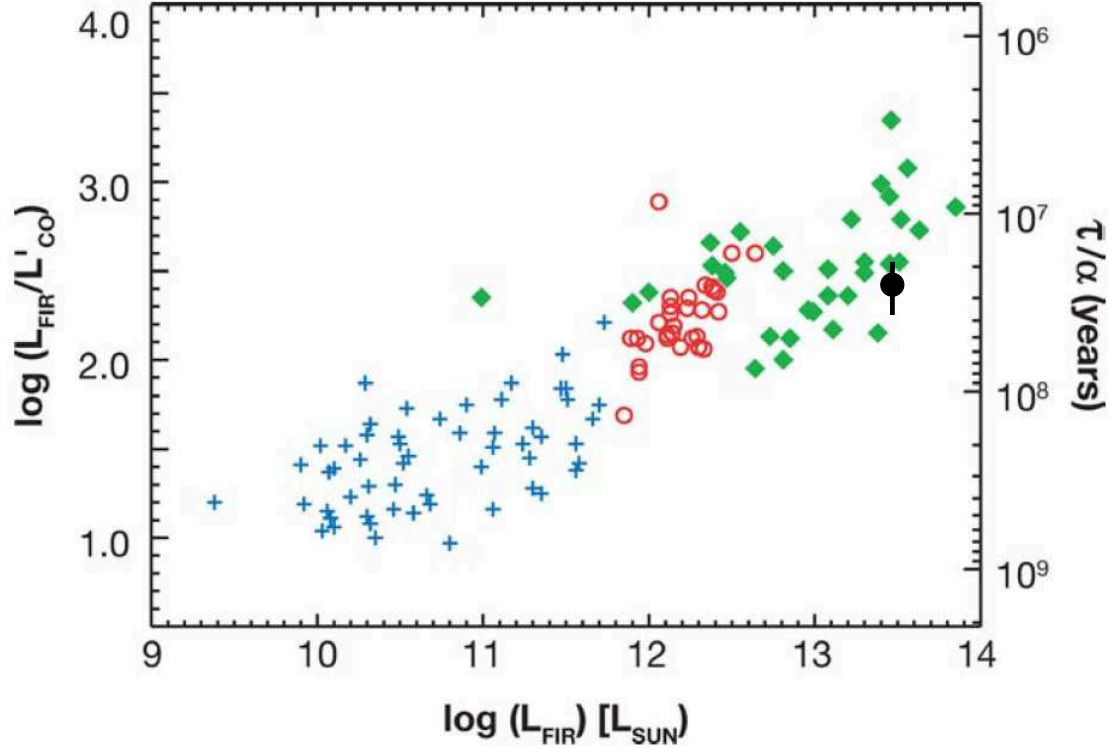


Figure 7.2: $L_{\text{FIR}}/L'_{\text{CO}}$ vs. L_{FIR} for normal spirals (*blue crosses*), local ULIRGs (*red circles*), and a population of high-redshift ($z \sim 2 - 4$) galaxies (*green diamonds*) from [108]. This ratio is an estimate of the star formation rate per unit molecular gas mass, and is often referred to as the star formation efficiency. The gas depletion timescale is τ , and $\alpha \approx 1$ is the H_2 mass (in M_\odot) per unit L'_{CO} (in $\text{K km s}^{-1} \text{pc}^2$). The data point for MIPS J1428 (uncorrected for lensing) (*black circle*) suggests a high star formation efficiency consistent with other sources of comparable luminosity [55].

Einstein radius of $\theta_E \lesssim 0.25''$. This angular scale corresponds to a linear size of $d \sim 2 \text{ kpc}$ at $z = 1.325$, and as this is on the order of the physical sizes of ULIRGs, it is argued that the lensing must be modest [7]. In a separate analysis, [7] compare the dust temperature and luminosity derived from their SED fit with an empirical correlation for submillimeter galaxies, which suggests that a system with $T_d = 43 \text{ K}$ should be ~ 10 times less luminous than directly inferred, indicating a lensing amplification of $\mu \sim 10$. An estimate of the lensing amplification is also obtained from the CO observations, in which [55] combine the CO fluxes with an assumed brightness temperature ($T_{\text{gas}} = T_d = 43 \text{ K}$) to estimate the im-

age size. This is combined with a simple lensing model and the 1.3'' upper limit to the CO(2→1) image size to estimate $\mu \lesssim 8$.

Thus, while the lensing amplification μ is poorly constrained, it is unlikely to be larger than 10 (although an alternative model is discussed in section 7.3.3). Throughout the rest of this chapter we explicitly include μ in all expressions of absolute quantity.

7.2 Results

7.2.1 [CII], CO, and the FIR Continuum: A Comparison to Starburst Galaxies

The first extragalactic observations of [CII] were made with the Kuiper Airborne Observatory (KAO) by [15, 109]. These initial two surveys reported [CII] detections from the nuclei of 20 gas-rich galaxies, with the $\approx 55''$ beam corresponding to linear sizes of 0.5 – 5 kpc for the 18 nearby systems. For all sources the $F_{\text{[CII]}}/F_{\text{FIR}}$ ratio was 0.1 – 1%, consistent with the predictions of the gas heating efficiency of PDRs. The spectral profiles of the [CII] and CO(1→0) lines were similar, as were the spatial distributions in the subset of galaxies mapped in both transitions. Combined, these correlations strongly supported the conclusion that the [CII] emission was produced by PDRs formed at the interface between giant molecular clouds and ionized gas.

Further insight is gained by examining the relative intensities of [CII], CO(1→0), and the FIR continuum. In Figure 7.3 the plot of $Y_{\text{[CII]}} = F_{\text{[CII]}}/F_{\text{FIR}}$

vs. $Y_{\text{CO}} = F_{\text{CO}(1\rightarrow 0)}/F_{\text{FIR}}$ for the galaxies in the combined sample [15, 109] is shown, along with a number of Galactic star-forming regions and molecular clouds. Overlaid are PDR model calculations, in which the incident FUV flux is parameterized as $F_{\text{UV}} = \chi_{\text{UV}} \times (2.0 \times 10^{-4} \text{ erg s}^{-1} \text{ cm}^{-2})$. The behavior of the theoretical models can be explained as follows. For low values of χ_{UV}/n the absorption of FUV flux is dominated by H_2 and C opacity, such that the C^+ column density and the gas temperature increase with increasing χ_{UV}/n , and $Y_{[\text{CII}]}$ increases as well. At larger values of χ_{UV}/n the absorption becomes dominated by dust grains, the C^+ column density is then only weakly dependent on χ_{UV}/n , and $Y_{[\text{CII}]}$ reaches a plateau. Further increasing χ_{UV}/n results in little additional [CII] emission, and for very large values of χ_{UV}/n , $Y_{[\text{CII}]}$ drops sharply. The CO intensity increases modestly with density but has very little dependence on χ_{UV} , and for a fixed n , Y_{CO} decreases monotonically with increasing χ_{UV} .

The positions of Galactic molecular clouds in this diagram indicate relatively weak FUV fields described by $\chi_{\text{UV}} \sim 10^2 - 10^3$, while the elevated star formation rates in Galactic star-forming regions produce values of $\chi_{\text{UV}} \sim 10^3 - 10^5$. The galaxy sample is divided into two populations based on the dust temperature, with galaxies showing $T_d \geq 40 \text{ K}$ classified as starburst galaxies. The normal spiral galaxies occupy the same region of phase space as the molecular clouds, while the starburst galaxies trend to higher values of $\chi_{\text{UV}} \sim 10^3 - 10^4$, mixing with the low- χ_{UV} population of Galactic star-forming regions. It is noteworthy that the starburst galaxies and the Galactic star-forming regions are tightly correlated about $F_{[\text{CII}]} / F_{\text{CO}(1\rightarrow 0)} = 4100$ (indicated by the dashed line in Fig. 7.3), while the same ratio in spiral galaxies and Galactic molecular clouds is ~ 3 times smaller. This rules out the possibility that a starburst galaxy might be a combination of intense, Orion-like star-forming regions and cold molecular clouds.

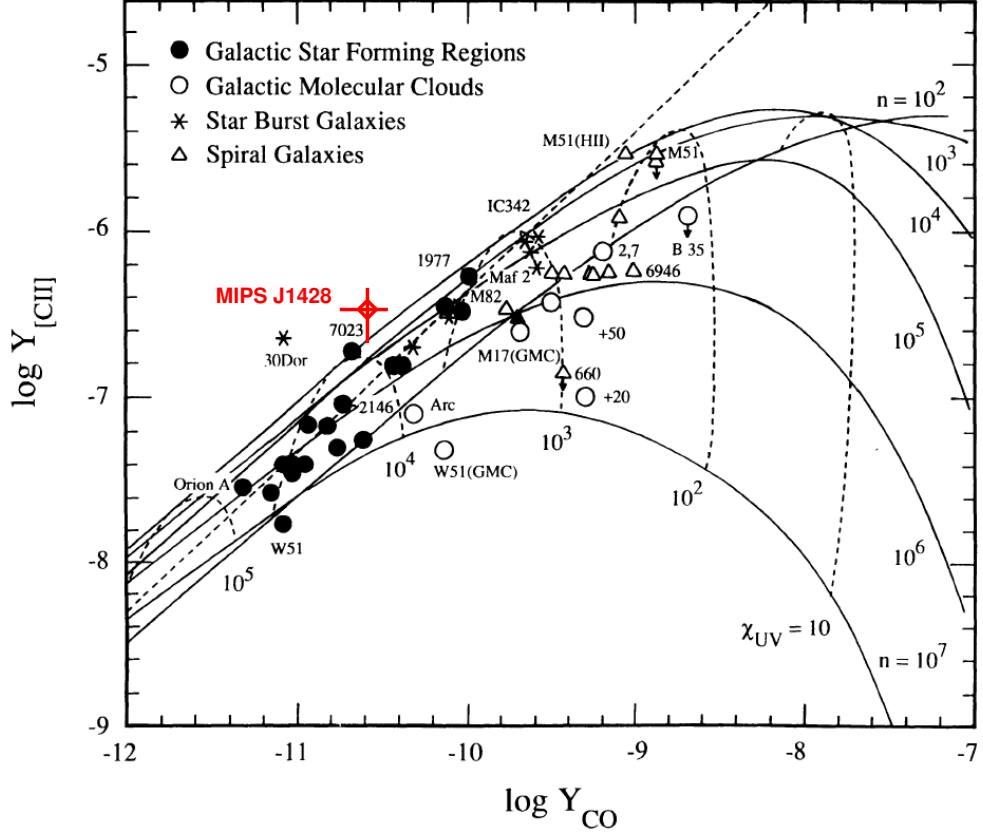


Figure 7.3: Plot of $Y_{\text{[CII]}}$ vs. Y_{CO} with PDR overlays from [109], with the data point for MIPS J1428 measured here. The MIPS J1428 point lies near the high- χ_{UV} end of the distribution of starburst galaxies.

The large $F_{\text{[CII]}}/F_{\text{CO(1}\rightarrow\text{0)}}$ ratio measured in the starburst sample corresponds to the photodissociated mass representing $\sim 30\% - 40\%$ of the total gas mass, compared with $\sim 3\% - 15\%$ for the normal spiral sample [109].

Also shown in Figure 7.3 is our measurement of MIPS J1428. The CO(1 \rightarrow 0) line has not been detected, but given that $L'_{\text{CO(3}\rightarrow\text{2)}}/L'_{\text{CO(2}\rightarrow\text{1)}} \sim 1$ [55] we assume the gas is thermalized, and estimate $L'_{\text{CO(1}\rightarrow\text{0)}} = L'_{\text{CO(2}\rightarrow\text{1)}}$. The data point falls near the high- χ_{UV} end of the distribution of starburst galaxies, albeit with a value of $F_{\text{[CII]}}/F_{\text{CO(1}\rightarrow\text{0)}} \approx 8700$ which is somewhat larger than the correlation established for the starburst galaxies and the Galactic star-forming regions. Nevertheless, this similarity suggests that in MIPS J1428, like in starburst nuclei, the

[CII], CO(1→0), and FIR continuum emission arises from PDRs illuminated by modest intensity FUV fields.

7.2.2 PDR Analysis

To obtain quantitative estimates of the physical conditions of the photodissociated molecular gas in MIPS J1428, we apply the PDR models of [60] to the observations of [CII], CO(3→2), CO(2→1), and the FIR continuum. We begin by using the relative strengths of these tracers to estimate the gas density n and the incident FUV flux, parameterized as $F_{\text{UV}} = G_0 \times (1.6 \times 10^{-4} \text{ erg s}^{-1} \text{ cm}^{-2})$. We then compare the $L_{[\text{CII}]}$ inferred from our observations with the $I_{[\text{CII}]}$ estimated from the model to derive the total PDR surface area, and then use $L_{[\text{CII}]}$ to estimate the atomic gas mass contained in the C^+ regions.

Line Ratios

Observations of CO(3→2) and CO(2→1) yield a line ratio of $L'_{\text{CO}(3\rightarrow 2)}/L'_{\text{CO}(2\rightarrow 1)} = 1.2 \pm 0.5$ [55]. The fact that this ratio is near unity suggests that the two lines have similar brightness temperatures, and therefore arise from high density, thermalized gas. An excitation analysis of this ratio finds $n_{\text{H}_2} \gtrsim 10^3 \text{ cm}^{-3}$, under the assumption that the gas temperature is comparable to the 43 K dust temperature [55]. In the PDR model this ratio is almost entirely a function of density for $G_0 \gtrsim 10$, and the lower limit of $L'_{\text{CO}(3\rightarrow 2)}/L'_{\text{CO}(2\rightarrow 1)} \gtrsim 0.7$ requires $n \gtrsim 10^{3.5} \text{ cm}^{-3}$ (Fig. 7.4).

Before comparing our [CII] observations to the models we must estimate

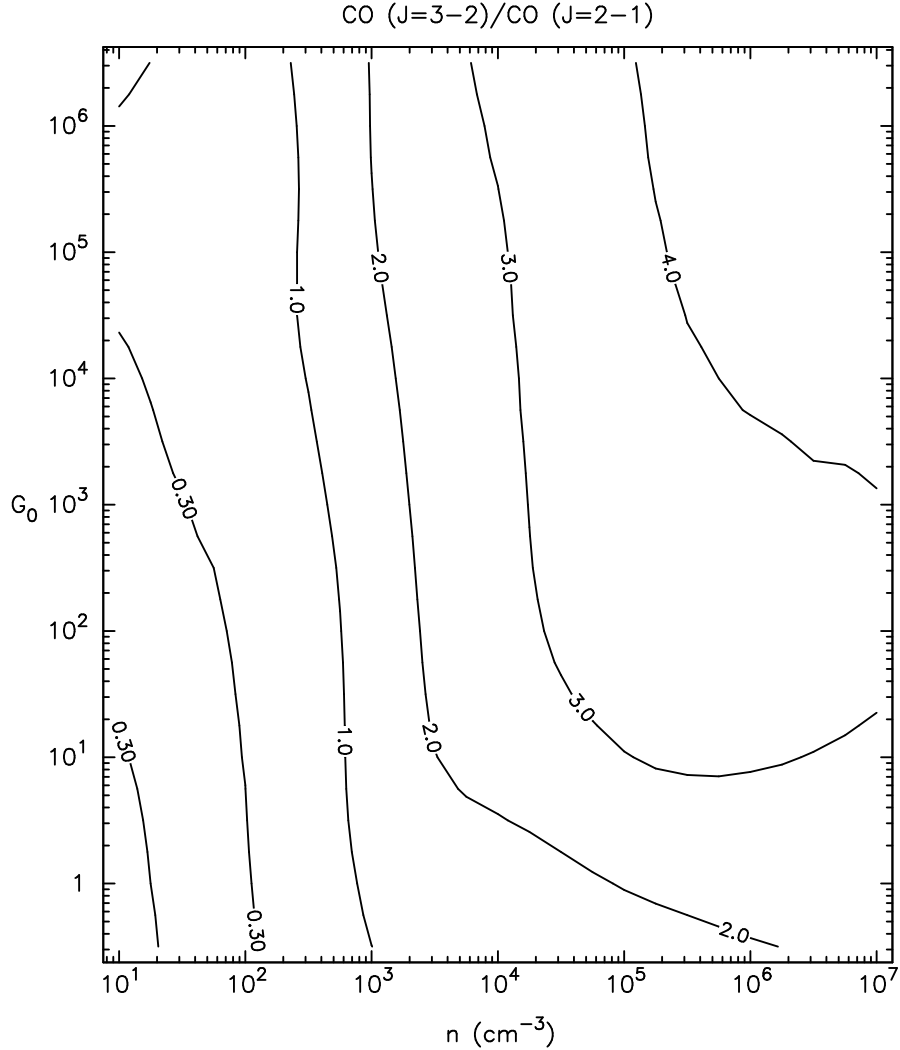


Figure 7.4: $F_{\text{CO}(3\rightarrow 2)}/F_{\text{CO}(2\rightarrow 1)}$ as a function of density, n , and FUV flux, G_0 , from the PDR models of [60]. The $\pm 1\sigma$ range of $L'_{\text{CO}(3\rightarrow 2)}/L'_{\text{CO}(2\rightarrow 1)} = 0.7 - 1.7$ corresponds to a flux ratio of $F_{\text{CO}(3\rightarrow 2)}/F_{\text{CO}(2\rightarrow 1)} = 2.3 - 5.5$, requiring $n \gtrsim 10^{3.5} \text{ cm}^{-3}$.

what fraction of the observed emission arises from non-PDR components. In principle, significant [CII] emission may be produced in compact HII regions and cold atomic clouds, but without knowing the physical conditions and mass fractions of these components in MIPS J1428 we cannot make any definite estimates of their contribution. Instead we turn to the local starburst templates NGC 253 and M82, in which joint modeling of the HII regions and PDRs show that the ionized gas produces no more than 30% of the galaxy-averaged [CII]

emission [11, 71]. [CII] emission from atomic clouds has also been shown to be negligible for the centers of galaxies [109], so here we estimate 70% of the [CII] emission from MIPS J1428 comes from the PDRs.

With this correction, the $L_{\text{[CII]}}/L_{\text{FIR}}$ ratio of the PDR component is $(1.16 \pm 0.43) \times 10^{-3}$. In the $n = 10^{3.5} - 10^{4.5} \text{ cm}^{-3}$ range this ratio is only weakly dependent on density, as long as $G_0 \gtrsim 10^2$ (Fig. 7.5). An increase in density will reduce the G_0/n ratio, which will increase the gas heating efficiency and the fraction of the bolometric emission contained in the cooling lines. However, the increased density will also shift the cooling budget toward the [OI] $63 \mu\text{m}$ transition, which has a high critical density of $n_{\text{crit}} \sim 9 \times 10^5 \text{ cm}^{-3}$, such that $L_{\text{[CII]}}/L_{\text{FIR}}$ is unchanged. For this density range the PDR models give $G_0 \approx 10^{2.5} - 10^{3.3}$, and while lower values of G_0 are possible for $n \gtrsim 10^{4.5} \text{ cm}^{-3}$, such models are ruled out by the $L_{\text{[CII]}}/L_{\text{CO}(2 \rightarrow 1)}$ ratio.

A third constraint may be obtained by considering the $L_{\text{[CII]}}/L_{\text{CO}(2 \rightarrow 1)}$ ratio, which becomes $L_{\text{[CII]}}/L_{\text{CO}(2 \rightarrow 1)} = 480 - 1050$ after reducing $L_{\text{[CII]}}$ by 30%. This constraint rules out solutions with $n \gtrsim 10^4 \text{ cm}^{-3}$, which underpredict $L_{\text{[CII]}}/L_{\text{CO}(2 \rightarrow 1)}$ unless G_0 is increased above $10^{3.3}$. We conclude that the relative strengths of the [CII], CO(3 \rightarrow 2), CO(2 \rightarrow 1), and FIR continuum emission may be reproduced by a PDR with $n \approx 10^{3.5} - 10^4 \text{ cm}^{-3}$ and $G_0 \approx 10^{2.5} - 10^{3.3}$, with a best fit at $n = 10^4 \text{ cm}^{-3}$ and $G_0 = 10^3$. These parameters are typical for starburst galaxies, which is to be expected, given the location of MIPS J1428 in Figure 7.3

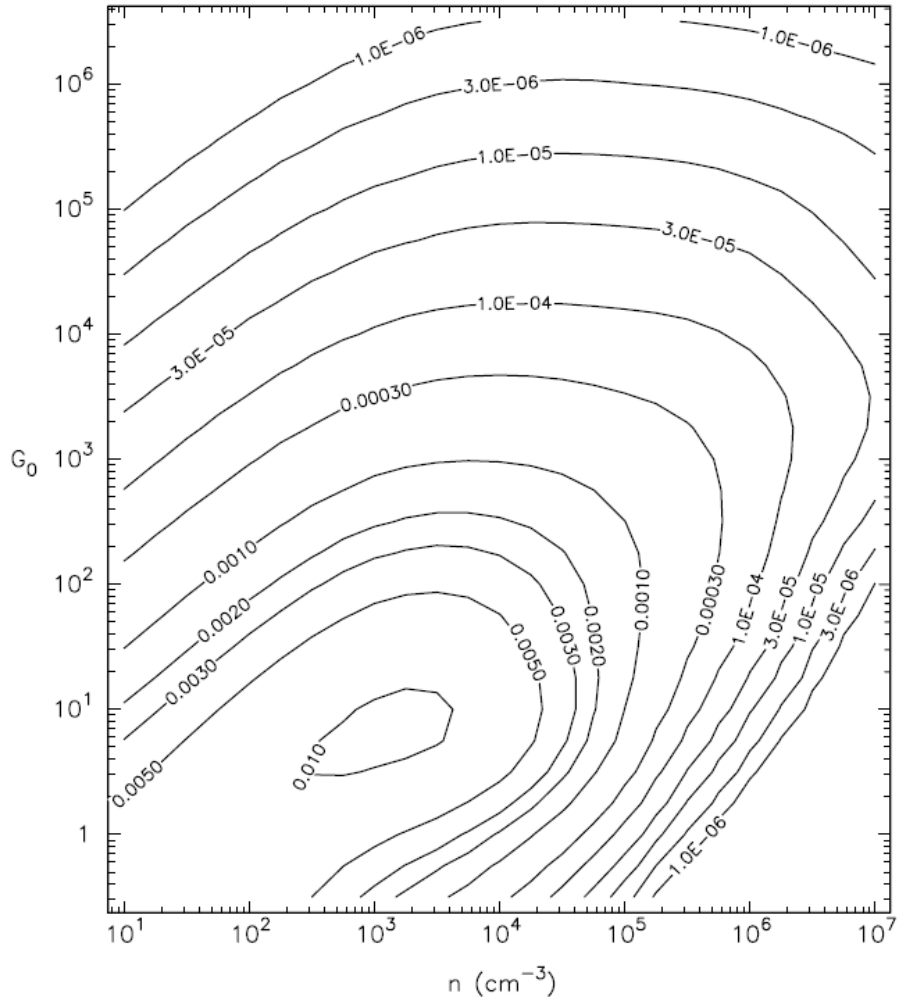


Figure 7.5: $F_{[\text{CII}]} / F_{\text{FIR}}$ as a function of density, n , and FUV flux, G_0 , from the PDR models of [60] and [73]. For $F_{[\text{CII}]} / F_{\text{FIR}} \approx 10^{-3}$ and $n = 10^{3.5} - 10^{4.5} \text{ cm}^{-3}$, this requires $G_0 \sim 10^3$.

Source Area

The emission from MIPS J1428 arises from a large number of individual PDRs distributed throughout the galaxy, and normalization of the models is achieved by specifying the total PDR surface area, A_{PDR} . For $n = 10^4 \text{ cm}^{-3}$ and $G_0 = 10^3$ the [CII] flux emerging from the surface of the PDR is $F_{[\text{CII}]} = (2\pi) \times (5 \times 10^{-4} \text{ ergs s}^{-1})$

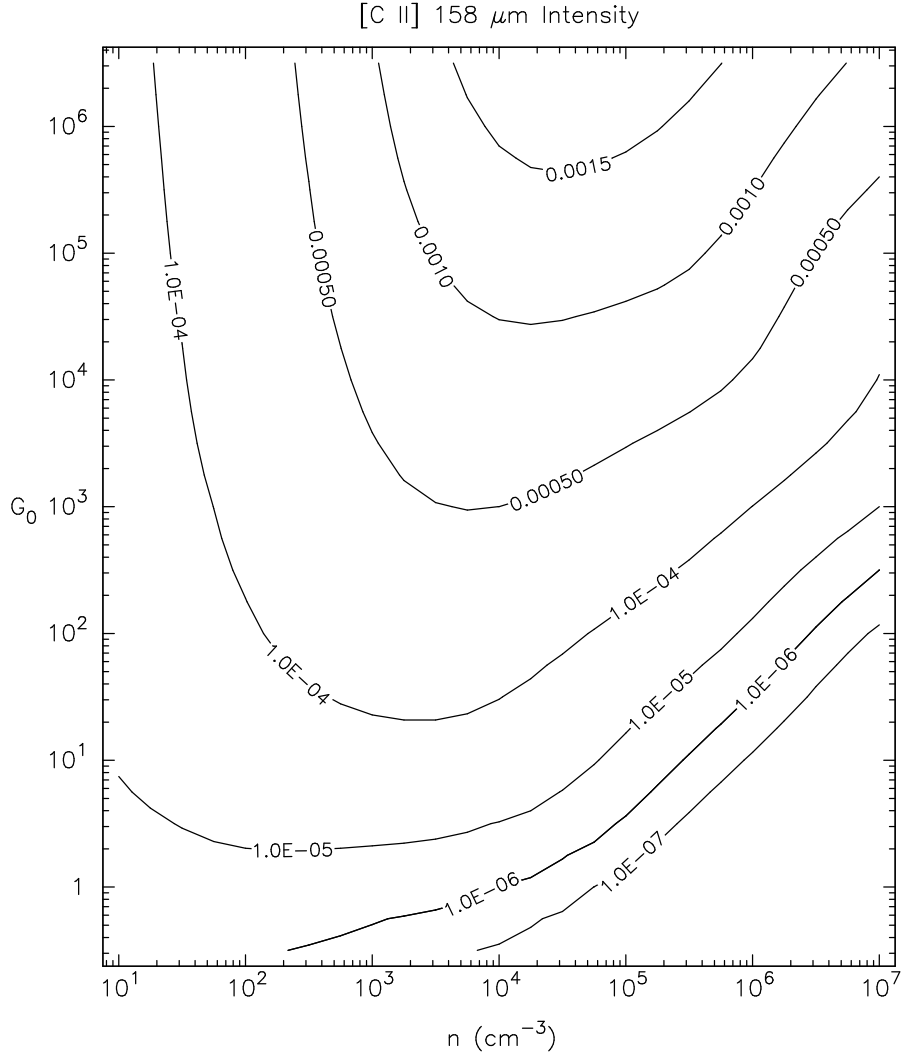


Figure 7.6: Absolute intensity of [CII] emitted normally from the surface of a PDR as a function of density, n , and FUV flux, G_0 , from [60].

cm^{-2}) (Fig. 7.6), and the total luminosity of the system is then $L_{[\text{CII}]} = A_{\text{PDR}} F_{[\text{CII}]}$. For the inferred PDR [CII] luminosity of $L_{[\text{CII}]} = 0.7 \times 5.3 \times 10^{10} \mu^{-1} L_{\odot}$ this gives a surface area of $A_{\text{PDR}} = (69 \text{ kpc})^2 \mu^{-1}$, where μ is the lensing amplification. While it is possible to use PDR models to construct a detailed picture of the distribution of matter in a galactic nucleus [126], we make no attempt to do so here. However, any such model would be constrained by this total surface area.

Atomic Gas Mass

An estimate of the atomic gas mass in MIPS J1428 may be obtained directly from the inferred [CII] luminosity. Assuming the [CII] emission is optically thin, and arises from hot ($T \gg 91$ K), dense ($n \gg n_{\text{crit}} = 3 \times 10^3 \text{ cm}^{-3}$) gas, the mass is directly proportional to the luminosity as

$$M_a = 1.16 \left(\frac{1.4 \times 10^{-4}}{X_{\text{C}^+}} \right) \left(\frac{L_{[\text{CII}]}}{L_\odot} \right) M_\odot, \quad (7.1)$$

where we use a C^+ abundance per hydrogen atom of $X_{\text{C}^+} = 1.4 \times 10^{-4}$ [100]. For the estimated $L_{[\text{CII}]} = 5.3 \times 10^{10} \mu^{-1} L_\odot$ this corresponds to $M_a = 6.2 \times 10^{10} \mu^{-1} M_\odot$.

The temperature at the surface of a PDR with $n = 10^4 \text{ cm}^{-3}$ and $G_0 = 10^3$ is $T_S = 300$ K, and it cools to $T \approx 100$ K at the C^+/C^0 interface [120, 60]. For a mean temperature of $T = 200$ K the high excitation limit invoked above doesn't strictly apply, and the mass estimate must be increased by a factor of 1.35. This correction is compensated by our previous estimate that only 70% of the [CII] emission originates in PDRs, such that the hydrogen mass in the C^+ region of the PDRs is $M_a = 5.8 \times 10^{10} \mu^{-1} M_\odot$. For comparison, the molecular mass estimated from the CO luminosity is $M_{\text{H}_2} \sim 10^{11} \mu^{-1} M_\odot$ [55], resulting in a PDR to H_2 mass ratio of ≈ 0.58 . We note that adopting the $X_{\text{C}^+} = 3 \times 10^{-4}$ abundance ratio used in [15, 109] would lead to a mass fraction of ≈ 0.29 , similar to the values found for starburst nuclei. Much like in nearby starburst nuclei, the PDR mass in MIPS J1428 is a significant fraction of the total molecular gas mass.

7.2.3 Comparison to M82: MIPS J1428 as a Scaled-Up Starburst Galaxy

In sections 7.2.1 and 7.2.2 we found that the physical parameters of the PDRs in MIPS J1428 are similar to those found in a typical starburst nucleus, and that the PDRs contain comparable fractions of the total gas mass in both systems. Given this similarity, we suggest MIPS J1428 may be modeled as a scaled-up version of the M82 starburst.

M82 is one of the nearest ($d \sim 3.5$ Mpc) and best studied starburst galaxies, and along with NGC 253 is often cited as a prototypical starburst. It is the brightest extragalactic source of IR continuum emission, producing a luminosity of $L_{IR} \sim 3 \times 10^{10} L_{\odot}$ [118]. The warm dust is distributed in a $\sim 400 \times 200$ pc nuclear region, with a ~ 125 pc site of elevated emission at either end. Like NGC 253, M82 contains a \sim kpc stellar bar which likely helps channel gas into the nucleus to feed the starburst, and was possibly formed by a recent interaction with M81. NGC 253 and M82 were two of the first galaxies for which multiple FIR lines were measured with the KAO and analyzed with PDR modeling [126, 11, 71, 60]. While the densities derived for both sources were $n \sim 10^4$ cm^{-3} , the FUV field strength of $G_0 \sim 2 \times 10^4$ estimated for NGC 253 was found to be larger than the value of $G_0 \sim 10^3$ estimated for M82 and above for MIPS J1428 [11, 71].

It is important to consider how the geometry of a starburst region controls the FUV flux incident on the PDRs. The first attempt to comprehensively examine how PDR models could be applied to extragalactic systems was [126], who considered two simple geometric models. The first model considered emission

from clouds distributed in close proximity to OB clusters, and the second model assumed the clouds were subject to an average interstellar radiation field produced by a random distribution of OB stars. For a fixed total stellar luminosity, PDRs in the second model would be characterized by a smaller value of G_0 . By comparing the value of G_0 derived from an examination of the emission ratios with the values predicted by these models, one could differentiate between the two geometries. For both NGC 253 and M82, it was established that the clouds were illuminated by an interstellar radiation field, rather than by nearby clusters [11, 71].

For such a geometry, the average incident flux scales as

$$G_{\text{AV}} \propto L_{\text{IR}} \frac{\lambda}{R^3} [1 - e^{-R/\lambda}], \quad (7.2)$$

where L_{IR} is the total (dust-processed) stellar luminosity, R is the radius of the region (assumed to be spherical), and λ is the mean cloud separation along a line of sight, which determines the most distant star which can contribute to the flux on a cloud. This parameter is determined by the size and number density of the clouds, and adopting $R = 200$ pc for M82 we estimate $\lambda = 90$ pc from the PDR solution in [71]. For $R/\lambda > 1$ the exponential term varies little with R , and can be ignored. To model MIPS J1428 as a scaled-up version of M82, with the same values of λ and G_{AV} , the factor of ~ 1000 greater luminosity then translates into a factor of ~ 10 increase in size, giving a spherical diameter of $D \approx 4\mu^{-1/3}$ kpc. We note that assuming $R/\lambda \ll 1$ would lead to an alternate estimate of $D \approx 12\mu^{-1/2}$ kpc.

The tightest constraint on the size of the IR-bright region of MIPS J1428 is provided by the CO(2 \rightarrow 1) interferometric image, which gives $\theta \lesssim 1.3''$, corresponding to $D \lesssim 11$ kpc assuming no lensing [55]. By inserting the estimated

FIR continuum luminosity and dust temperature into the Stefan-Boltzmann law for blackbody emission, [7] derive a spherical diameter of $D = 4.6\mu^{-1/2}$ kpc, similar to our estimate.

7.3 Discussion

7.3.1 [CII], CO, and the FIR Continuum: A Comparison with ULIRGs

KAO observations of [CII] and other FIR fine-structure lines made after the initial publications of [15, 109] reinforced the general conclusions of that earlier work: the emission from the nuclei of IR-bright galaxies was well modeled as arising from PDRs with $n \sim 10^3 - 10^4 \text{ cm}^{-3}$, $G_0 \sim 10^3 - 10^4$ [11, 70, 71]. With the launch of the Infrared Space Observatory (ISO) it became possible to extend these observations to fainter sources and assemble larger datasets. The largest sample of star-forming galaxies was published by [77], who detected [CII] and [OI] $63 \mu\text{m}$ emission from almost all of their 60 target sample, and important ionized gas cooling lines for many sources. The combination of [CII] and [OI] intensities proved a sensitive probe of the PDR conditions, especially for systems with elevated UV fields. It was discovered that galaxies with warmer dust temperatures (correlating with large luminosities) exhibited low $F_{\text{[CII]}}/F_{\text{FIR}}$ ratios, due to both an increase in the ratio G_0/n and in both of n and G_0 . For large values of G_0/n the dust grains become positively charged and photoelectric heating of the gas becomes less efficient, thereby reducing the cooling line intensities relative to the continuum emission. The increase in both n and G_0

shifts the cooling budget toward [OI], which also reduces $F_{\text{[CII]}}/F_{\text{FIR}}$.

The biggest surprise of the ISO [CII] observations came with the discovery that the $F_{\text{[CII]}}/F_{\text{FIR}}$ ratio in ULIRGs is a factor of ~ 7 times weaker than in normal star-forming galaxies [73]. Figure 7.7 shows a sample of the ISO and pre-ISO [CII] observations along with CO and FIR intensities and PDR model overlays. The extended sample of normal star-forming galaxies occupies the same region as the KAO sample of [15, 109], at the low-FUV end of the distribution of Galactic PDRs and HII regions. The ULIRGs, however, have somewhat smaller values of Y_{CO} , and much smaller values of $Y_{\text{[CII]}}$.

This [CII] deficit in ULIRGs has been much discussed in the literature since its discovery [76, 77, 72, 30, 73]. One possible solution is that it is simply a continuation of the decreasing $F_{\text{[CII]}}/F_{\text{FIR}}$ ratio detected by [77] at the high luminosity end of the normal galaxy sample. This idea is reinforced by the location of the ULIRGs with respect to the PDR model overlays in Figure 7.7, which indicate both higher n and higher G_0 . The [CII] deficit could then be a combination of reduced gas cooling efficiency and a shift in the cooling importance to [OI]. A second potential explanation is that the ULIRGs contain a population of PDRs with more moderate values of n and G_0 , but in addition contain an extra source of FIR continuum which dominates over the PDR component. This could occur if the bulk of the UV luminosity is processed by warm dust mixed with HII regions, rather than in PDRs [73].

Regardless of the origins of the [CII] deficit in ULIRGs, it is remarkable that the hyperluminous galaxy MIPS J1428 does not exhibit such a deficit, but instead produces a large $F_{\text{[CII]}}/F_{\text{FIR}}$ ratio more closely resembling that of a low luminosity starburst galaxy. This suggests that ULIRGs may not be as useful as

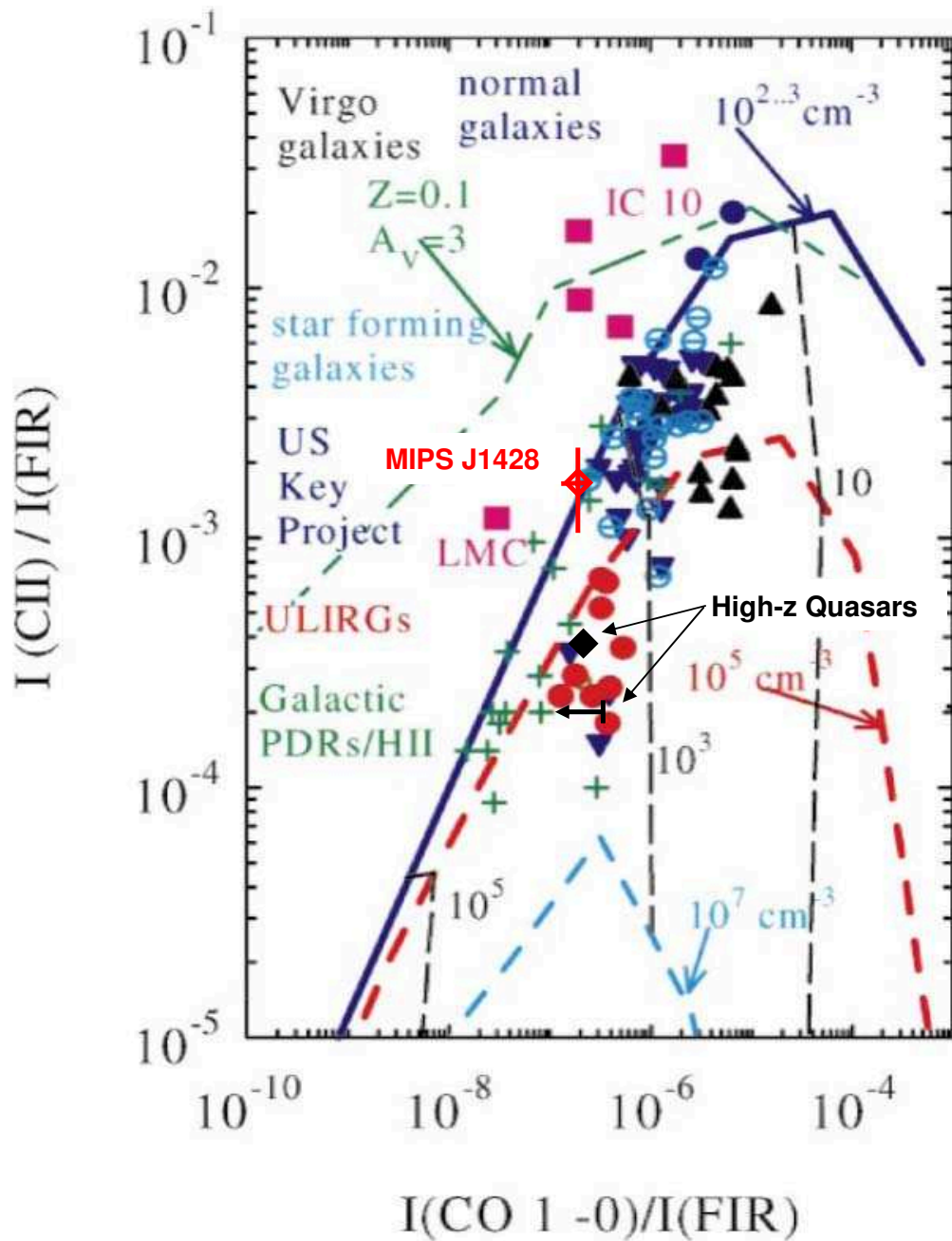


Figure 7.7: Plot of Y_{CII} vs. Y_{CO} showing data from KAO and ISO observations with PDR overlays from [30]. Also shown is the data point for MIPS J1428 measured here, and the two high-redshift quasars from [75, 56].

templates for high-redshift star formation as might be expected.

7.3.2 [CII] Emission from High-Redshift Quasars

In addition to the local galaxies observed with the KAO and ISO, weak [CII] emission has been detected from a pair of high-redshift quasars, which are included in Figure 7.7. The first of these is the $z = 6.42$ quasar SDSS J114816.64+525150.3, which at the time of the [CII] detection was the most distant known QSO [75]. The host galaxy has a FIR luminosity of $L_{\text{FIR}} \approx 2 \times 10^{13} L_{\odot}$ and an estimated gas mass of a few $\times 10^{10} M_{\odot}$, so while it's not known how much of the luminosity arises from star formation, the galaxy has a sufficiently large gas reservoir to fuel a major burst. The [CII] luminosity corresponds to $L_{\text{[CII]}}/L_{\text{FIR}} = 2 \times 10^{-4}$, and a PDR model of the [CII], FIR continuum, CO(1 \rightarrow 0), CO(3 \rightarrow 2), CO(6 \rightarrow 5), and CO(7 \rightarrow 6) emission yields a satisfactory fit for $n = 10^5 \text{ cm}^{-3}$ and $G_0 = 10^{3.8}$.

A second detection of [CII] emission has been obtained from the northern component of the $z = 4.7$ quasar BR 1202-0725 [56]. This system is a two component merger, with BR 1202S an optically visible QSO and BR 1202N also likely hosting an obscured AGN. Both components are detected in dust continuum and in CO, with estimated gas masses larger than $10^{10} M_{\odot}$. Emission from [CII] is detected from BR 1202N with $L_{\text{[CII]}}/L_{\text{FIR}} = 3.8 \times 10^{-4}$, and an upper limit corresponding to $L_{\text{[CII]}}/L_{\text{FIR}} \leq 2.8 \times 10^{-4}$ is reported for BR 1202S.

Figure 7.8 shows the $L_{\text{[CII]}}/L_{\text{FIR}}$ ratio as a function of L_{FIR} for the normal galaxy sample, the ULIRGs, the two high-redshift quasars, and MIPS J1428. The two high-redshift detections represent an apparent extension of the [CII] deficit

observed in local ULIRGs to higher redshifts and higher luminosities, making MIPS J1428 seem an outlier. However, the potential presence of an energetically dominant AGN illuminating the gas with a hard, intense UV field provides a natural explanation for the weak [CII] in the two quasars. The intense UV flux incident on the PDR will result in charged grains and a reduction in the gas heating efficiency, as has been proposed for the ULIRGs (section 7.3.1). A particularly hard field will result in a large fraction of the UV emission absorbed by dust in the HII regions, thereby diluting the $L_{\text{[CII]}}/L_{\text{FIR}}$ ratio of the PDRs [73]. More generally, the two quasars were selected as optically visible QSOs, whereas MIPS J1428 was selected as a FIR-luminous galaxy. Based on this selection criteria alone, MIPS J1428 should be considered as belonging to a separate population, of which it is currently the only member.

An upper limit of $L_{\text{[CII]}}/L_{\text{FIR}} < 4 \times 10^{-3}$ was reported for the $z = 4.93$ galaxy GI CL1358+62, which has an apparent luminosity of $L_{\text{FIR}} = 2.8 \times 10^{12} L_{\odot}$, but is likely lensed by a factor $\mu \sim 5 - 11$ [78]. This source is not a quasar, and is therefore more likely to be a high-redshift analog of either the ULIRGs or MIPS J1428. However, the achieved upper limit does not place a meaningful constraint on $L_{\text{[CII]}}/L_{\text{FIR}}$.

7.3.3 An Extended Starburst?

We previously used the similarity between the estimated PDR parameters of MIPS J1428 and M82 to argue that MIPS J1428 may resemble a scaled-up starburst nucleus, with a size of $D = 4\mu^{-1/3}$ kpc. This size estimate is similar to the value of $D = 4.6\mu^{-1/2}$ kpc estimated by [7] through a comparison of the in-

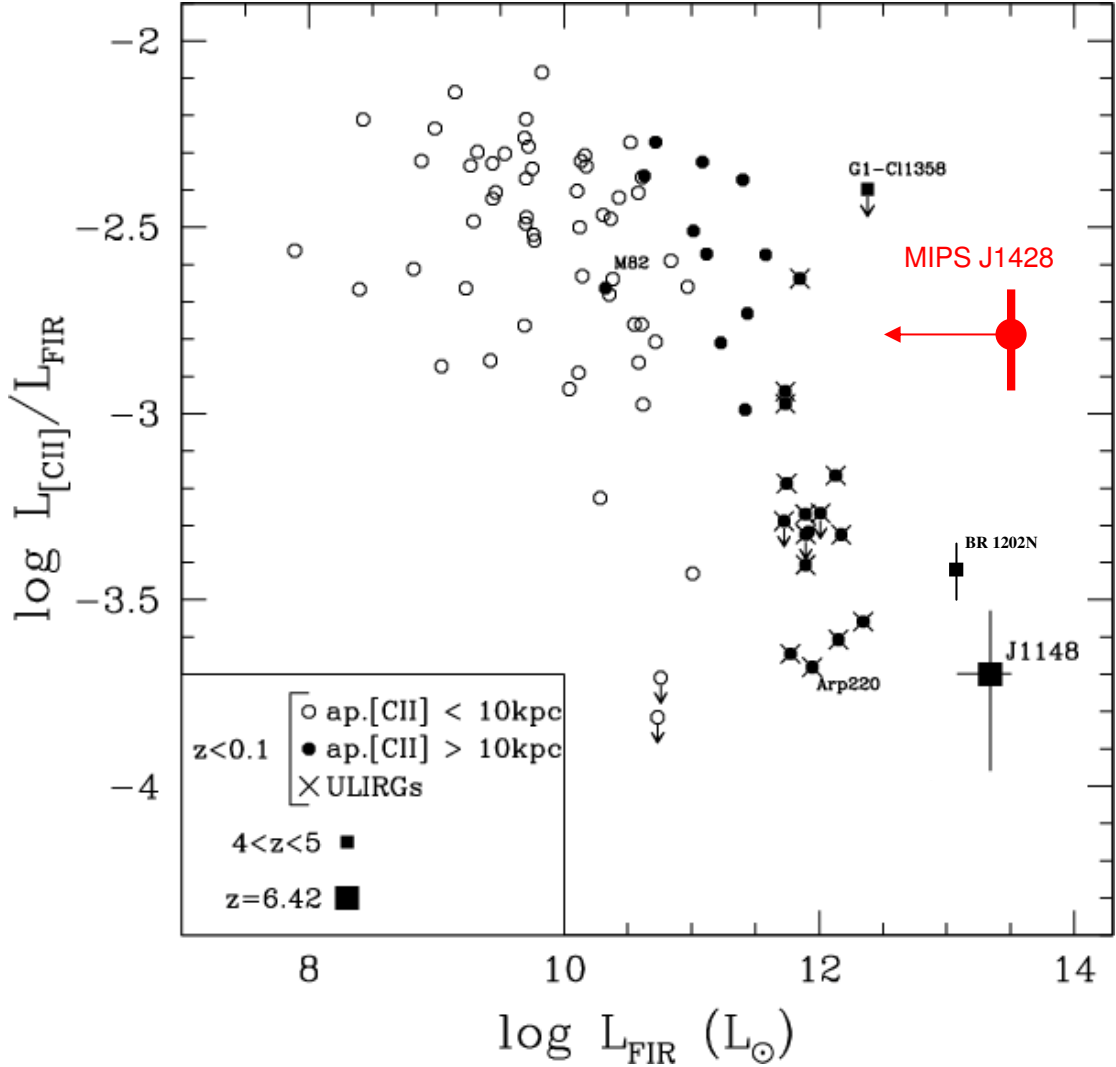


Figure 7.8: Plot of $L_{\text{[CII]}}/L_{\text{FIR}}$ vs. L_{FIR} for normal galaxies, ULIRGs, and high-redshift sources adapted from [75]. The ZEUS detection of MIPS J1428 is included, with an arrow correcting for a lensing amplification of $\mu = 10$.

ferred L_{FIR} and the dust temperature. This would be in sharp contrast to local ULIRGs, however, in which most of the emission traced by CO interferometry is contained within the central kpc [20].

There is good evidence, however, that submillimeter galaxies are extended. High resolution 1.4 GHz images of a sample of 12 SMGs have shown that 8 are extended on a scale of ~ 10 kpc [14]. Under the assumption that the ra-

dio images are tracking the FIR morphology through the FIR/radio correlation, this implies that the SMGs are powered by star formation extended over ~ 40 kpc². The estimated star formation surface densities in these sources is $\sim 45 M_{\odot} \text{ yr}^{-1} \text{ kpc}^{-2}$, similar to the upper limit for surface densities in starburst galaxies, which suggests similar physical mechanisms may be operating at small scales in the two populations [14, and references therein]. A more recent radio-mapping project has qualitatively confirmed this result by measuring a mean width of ~ 5 kpc in a sample of 12 SMGs, and noting that these galaxies are larger than randomly selected radio sources with comparable brightness [5]. These authors suggest that the SMGs may be witnessed at an earlier, more extended merger stage than the compact, late stage merging ULIRGs.

An imaging survey of CO emission from 8 SMGs has confirmed that many of these sources are extended on the scale of a few kpc, with a size distribution statistically consistent with the radio studies [116]. However, these latter authors note that although the SMGs are larger than the ULIRGs, the two populations are found to have similar surface brightnesses, which would contradict the low star formation surface density model suggested by [14]. Regardless, it is clear that the SMG population is extended on kpc scales, consistent with our estimate for MIPS J1428.

While MIPS J1428 remains unresolved in the IR and at longer wavelengths, an H α image has been obtained by [115]. The emission is extended over $\sim 1''$ (~ 8 kpc at $z = 1.325$), and an upper limit of 125 km s^{-1} is placed on the velocity shift across the image. One interpretation of this image is that the H α emission traces star formation over ~ 8 kpc, and the low velocity shift across the source implies that any disk rotation or relative velocity between merging components

is in the plane of observation. There are, however, two uncertainties in this conclusion. The first complexity lies in the fact that the $H\alpha$ image may be distorted by the foreground lens, which is visible in the form of extended near-IR continuum emission within $\sim 0.5''$ of the $H\alpha$ centroid. This would suggest that the $\sim 1''$ image may be a magnification of a smaller intrinsic source size, an idea which is supported by the lack of a systematic velocity shift across the image. However, the $H\alpha$ image is elongated along the line connecting the lens to the image, whereas one would expect the lensing to elongate the image in the orthogonal direction. It is also possible that the source is multiply imaged on one side of the lens, in which case a third image is expected to be produced on the opposite side. The nondetection of this image would potentially yield a lensing amplification of $\mu \gg 10$, but this is inconsistent with the modest values of μ estimated by [7, 55].

A second difficulty in interpreting the $H\alpha$ emission is the presence of large extinction, which generally results in $H\alpha$ -derived star formation rates a factor of $\sim 10 - 100$ times smaller than rates derived from FIR luminosities [115]. The $H\alpha$ and CO images of a selection of 6 SMGs are compared in [116], where it is found that the $H\alpha$ emission tends to be more spatially extended. The optical continuum maps tend to be more extended as well, and [116] suggest that the optical emission traces lower extinction, lower luminosity emission outside of the more obscured, and energetically dominant, centralized starburst. Thus while it is tempting to conclude that the extended $H\alpha$ emission is consistent with our previous suggestion of an extended starburst, the star formation traced by this $H\alpha$ image may not be a significant fraction of the system activity.

7.3.4 Evolution of High-Redshift Galaxies: Connection to Massive Ellipticals

Since their discovery, it was recognized that SMGs were good candidates to be the progenitors of massive elliptical galaxies [69, 103, 115]. Elliptical galaxies dominate the local optical luminosity function at $L > L^*$, and can have stellar masses as large as $M_{\text{star}} \sim 10^{11} - 10^{12} M_{\odot}$. There is also good evidence that massive ellipticals were already established in clusters at $z > 1$, implying that their stellar populations were formed quickly and early [6].

If the lensing amplification of MIPS J1428 is not too large, the molecular gas mass $M_{\text{H}_2} \sim 10^{11} \mu^{-1} M_{\odot}$ is similar to the typical SMG value, and suggests that MIPS J1428 is capable of forming the large stellar mass found in a massive elliptical. At the current star formation rate of $5500 \mu^{-1} M_{\odot} \text{ yr}^{-1}$ [7] this gas will be depleted in only $\tau \sim 20$ Myr, consistent with the rapid stellar production implied by the existence of massive evolved systems at $z \sim 1$. We conclude that MIPS J1428, like the general SMG population, is a likely progenitor of a massive elliptical galaxy.

7.4 Conclusions

We have detected the ${}^2\text{P}_{3/2} \rightarrow {}^2\text{P}_{1/2}$ $158 \mu\text{m}$ [CII] transition in the $z = 1.325$ hyperluminous infrared galaxy MIPS J142824.0+352619. This is the first detection of a far-infrared fine-structure line in a high-redshift source with no evidence of a powerful AGN. By all indications, the luminosity of this galaxy is powered by star formation, a conclusion which is further reinforced by the brightness

of the [CII] line. We combine the [CII], CO(3→2), CO(2→1), and far-infrared continuum intensities to probe the physical conditions of the gas, and find that the density and ambient UV field strength are similar to those found in starburst nuclei, but markedly different from those found in local ULIRGs. We suggest that MIPS J142824.0+352619 may resemble a scaled-up starburst nucleus, with vigorous star formation occurring over a scale of ~ 4 kpc. This length scale is consistent with a previous estimate of the source size, and consistent with the extended nature of the general submillimeter galaxy population. MIPS J142824.0+352619 has a massive reservoir of molecular gas that it is rapidly converting to stars, and like the rest of the submillimeter galaxy population, it appears to be evolving toward a massive elliptical galaxy. While the brightness of this galaxy may be amplified by a gravitational lens, it is unlikely that the lensing amplification is large enough to change this picture.

APPENDIX A
LARGE VELOCITY GRADIENT

In this section we describe our procedure for calculating model sets of CO line intensities with the help of the large velocity gradient (LVG) approximation. The following notation is that of [98], and our radiative transfer calculations closely follow [12, 33].

We begin by considering a two-level system with level populations n_1 and n_2 . In the optically thin limit the equation of statistical equilibrium is

$$\frac{dn_2}{dt} = -n_2 (C_{21} + A_{21}) + n_1 C_{12} = 0, \quad (\text{A.1})$$

where C_{12} and C_{21} are the collisional excitation and de-excitation rates, and A_{21} is the Einstein rate coefficient for spontaneous emission. For collisions with H_2 the rates are written as $C_{ij} = n_{\text{H}_2} \gamma_{ij}$, where the coefficients γ_{ij} are functions of the gas kinetic temperature. The CO- H_2 collisional coefficients have been calculated for a range of temperatures by [27], such that for a choice of n_{H_2} and T_{kin} , equation A.1 can be solved to give the level population ratio n_2/n_1 .

The situation becomes more complicated when we consider stimulated emission and absorption, in which case the equation of statistical equilibrium becomes

$$\frac{dn_2}{dt} = -n_2 (C_{21} + A_{21} + B_{21} \bar{J}) + n_1 (C_{12} + B_{12} \bar{J}) = 0, \quad (\text{A.2})$$

where \bar{J} is the mean intensity J_ν averaged over the local line profile function $\phi(\nu)$, and B_{21} and B_{12} are the Einstein rate coefficients for stimulated emission and absorption. Due to the large optical depths of the CO transitions, stimulated processes play a significant role in the determination of the level populations. The equations of statistical equilibrium and radiative transfer are there-

fore strongly coupled, and to proceed we make a key simplifying approximation.

One of the major difficulties of this problem is that it is nonlocal; the mean intensity J_ν at any location in the source is a function of the emission produced by gas all over the rest of the source. If we assume a large velocity gradient is present, however, then \bar{J} becomes purely a local quantity. Specifically, if the local thermal or turbulent velocity width of the gas is δ_ν and the velocity gradient is dv/dr , then an emitted photon can only interact with the gas within a distance $l \sim \delta_\nu/(dv/dr)$ of the site of its emission. For a sufficiently large velocity gradient we can assume the gas is homogeneous over this length. For a spherically symmetric source with a radial velocity field $\mathbf{v}(\mathbf{r}) = v(r)\mathbf{e}_r$, we can relate \bar{J} to the local gas excitation by writing

$$\bar{J} = (1 - \beta) S_\nu, \quad (\text{A.3})$$

where β is the photon escape probability, the source function is

$$S_\nu = \frac{2h\nu^3}{c^2} \left(\frac{g_2 n_1}{g_1 n_2} - 1 \right)^{-1}, \quad (\text{A.4})$$

and g_2 and g_1 are the statistical weights. Equation A.2 then reduces to the simplified form

$$\frac{dn_2}{dt} = -n_2 (C_{21} + \beta A_{21}) + n_1 C_{12} = 0. \quad (\text{A.5})$$

Generalizing equation A.5 to a multi-level system we find

$$\frac{dn_i}{dt} = \sum_{j \neq i} [-n_i C_{ij} + n_j C_{ji}] - n_i \beta_{i,i-1} A_{i,i-1} + n_{i+1} \beta_{i+1,i} A_{i+1,i} = 0, \quad (\text{A.6})$$

where for CO only transitions with $j - i = \pm 1$ have nonzero A_{ij} coefficients. With the further assumption that dv/dr is constant through the source, β_{ij} reduces to the simple function

$$\beta_{i+1,i} = \frac{1 - e^{-\tau_{i+1,i}}}{\tau_{i+1,i}}, \quad (\text{A.7})$$

where

$$\tau_{i+1,i} = \frac{A_{i+1,i}}{8\pi} \frac{c^3}{v_{i+1,i}^3} \frac{n_{\text{tot}}}{dv/dr} \frac{n_i g_{i+1}}{n_{\text{tot}} g_i} \left(1 - \frac{g_i n_{i+1}}{g_{i+1} n_i} \right). \quad (\text{A.8})$$

To solve the equations of statistical equilibrium we begin by guessing values of $\beta_{i+1,i}$ and inserting them into equations A.6. For a choice of n_{H_2} and T_{kin} the collisional rates are determined and equations A.6 reduce to a system of linear equations, which can be solved to give the fractional level populations n_i/n_{tot} . For a choice of $n_{\text{tot}}/(dv/dr)$ the set of $\tau_{i+1,i}$ is then calculated from equations A.8 and $\beta_{i+1,i}$ are calculated from equations A.7. The results are compared with the guessed values of $\beta_{i+1,i}$ and a new set of guess values is chosen, and we iterate in this fashion until a self-consistent solution is reached. We start this process in the optically thin limit by initializing $\beta_{i+1,i} = 1$.

The LVG approach allows us to model sources with nontrivial density and temperatures profiles, but for the sake of simplicity we assume our cloud is a homogeneous sphere. We further assume that the telescope beam contains a large number of these small, identical clouds, such that the measured integrated intensity is simply

$$I_{i+1,i} = \frac{h\nu_{i+1,i}}{4\pi} \frac{n_{i+1}}{n_{\text{tot}}} A_{i+1,i} \beta_{i+1,i} N_{\text{tot}}, \quad (\text{A.9})$$

where N_{tot} is the beam-averaged column density.

We also include the effects of the cosmic microwave background by setting

$$\beta_{i+1,i} \rightarrow \beta_{i+1,i} \left[1 - \frac{(n_i g_{i+1}/n_{i+1} g_i) - 1}{\left(\exp(h\nu_{i+1,i}/kT_{\text{bg}}) - 1 \right)} \right] \quad (\text{A.10})$$

in equations A.6 and A.9, with $T_{\text{bg}} = 2.73$ K.

BIBLIOGRAPHY

- [1] J. W. M. Baars. The measurement of large antennas with cosmic radio sources. *IEEE Transactions on Antennas and Propagation*, 21:461–474, 1973.
- [2] E. Bayet, M. Gerin, T. G. Phillips, and A. Contursi. The submillimeter C and CO lines in Henize 2-10 and NGC 253. *A&A*, 427:45–59, November 2004.
- [3] E. Bayet, M. Gerin, T. G. Phillips, and A. Contursi. A survey of submillimeter C and CO lines in nearby galaxies. *A&A*, 460:467–485, December 2006.
- [4] D. J. Benford, T. R. Hunter, and T. G. Phillips. Noise Equivalent Powers of Background Limited Thermal Detectors at Submillimeter Wavelengths. *International Journal of Infrared and Millimeter Waves*, 19:7–+, 1998.
- [5] A. D. Biggs and R. J. Ivison. High-resolution radio observations of submillimetre galaxies. *MNRAS*, 385:893–904, April 2008.
- [6] J. P. Blakeslee, M. Franx, M. Postman, P. Rosati, B. P. Holden, G. D. Illingworth, H. C. Ford, N. J. G. Cross, C. Gronwall, N. Benítez, R. J. Bouwens, T. J. Broadhurst, M. Clampin, R. Demarco, D. A. Golimowski, G. F. Hartig, L. Infante, A. R. Martel, G. K. Miley, F. Menanteau, G. R. Meurer, M. Sirlanni, and R. L. White. Advanced Camera for Surveys Photometry of the Cluster RDCS 1252.9-2927: The Color-Magnitude Relation at $z = 1.24$. *ApJ*, 596:L143–L146, October 2003.
- [7] C. Borys, A. W. Blain, A. Dey, E. Le Floch, B. T. Jannuzi, V. Barnard, C. Bian, M. Brodwin, K. Menéndez-Delmestre, D. Thompson, K. Brand, M. J. I. Brown, C. D. Dowell, P. Eisenhardt, D. Farrah, D. T. Frayer, J. Higdon, S. Higdon, T. Phillips, B. T. Soifer, D. Stern, and D. Weedman. MIPS J142824.0+352619: A Hyperluminous Starburst Galaxy at $z = 1.325$. *ApJ*, 636:134–139, January 2006.
- [8] C. M. Bradford, T. Nikola, G. J. Stacey, A. D. Bolatto, J. M. Jackson, M. L. Savage, J. A. Davidson, and S. J. Higdon. CO ($J=7\rightarrow 6$) Observations of NGC 253: Cosmic-Ray-heated Warm Molecular Gas. *ApJ*, 586:891–901, April 2003.
- [9] C. M. Bradford, G. J. Stacey, T. Nikola, A. D. Bolatto, J. M. Jackson, M. L. Savage, and J. A. Davidson. Warm Molecular Gas Traced with CO $J =$

- 7→6 in the Galaxy's Central 2 Parsecs: Dynamical Heating of the Circumnuclear Disk. *ApJ*, 623:866–876, April 2005.
- [10] C. M. Bradford, G. J. Stacey, M. R. Swain, T. Nikola, A. D. Bolatto, J. M. Jackson, M. L. Savage, J. A. Davidson, and P. A. R. Ade. SPIFI: a direct-detection imaging spectrometer for submillimeter wavelengths. *Appl. Opt.*, 41:2561–2574, May 2002.
- [11] P. Carral, D. J. Hollenbach, S. D. Lord, S. W. J. Colgan, M. R. Haas, R. H. Rubin, and E. F. Erickson. The interstellar medium in the starburst regions of NGC 253 and NGC 3256. *ApJ*, 423:223–236, March 1994.
- [12] J. I. Castor. Spectral line formation in Wolf-Rayet envelopes. *MNRAS*, 149:111–127, 1970.
- [13] S. C. Chapman, A. W. Blain, I. Smail, and R. J. Ivison. A Redshift Survey of the Submillimeter Galaxy Population. *ApJ*, 622:772–796, April 2005.
- [14] S. C. Chapman, I. Smail, R. Windhorst, T. Muxlow, and R. J. Ivison. Evidence for Extended, Obscured Starbursts in Submillimeter Galaxies. *ApJ*, 611:732–738, August 2004.
- [15] M. K. Crawford, R. Genzel, C. H. Townes, and D. M. Watson. Far-infrared spectroscopy of galaxies - The 158 micron C(+) line and the energy balance of molecular clouds. *ApJ*, 291:755–771, April 1985.
- [16] M. Das, K. R. Anantharamaiah, and M. S. Yun. The Central Velocity Field in NGC 253: Possible Indication of a Bar. *ApJ*, 549:896–905, March 2001.
- [17] V. Desai, L. Armus, B. T. Soifer, D. W. Weedman, S. Higdon, C. Bian, C. Borys, H. W. W. Spoon, V. Charmandaris, K. Brand, M. J. I. Brown, A. Dey, J. Higdon, J. Houck, B. T. Jannuzi, E. Le Floc'h, M. L. N. Ashby, and H. A. Smith. IRS Spectra of Two Ultraluminous Infrared Galaxies at $z = 1.3$. *ApJ*, 641:133–139, April 2006.
- [18] H. Dole, G. Lagache, J.-L. Puget, K. I. Caputi, N. Fernández-Conde, E. Le Floc'h, C. Papovich, P. G. Pérez-González, G. H. Rieke, and M. Blaylock. The cosmic infrared background resolved by Spitzer. Contributions of mid-infrared galaxies to the far-infrared background. *A&A*, 451:417–429, May 2006.
- [19] C. D. Dowell, C. A. Allen, R. S. Babu, M. M. Freund, M. Gardner,

- J. Groseth, M. D. Jhabvala, A. Kovacs, D. C. Lis, S. H. Moseley, Jr., T. G. Phillips, R. F. Silverberg, G. M. Voellmer, and H. Yoshida. SHARC II: a Caltech submillimeter observatory facility camera with 384 pixels. In T. G. Phillips and J. Zmuidzinas, editors, *Society of Photo-Optical Instrumentation Engineers (SPIE) Conference Series*, volume 4855 of *Society of Photo-Optical Instrumentation Engineers (SPIE) Conference Series*, pages 73–87, February 2003.
- [20] D. Downes and P. M. Solomon. Rotating Nuclear Rings and Extreme Starbursts in Ultraluminous Galaxies. *ApJ*, 507:615–654, November 1998.
- [21] B. T. Draine and W. G. Roberge. CO line emission from shock waves in molecular clouds. *ApJ*, 282:491–507, July 1984.
- [22] B. T. Draine, W. G. Roberge, and A. Dalgarno. Magnetohydrodynamic shock waves in molecular clouds. *ApJ*, 264:485–507, January 1983.
- [23] C. W. Engelbracht, M. J. Rieke, G. H. Rieke, D. M. Kelly, and J. M. Achtermann. The Nuclear Starburst in NGC 253. *ApJ*, 505:639–658, October 1998.
- [24] D. Farrah, J. Bernard-Salas, H. W. W. Spoon, B. T. Soifer, L. Armus, B. Brandl, V. Charmandaris, V. Desai, S. Higdon, D. Devost, and J. Houck. High-Resolution Mid-Infrared Spectroscopy of Ultraluminous Infrared Galaxies. *ApJ*, 667:149–169, September 2007.
- [25] D. J. Fixsen, C. L. Bennett, and J. C. Mather. COBE Far Infrared Absolute Spectrophotometer Observations of Galactic Lines. *ApJ*, 526:207–214, November 1999.
- [26] D. J. Fixsen, E. Dwek, J. C. Mather, C. L. Bennett, and R. A. Shafer. The Spectrum of the Extragalactic Far-Infrared Background from the COBE FIRAS Observations. *ApJ*, 508:123–128, November 1998.
- [27] D. R. Flower. The rotational excitation of CO by H₂. *Journal of Physics B Atomic Molecular Physics*, 34:2731–2738, July 2001.
- [28] M. A. Frerking, W. D. Langer, and R. W. Wilson. The relationship between carbon monoxide abundance and visual extinction in interstellar clouds. *ApJ*, 262:590–605, November 1982.
- [29] S. García-Burillo, J. Martín-Pintado, A. Fuente, and R. Neri. Large-scale

- shocks in the starburst galaxy NGC 253. Interferometer mapping of a ~ 600 pc SiO/H¹³CO⁺ circumnuclear disk. *A&A*, 355:499–511, March 2000.
- [30] R. Genzel and C. J. Cesarsky. Extragalactic Results from the Infrared Space Observatory. *ARA&A*, 38:761–814, 2000.
- [31] R. Genzel, D. Lutz, E. Sturm, E. Egami, D. Kunze, A. F. M. Moorwood, D. Rigopoulou, H. W. W. Spoon, A. Sternberg, L. E. Tacconi-Garman, L. Tacconi, and N. Thatte. What Powers Ultraluminous IRAS Galaxies? *ApJ*, 498:579–+, May 1998.
- [32] M. Gerin and T. G. Phillips. Atomic Carbon in Galaxies. *ApJ*, 537:644–653, July 2000.
- [33] P. Goldreich and J. Kwan. Molecular Clouds. *ApJ*, 189:441–454, May 1974.
- [34] P. F. Goldsmith. Molecular Depletion and Thermal Balance in Dark Cloud Cores. *ApJ*, 557:736–746, August 2001.
- [35] P. F. Goldsmith. Radio Telescopes and Measurements at Radio Wavelengths. In S. Stanimirovic, D. Altschuler, P. Goldsmith, and C. Salter, editors, *Single-Dish Radio Astronomy: Techniques and Applications*, volume 278 of *Astronomical Society of the Pacific Conference Series*, pages 45–79, December 2002.
- [36] P. F. Goldsmith and W. D. Langer. Molecular cooling and thermal balance of dense interstellar clouds. *ApJ*, 222:881–895, June 1978.
- [37] L. I. Goray. Rigorous integral method in application to computing diffraction on relief gratings working in wavelength range from microwaves to x ray. In T. Jansson and N. C. Gallagher, editors, *Society of Photo-Optical Instrumentation Engineers (SPIE) Conference Series*, volume 2532 of *Society of Photo-Optical Instrumentation Engineers (SPIE) Conference Series*, pages 427–433, September 1995.
- [38] T. R. Greve, F. Bertoldi, I. Smail, R. Neri, S. C. Chapman, A. W. Blain, R. J. Ivison, R. Genzel, A. Omont, P. Cox, L. Tacconi, and J.-P. Kneib. An interferometric CO survey of luminous submillimetre galaxies. *MNRAS*, 359:1165–1183, May 2005.
- [39] R. Güsten, A. Baryshev, A. Bell, A. Belloche, U. Graf, H. Hafok, S. Heyminck, S. Hochgürtel, C. E. Honingh, K. Jacobs, C. Kasemann,

- B. Klein, T. Klein, A. Korn, I. Krämer, C. Leinz, A. Lundgren, K. M. Menten, K. Meyer, D. Muders, F. Pavec, D. Rabanus, F. Schäfer, P. Schilke, G. Schneider, J. Stutzki, G. Wieching, A. Wunsch, and F. Wyrowski. Submillimeter heterodyne arrays for APEX. In *Society of Photo-Optical Instrumentation Engineers (SPIE) Conference Series*, volume 7020 of *Presented at the Society of Photo-Optical Instrumentation Engineers (SPIE) Conference*, August 2008.
- [40] R. Güsten, S. D. Philipp, A. Weiß, and B. Klein. CO(4-3) and CO(7-6) maps of the nucleus of NGC 253. *A&A*, 454:L115–L118, August 2006.
- [41] S. Hailey-Dunsheath, T. Nikola, G. J. Stacey, T. E. Oberst, S. C. Parshley, C. M. Bradford, P. A. R. Ade, and C. E. Tucker. Detection of the ^{13}CO J=6→5 transition in the Starburst Galaxy NGC 253. *ApJ*, 689:L109–L112, December 2008.
- [42] S. I. Han, R. Almy, E. Apodaca, W. Bergmann, S. Deiker, A. Lesser, D. McCammon, K. Rawlins, R. L. Kelley, S. H. Moseley, F. S. Porter, C. K. Stahle, and A. E. Szymkowiak. Intrinsic 1/f noise in doped silicon thermistors for cryogenic calorimeters. In O. H. Siegmund and M. A. Gummin, editors, *Society of Photo-Optical Instrumentation Engineers (SPIE) Conference Series*, volume 3445 of *Presented at the Society of Photo-Optical Instrumentation Engineers (SPIE) Conference*, pages 640–644, November 1998.
- [43] A. I. Harris, J. Stutzki, U. U. Graf, A. P. G. Russell, R. Genzel, and R. E. Hills. First observations of the CO J = 6-5 transition in starburst galaxies. *ApJ*, 382:L75–L79, December 1991.
- [44] A. Harrison, C. Henkel, and A. Russell. Carbon monoxide in the starburst of NGC 253 revisited. *MNRAS*, 303:157–172, February 1999.
- [45] A. Harrison, P. Puxley, A. Russell, and P. Brand. Atomic carbon and carbon monoxide in the nuclear region of NGC 253. *MNRAS*, 277:413–422, November 1995.
- [46] T. M. Heckman. Starbursts: Lessons for the Origin and Evolution of Galaxies and the Intergalactic Medium. In C. E. Woodward, J. M. Shull, and H. A. Thronson, Jr., editors, *Origins*, volume 148 of *Astronomical Society of the Pacific Conference Series*, pages 127–+, 1998.
- [47] C. Henkel, R. Mauersberger, T. Wiklind, S. Huettemeister, C. Lemme, and T. J. Millar. Dense gas in nearby galaxies. VI - A large C-12/C-13 ratio in a nuclear starburst environment. *A&A*, 268:L17–L20, February 1993.

- [48] T. Herter, D. L. Shupe, and G. E. Gull. KEGS: A 5-40 micron Spectrometer for the KAO. In R. E. Stencel, editor, *Proceedings of the 1991 North American Workshop on Infrared Spectroscopy*, pages 35–+, June 1991.
- [49] R. H. Hildebrand, R. F. Loewenstein, D. A. Harper, G. S. Orton, J. Keene, and S. E. Whitcomb. Far-infrared and submillimeter brightness temperatures of the giant planets. *Icarus*, 64:64–87, October 1985.
- [50] W. S. Holland, E. I. Robson, W. K. Gear, C. R. Cunningham, J. F. Lightfoot, T. Jenness, R. J. Ivison, J. A. Stevens, P. A. R. Ade, M. J. Griffin, W. D. Duncan, J. A. Murphy, and D. A. Naylor. SCUBA: a common-user submillimetre camera operating on the James Clerk Maxwell Telescope. *MNRAS*, 303:659–672, March 1999.
- [51] D. J. Hollenbach and A. G. G. M. Tielens. Dense Photodissociation Regions (PDRs). *ARA&A*, 35:179–216, 1997.
- [52] P. Horowitz and W. Hill. *The art of electronics*. Cambridge, New York: Cambridge University Press, —c1989, 2nd ed., 1989.
- [53] J. E. Howe, D. T. Jaffe, E. N. Grossman, W. F. Wall, J. G. Mangum, and G. J. Stacey. Extended CO(7-6) emission from warm gas in Orion. *ApJ*, 410:179–187, June 1993.
- [54] D. Iono, A. B. Peck, A. Pope, C. Borys, D. Scott, D. J. Wilner, M. Gurwell, P. T. P. Ho, M. S. Yun, S. Matsushita, G. R. Petitpas, J. S. Dunlop, M. Elvis, A. Blain, and E. Le Floch. Interferometric 890 μm Images of High-Redshift Submillimeter Galaxies. *ApJ*, 640:L1–L4, March 2006.
- [55] D. Iono, Y. Tamura, K. Nakanishi, R. Kawabe, K. Kohno, T. Okuda, K. Yamada, B. Hatsukade, and M. Sameshima. CO (3-2) and CO (2-1) Detections in a $z = 1.3$ Hyper-Luminous Starburst Galaxy. *PASJ*, 58:957–963, December 2006.
- [56] D. Iono, M. S. Yun, M. Elvis, A. B. Peck, P. T. P. Ho, D. J. Wilner, T. R. Hunter, S. Matsushita, and S. Muller. A Detection of [C II] Line Emission in the $z = 4.7$ QSO BR 1202-0725. *ApJ*, 645:L97–L100, July 2006.
- [57] F. P. Israel and F. Baas. Neutral atomic carbon in centers of galaxies. *A&A*, 383:82–90, January 2002.

- [58] F. P. Israel, G. J. White, and F. Baas. CO and CI maps of the starburst galaxy NGC 253. *A&A*, 302:343–+, October 1995.
- [59] D. T. Jaffe, R. Genzel, A. I. Harris, J. B. Lugten, G. J. Stacey, and J. Stutzki. Strong, spatially extended CO 7-6 emission from luminous cloud cores - W51 and DR 21. *ApJ*, 344:265–276, September 1989.
- [60] M. J. Kaufman, M. G. Wolfire, D. J. Hollenbach, and M. L. Luhman. Far-Infrared and Submillimeter Emission from Galactic and Extragalactic Photodissociation Regions. *ApJ*, 527:795–813, December 1999.
- [61] J. Keene, G. A. Blake, T. G. Phillips, P. J. Huggins, and C. A. Beichman. The abundance of atomic carbon near the ionization fronts in M17 and S140. *ApJ*, 299:967–980, December 1985.
- [62] J. Keene, D. C. Lis, T. G. Phillips, and P. Schilke. Photon-dominated regions: Observations of [C I] and CO. In E. F. van Dishoeck, editor, *Molecules in Astrophysics: Probes & Processes*, volume 178 of *IAU Symposium*, pages 129–+, 1996.
- [63] B. Klein, S. D. Philipp, I. Krämer, C. Kasemann, R. Güsten, and K. M. Menten. The APEX digital Fast Fourier Transform Spectrometer. *A&A*, 454:L29–L32, August 2006.
- [64] J. W. Kooi, J. Kawamura, J. Chen, G. Chattopadhyay, J. R. Pardo, J. Zmuidzinas, T. G. Phillips, B. Bumble, J. Stern, and H. G. LeDuc. A Low Noise NbTiN-Based 850 GHz SIS Receiver for the Caltech Submillimeter Observatory. *International Journal of Infrared and Millimeter Waves*, 21:16–+, 2000.
- [65] E. Krugel, R. Chini, U. Klein, R. Lemke, R. Wielebinski, and R. Zylka. 1300-micron continuum observations of M82 and NGC 253. *A&A*, 240:232–236, December 1990.
- [66] M. L. Kutner and B. L. Ulich. Recommendations for calibration of millimeter-wavelength spectral line data. *ApJ*, 250:341–348, November 1981.
- [67] E. Le Floch, C. Papovich, H. Dole, E. F. Bell, G. Lagache, G. H. Rieke, E. Egami, P. G. Pérez-González, A. Alonso-Herrero, M. J. Rieke, M. Blaylock, C. W. Engelbracht, K. D. Gordon, D. C. Hines, K. A. Misselt, J. E.

- Morrison, and J. Mould. Infrared Luminosity Functions from the Chandra Deep Field-South: The Spitzer View on the History of Dusty Star Formation at $0 \lesssim z \lesssim 1$. *ApJ*, 632:169–190, October 2005.
- [68] M. Leong, R. Peng, M. Houde, H. Yoshida, R. Chamberlin, and T. G. Phillips. A CSO submillimeter active optics system. In *Society of Photo-Optical Instrumentation Engineers (SPIE) Conference Series*, volume 6275 of *Presented at the Society of Photo-Optical Instrumentation Engineers (SPIE) Conference*, July 2006.
- [69] S. J. Lilly, S. A. Eales, W. K. P. Gear, F. Hammer, O. Le Fèvre, D. Cramp-ton, J. R. Bond, and L. Dunne. The Canada-United Kingdom Deep Sub-millimeter Survey. II. First Identifications, Redshifts, and Implications for Galaxy Evolution. *ApJ*, 518:641–655, June 1999.
- [70] S. D. Lord, D. J. Hollenbach, S. W. J. Colgan, M. R. Haas, R. H. Rubin, S. C. Madden, T. Y. Steiman-Cameron, P. Carral, P. R. Maloney, and E. F. Erickson. A far-infrared spectral line survey of 23 infrared-bright Galaxy nuclei. In M. R. Haas, J. A. Davidson, and E. F. Erickson, editors, *From Gas to Stars to Dust*, volume 73 of *Astronomical Society of the Pacific Conference Series*, pages 151–158, 1995.
- [71] S. D. Lord, D. J. Hollenbach, M. R. Haas, R. H. Rubin, S. W. J. Colgan, and E. F. Erickson. Interstellar Properties of a Dual Nuclear Starburst: Far-Infrared Spectroscopy of M82. *ApJ*, 465:703–+, July 1996.
- [72] M. L. Luhman, S. Satyapal, J. Fischer, M. G. Wolfire, P. Cox, S. D. Lord, H. A. Smith, G. J. Stacey, and S. J. Unger. Infrared Space Observatory Measurements of a [C II] 158 Micron Line Deficit in Ultraluminous Infrared Galaxies. *ApJ*, 504:L11+, September 1998.
- [73] M. L. Luhman, S. Satyapal, J. Fischer, M. G. Wolfire, E. Sturm, C. C. Dudley, D. Lutz, and R. Genzel. The [C II] 158 Micron Line Deficit in Ultraluminous Infrared Galaxies Revisited. *ApJ*, 594:758–775, September 2003.
- [74] M.-M. Mac Low. The Energy Dissipation Rate of Supersonic, Magnetohydrodynamic Turbulence in Molecular Clouds. *ApJ*, 524:169–178, October 1999.
- [75] R. Maiolino, P. Cox, P. Caselli, A. Beelen, F. Bertoldi, C. L. Carilli, M. J. Kaufman, K. M. Menten, T. Nagao, A. Omont, A. Weiß, C. M. Walmsley, and F. Walter. First detection of [CII]158 μm at high redshift: vigorous star formation in the early universe. *A&A*, 440:L51–L54, September 2005.

- [76] S. Malhotra, G. Helou, G. Stacey, D. Hollenbach, S. Lord, C. A. Beichman, H. Dinerstein, D. A. Hunter, K. Y. Lo, N. Y. Lu, R. H. Rubin, N. Silbermann, H. A. Thronson, Jr., and M. W. Werner. Infrared Space Observatory Measurements of [C II Line Variations in Galaxies. *ApJ*, 491:L27+, December 1997.
- [77] S. Malhotra, M. J. Kaufman, D. Hollenbach, G. Helou, R. H. Rubin, J. Brauher, D. Dale, N. Y. Lu, S. Lord, G. Stacey, A. Contursi, D. A. Hunter, and H. Dinerstein. Far-Infrared Spectroscopy of Normal Galaxies: Physical Conditions in the Interstellar Medium. *ApJ*, 561:766–786, November 2001.
- [78] G. Marsden, C. Borys, S. C. Chapman, M. Halpern, and D. Scott. An upper limit to [CII] emission in a $z \sim 5$ galaxy. *MNRAS*, 359:43–46, May 2005.
- [79] S. Martín, R. Mauersberger, J. Martín-Pintado, C. Henkel, and S. García-Burillo. A 2 Millimeter Spectral Line Survey of the Starburst Galaxy NGC 253. *ApJS*, 164:450–476, June 2006.
- [80] J. C. Mather. Bolometer noise: nonequilibrium theory. *Appl. Opt.*, 21:1125–1129, 1982.
- [81] R. Mauersberger, C. Henkel, R. Wielebinski, T. Wiklind, and H.-P. Reuter. Molecular distribution and kinematics in nearby galaxies. I. NGC 253. *A&A*, 305:421–+, January 1996.
- [82] R. Meijerink and M. Spaans. Diagnostics of irradiated gas in galaxy nuclei. I. A far-ultraviolet and X-ray dominated region code. *A&A*, 436:397–409, June 2005.
- [83] R. Meijerink, M. Spaans, and F. P. Israel. Diagnostics of irradiated dense gas in galaxy nuclei. II. A grid of XDR and PDR models. *A&A*, 461:793–811, January 2007.
- [84] S. H. Moseley, Jr., C. D. Dowell, C. Allen, and T. G. Phillips. Semiconducting Pop-Up Bolometers for Far-Infrared and Submillimeter Astronomy. In J. G. Mangum and S. J. E. Radford, editors, *Imaging at Radio through Submillimeter Wavelengths*, volume 217 of *Astronomical Society of the Pacific Conference Series*, pages 140–+, 2000.
- [85] G. S. Orton, E. Serabyn, and Y. T. Lee. Vertical Distribution of PH₃ in Saturn from Observations of Its 1-0 and 3-2 Rotational Lines. *Icarus*, 146:48–59, July 2000.

- [86] D. E. Osterbrock and G. J. Ferland. *Astrophysics of gaseous nebulae and active galactic nuclei*. 2006.
- [87] T. A. D. Paglione, T. Tosaki, and J. M. Jackson. The Distribution of the Dense Clouds in the Starburst Nucleus of NGC 253. *ApJ*, 454:L117+, December 1995.
- [88] T. A. D. Paglione, O. Yam, T. Tosaki, and J. M. Jackson. The Structure, Kinematics, and Physical Properties of the Molecular Gas in the Starburst Nucleus of NGC 253. *ApJ*, 611:835–845, August 2004.
- [89] P. P. Papadopoulos, K. G. Isaak, and P. P. van der Werf. First CO J = 6-5 and J = 4-3 Detections in Local ULIRGs: The Dense Gas in Markarian 231 and Its Cooling Budget. *ApJ*, 668:815–825, October 2007.
- [90] J. R. Pardo, J. Cernicharo, and E. Serabyn. Atmospheric transmission at microwaves (ATM): an improved model for millimeter/submillimeter applications. *IEEE Transactions on Antennas and Propagation*, 49:1683–1694, December 2001.
- [91] W. D. Pence. A photometric and kinematic study of the barred spiral galaxy NGC 253. II - The velocity field. *ApJ*, 247:473–483, July 1981.
- [92] R. Peng, S. Zhou, J. B. Whiteoak, K. Y. Lo, and E. C. Sutton. BIMA CS J=21 Observations of NGC 253: Kinematic Evidence for Dense Gas in a Bar. *ApJ*, 470:821–+, October 1996.
- [93] T. G. Phillips and P. J. Huggins. Abundance of atomic carbon /C I/ in dense interstellar clouds. *ApJ*, 251:533–540, December 1981.
- [94] G. H. Rieke, M. J. Lebofsky, R. I. Thompson, F. J. Low, and A. T. Tokunaga. The nature of the nuclear sources in M82 and NGC 253. *ApJ*, 238:24–40, May 1980.
- [95] G. H. Rieke and K. Visnovsky. *Detection of Light, From the Ultraviolet to the Submillimeter*. Detection of Light, From the Ultraviolet to the Submillimeter, ISBN 0521576741, Illustrated by Karen Swarthout, Cambridge University Press, 1996., 1996.
- [96] D. Rigopoulou, D. Kunze, D. Lutz, R. Genzel, and A. F. M. Moorwood. An ISO-SWS survey of molecular hydrogen in starburst and Seyfert galaxies. *A&A*, 389:374–386, July 2002.

- [97] M. Röllig, N. P. Abel, T. Bell, F. Bensch, J. Black, G. J. Ferland, B. Jonkheid, I. Kamp, M. J. Kaufman, J. Le Bourlot, F. Le Petit, R. Meijerink, O. Morata, V. Ossenkopf, E. Roueff, G. Shaw, M. Spaans, A. Sternberg, J. Stutzki, W.-F. Thi, E. F. van Dishoeck, P. A. M. van Hoof, S. Viti, and M. G. Wolfire. A photon dominated region code comparison study. *A&A*, 467:187–206, May 2007.
- [98] G. B. Rybicki and A. P. Lightman. *Radiative Processes in Astrophysics*. Radiative Processes in Astrophysics, by George B. Rybicki, Alan P. Lightman, pp. 400. ISBN 0-471-82759-2. Wiley-VCH, June 1986., June 1986.
- [99] D. B. Sanders and I. F. Mirabel. Luminous Infrared Galaxies. *ARA&A*, 34:749–+, 1996.
- [100] B. D. Savage and K. R. Sembach. Interstellar Abundances from Absorption-Line Observations with the Hubble Space Telescope. *ARA&A*, 34:279–330, 1996.
- [101] P. Schilke, J. E. Carlstrom, J. Keene, and T. G. Phillips. Atomic Carbon in M82. *ApJ*, 417:L67+, November 1993.
- [102] J. Schmid-Burgk, R. Densing, E. Krugel, H. Nett, H. P. Roser, F. Schafer, G. Schwaab, P. van der Wal, and R. Wattenbach. Extended CO (J = 7-6) emission from Orion molecular cloud 1 - Hot ambient gas, two hot-outflow sources. *A&A*, 215:150–164, May 1989.
- [103] S. E. Scott, M. J. Fox, J. S. Dunlop, S. Serjeant, J. A. Peacock, R. J. Ivison, S. Oliver, R. G. Mann, A. Lawrence, A. Efstathiou, M. Rowan-Robinson, D. H. Hughes, E. N. Archibald, A. Blain, and M. Longair. The SCUBA 8-mJy survey - I. Submillimetre maps, sources and number counts. *MNRAS*, 331:817–838, April 2002.
- [104] N. Z. Scoville, B. T. Soifer, G. Neugebauer, K. Matthews, J. S. Young, and J. Yerka. The inner disk of NGC 253. *ApJ*, 289:129–140, February 1985.
- [105] I. Smail, R. J. Ivison, A. W. Blain, and J.-P. Kneib. The nature of faint submillimetre-selected galaxies. *MNRAS*, 331:495–520, March 2002.
- [106] B. T. Soifer and G. Neugebauer. The properties of infrared galaxies in the local universe. *AJ*, 101:354–361, February 1991.
- [107] B. T. Soifer, D. B. Sanders, B. F. Madore, G. Neugebauer, G. E. Danielson,

- J. H. Elias, C. J. Lonsdale, and W. L. Rice. The IRAS bright galaxy sample. II - The sample and luminosity function. *ApJ*, 320:238–257, September 1987.
- [108] P. M. Solomon and P. A. Vanden Bout. Molecular Gas at High Redshift. *ARA&A*, 43:677–725, September 2005.
- [109] G. J. Stacey, N. Geis, R. Genzel, J. B. Lugten, A. Poglitsch, A. Sternberg, and C. H. Townes. The 158 micron forbidden C II line - A measure of global star formation activity in galaxies. *ApJ*, 373:423–444, June 1991.
- [110] G. J. Stacey, D. T. Jaffe, N. Geis, R. Grenzel, A. I. Harris, A. Poglitsch, J. Stutzki, and C. H. Townes. 158 micron forbidden C II mapping of the Orion molecular cloud. *ApJ*, 404:219–231, February 1993.
- [111] S. W. Stahler and F. Palla. *The Formation of Stars*. January 2005.
- [112] J. Stutzki, U. U. Graf, S. Haas, C. E. Honingh, D. Hottgenroth, K. Jacobs, R. Schieder, R. Simon, J. Staguhn, G. Winnewisser, R. N. Martin, W. L. Peters, and J. P. McMullin. Atomic Carbon in M82: Physical Conditions Derived from Simultaneous Observations of the [C i] Fine-structure Submillimeter-wave Transitions. *ApJ*, 477:L33+, March 1997.
- [113] J. Stutzki, G. J. Stacey, R. Genzel, A. I. Harris, D. T. Jaffe, and J. B. Lugten. Submillimeter and far-infrared line observations of M17 SW - A clumpy molecular cloud penetrated by ultraviolet radiation. *ApJ*, 332:379–399, September 1988.
- [114] R. V. Sudiwala, M. J. Griffin, and A. L. Woodcraft. Thermal Modelling and Characterisation of Semiconductor Bolometers. *IJIMW*, 23:545–573, April 2002.
- [115] A. M. Swinbank, S. C. Chapman, I. Smail, C. Lindner, C. Borys, A. W. Blain, R. J. Ivison, and G. F. Lewis. The link between submillimetre galaxies and luminous ellipticals: near-infrared IFU spectroscopy of submillimetre galaxies. *MNRAS*, 371:465–476, September 2006.
- [116] L. J. Tacconi, R. Neri, S. C. Chapman, R. Genzel, I. Smail, R. J. Ivison, F. Bertoldi, A. Blain, P. Cox, T. Greve, and A. Omont. High-Resolution Millimeter Imaging of Submillimeter Galaxies. *ApJ*, 640:228–240, March 2006.

- [117] C. M. Telesco, L. L. Dressel, and R. D. Wolstencroft. The genesis of starbursts and infrared emission in the centers of galaxies. *ApJ*, 414:120–143, September 1993.
- [118] C. M. Telesco and D. A. Harper. Galaxies and far-infrared emission. *ApJ*, 235:392–404, January 1980.
- [119] A. G. G. M. Tielens and D. Hollenbach. Photodissociation Regions - Part Two - a Model for the Orion Photodissociation Region. *ApJ*, 291:747–+, April 1985.
- [120] A. G. G. M. Tielens and D. Hollenbach. Photodissociation regions. I - Basic model. II - A model for the Orion photodissociation region. *ApJ*, 291:722–754, April 1985.
- [121] J. S. Ulvestad and R. R. J. Antonucci. VLA Observations of NGC 253: Supernova Remnants and H II Regions at 1 Parsec Resolution. *ApJ*, 488:621–+, October 1997.
- [122] G. Ventura, M. Barucci, E. Gottardi, and I. Peroni. Low temperature thermal conductivity of Kevlar. *Cryogenics*, 40:489–491, January 2000.
- [123] G. M. Voellmer, C. A. Allen, S. R. Babu, A. E. Bartels, C. D. Dowell, J. L. Dotson, D. A. Harper, S. H. Moseley, Jr., T. Rennick, P. J. Shirron, W. W. Smith, and E. J. Wollack. A two-dimensional semiconducting bolometer array for HAWC. In C. M. Bradford, P. A. R. Ade, J. E. Aguirre, J. J. Bock, M. Dragovan, L. Duband, L. Earle, J. Glenn, H. Matsuhara, B. J. Naylor, H. T. Nguyen, M. Yun, and J. Zmuidzinas, editors, *Society of Photo-Optical Instrumentation Engineers (SPIE) Conference Series*, volume 5498 of *Presented at the Society of Photo-Optical Instrumentation Engineers (SPIE) Conference*, pages 428–437, October 2004.
- [124] J. S. Ward, J. Zmuidzinas, A. I. Harris, and K. G. Isaak. A ^{12}CO J=6-5 Map of M82: The Significance of Warm Molecular Gas. *ApJ*, 587:171–185, April 2003.
- [125] G. J. White, B. Ellison, S. Claude, W. R. F. Dent, and D. N. Matheson. CO and CI maps of the starburst galaxy M 82. *A&A*, 284:L23–L26, April 1994.
- [126] M. G. Wolfire, A. G. G. M. Tielens, and D. Hollenbach. Physical conditions in photodissociation regions - Application to galactic nuclei. *ApJ*, 358:116–131, July 1990.

- [127] A. L. Woodcraft, R. V. Sudiwala, M. J. Griffin, E. Wakui, B. Maffei, C. E. Tucker, C. V. Haynes, F. Gannaway, P. A. R. Ade, J. J. Bock, A. D. Turner, S. Sethuraman, and J. W. Beeman. High Precision Characterisation of Semiconductor Bolometers. *IJIMW*, 23:575–595, April 2002.
- [128] J. Zmuidzinas, A. L. Betz, R. T. Boreiko, and D. M. Goldhaber. Neutral atomic carbon in dense molecular clouds. *ApJ*, 335:774–785, December 1988.